Controlled Metal Nitrate Decomposition for the Preparation of Supported Metal Catalysts

Gecontroleerde ontleding van metaalnitraten voor de bereiding van metaalkatalysatoren

(met een samenvatting in het Nederlands)

Proefschrift

ter verkrijging van de graad van doctor aan de Universiteit Utrecht op gezag van de rector magnificus, prof. dr. J.C. Stoof, ingevolge het besluit van het college voor promoties in het openbaar te verdedigen op maandag 22 november 2010 des ochtends te 10.30 uur

door

Mariska Wolters

geboren op 30 augustus 1983 te Lelystad

Promotor: Prof. dr. ir. K.P. de Jong

Co-promotor: Dr. P. E. de Jongh

The research described in this thesis was financially supported by Johnson Matthey Catalysts.

Voor mijn familie

ISBN: 978-90-6464-425-2

Printed by GVO drukkers & vormgevers B.V. | Ponsen & Looien

Contents

Chapter 1

General Introduction

Catalysts

Since their discovery in 1835, catalysts have taken an ever increasing role in the production of fuels, chemicals, pharmaceuticals, and the abatement of environmental pollution. It has been estimated that presently around 85% of all chemical processes involve catalysts to increase efficiency and selectivity. Three types of catalysts can be distinguished: heterogeneous, homogeneous and bio-catalysts. Heterogeneous catalysts are most widely applied industrially, making up for around 80% of the total number of catalytic processes.[1] With the ever growing demand of chemicals, tightening environmental legislation and diminishing fossil fuel resources, both catalyst sales and development are expected to steadily increase.

The major class of heterogeneous catalysts are supported metals, metal oxides and metal sulphides which find application in important reactions, including (de)hydrogenation, epoxidation, polymerization, NO_x reduction and hydrodesulphurization.[1-2] Although each reaction requires a catalyst with specific chemical and physical properties, typically three classes of components are present: the active metal, metal oxide or metal sulphide, the support, and (structural or chemical) promoters. As the catalytic reaction occurs at the surface of the metal (oxide), a high surface area to volume ratio is usually desired, which explains the need of the second component, the support. The primary role of the support is to facilitate dispersion of the metal (oxide) particles and to increase the accessibility and stability during reaction. Although the physical property requirements of the support vary with each application, a good support generally exhibits a high surface area, large pore volume, low chemical reactivity and a high thermal and mechanical stability. Frequently applied supports are based on SiO_2, Al_2O_3 and TiO_2. Structural or chemical promoters are added to increase the catalyst's activity, stability and/or selectivity. Examples are manganese in cobalt based FT catalysts, and silica and potassium in iron based FT catalysts.

Ordered mesoporous silica supports

The preparation method largely determines the catalytic activity, selectivity and stability and, therefore, a great number of studies have been devoted to optimizing and understanding the catalyst preparation conditions.[3-17] Ordered mesoporous silica (OMS) supports have become a valuable tool in fundamental preparation studies. Following the invention MCM-41 by Mobil researchers there has been a wide spread interest in these type of materials resulting in the development of a range of different structures and pore sizes.[18-22] Figure 1 shows schematic representations of an OMS and a conventional silica. In a conventional silica, pores correspond to the

interparticle voids. Consequently, these materials exhibit broad pore size distributions and irregular pore shapes. OMS supports such as SBA-15 and MCM-41, on the other hand, have hexagonally ordered mesopores with a narrow pore size distribution. Because of the well defined pore structure more detailed information can be obtained on the distribution of the active phases after individual preparation steps, using for example electron microscopy and N_2-physisorption.[23-24] Another advantage is that the average pore size can be varied over a wide range (2-15 nm) facilitating studies focusing on the impact of phase confinement by the pore walls on for example the particle size or catalytic activity, [25-29] as will be discussed in Chapter 5.

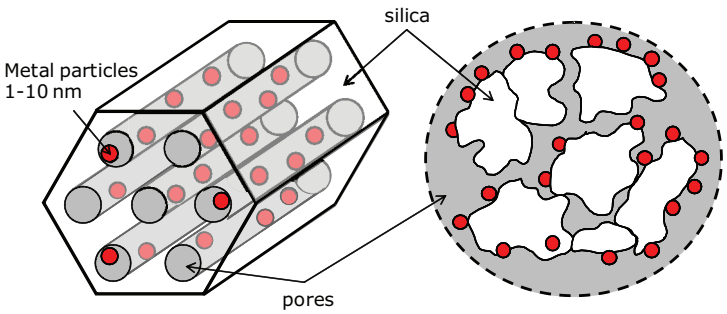

Figure 1: Schematic representations of an ordered mesoporous silica (left) and a conventional porous silica (right). Gray regions indicate pores or voids and the white regions the silica. The gray spheres indicate deposited metal particles.

The flexibility in the pore size and geometry of OMS supports is a direct result of their preparation method, which makes use of organic templates. Figure 2 shows a schematic overview of the preparation route. MCM-type materials are generally prepared using quaternary ammonium salts ($C_nH_{2n+1}(C_mH_{2m+1})_3NX$ with n = 6–22, m = 1–4 and X = OH/Cl, OH, Cl, Br or HSO_4) in basic medium, and SBA-type materials with non-ionic triblock copolymers ($(EO)_n(PO)_m(EO)_n$, EO = ethylene oxide, PO = propylene oxide) in acidic medium.[21] The first step in the synthesis is the dissolution of the template in its proper medium, which results in the formation of liquid crystals (Figure 2). These crystals may act as a template for the silica precursor (for example TEOS) that is subsequently added. Stirring of the mixture at slightly elevated temperatures (30-40°C) will result in assembly of the silica precursor around the liquid crystals via a combination of electrostatic, hydrogen bonding and van der Waals interactions.[21] During this stage some condensation occurs, which is completed by aging the mixture at higher temperatures, generally between 60 and 150 °C, resulting in a mesostructured hybrid network (Figure 2). After filtration and

washing, the template is removed via calcination or extraction to yield mesoporous silica. The temperature at which the aging step is performed and the type of surfactant influences the final mesopore size and pore ordering, where higher temperatures and longer-chain surfactants lead to larger pores.[30] As a result of the incorporation of the EO moieties in the silica during growth, SBA-type materials generally exhibit intrapore wall porosity, created by 0.5-3 nm connecting pores.[19,30-33] The presence of interconnecting pores also opens the possibility to use these materials as hard templates for the preparation of nanostructures metal oxides and carbons.[34-38] In addition, the thicker pore walls result in a higher hydrothermal stability as compared to MCM-41.[30,39-40]

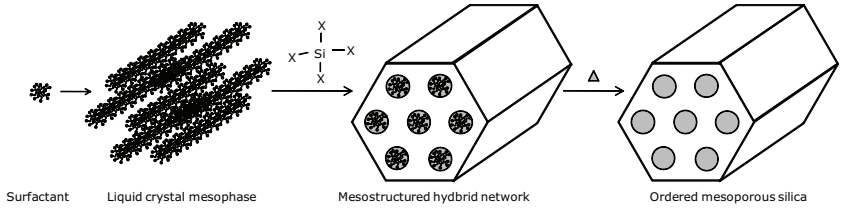

Figure 2: Schematic overview of the general preparation route for ordered mesoporous silica supports.

Preparation of supported catalysts by impregnation

Deposition of metal precursors onto a support (e.g. SiO_2 or Al_2O_3) can be conducted from the vapour phase or liquid phase.[41-43] Techniques involve vapour deposition, deposition-precipitation, ion-exchange, co-precipitation and impregnation. Commonly, the latter technique is preferred, because of its practical simplicity and small waste streams. A schematic overview of the impregnation preparation route is given in Figure 3.

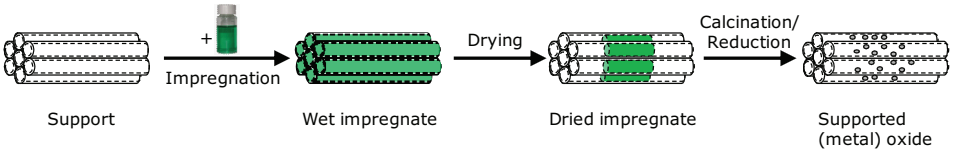

Figure 3: Schematic overview of catalyst preparation via impregnation.

The use of organic precursors for the impregnation generally yields high dispersions; however, due to the limited solubility multiple impregnation steps are often required to achieve the desired metal loading.[44] Inorganic precursors such as nitrates, sulphates and chlorides generally have much higher solubility in water,

which makes them attractive to industry as higher loadings can be obtained in a single impregnation step. Nitrate precursors, in contrast to sulphate and chloride precursors, are easily converted into pure oxides via so-called 'calcination' in air and are, therefore, preferred. Nevertheless, nitrate precursors may give rise to poorly dispersed metal-oxide phases due to agglomeration during drying and thermal treatment.[44-45]

Several different approaches to counter the agglomeration have been reported, including the use of chelating and viscosity-increasing agents in the impregnation solution and the tuning of the drying conditions such as heating rate and temperature.[10,45-50] Other successful approaches are the direct reduction[11,51-52] and glow discharge plasma assisted decomposition of metal nitrates.[17] Recently, a very effective and facile method for the prevention of agglomeration was reported, i.e., the replacement of the traditional air calcination by a thermal treatment in 1% v/v NO/He, resulting for instance in high NiO and Co_3O_4 dispersions.[53-54] The origin of the improved dispersion obtained with this method will be discussed in Chapters 3 and 4.

Metal nitrate decomposition

Because of their extensive use as catalyst precursors, the agglomeration behaviour of metal nitrates has been studied for many years and it is generally accepted that the final phase and particle size critically depend on the experimental conditions, as reported for both supported and unsupported metal nitrates. [55-57] In general the decomposition of a metal nitrate goes through three stages (Equations 1-3). The first step is partial dehydration at low temperatures (Equation 1). During heating some metal nitrates may dissolve in their own crystal water, often referred to as melting. The degree of dehydration is generally dependent on both the metal nitrate and the experimental conditions. The second stage comprises the hydrolysis of the complex to form nitric acid and a metal hydroxynitrate (Equation 2). This process is determined by the acidity of the metal nitrate hydrate complex. In addition, sufficient water has to be present.[10,12,49] Therefore, heating in vacuum[57-58] or a fast gas flow (vide infra) may suppress its formation, leading to the direct decomposition to the oxide (Equation 3a) rather than via the metal hydroxynitrate (Equation 3b).

$$M(NO_3)_m \cdot nH_2O \xrightarrow{30\text{-}60\ ^\circ C} M(NO_3)_m \cdot (n\text{-}q)H_2O + qH_2O \quad (1)$$

$$M(NO_3)_m \cdot (n\text{-}q)H_2O \xrightarrow{60\text{-}180\ ^\circ C} M(OH)_r(NO_3)_{m\text{-}r} + rHNO_3 + (n\text{-}q\text{-}r)H_2O \quad (2)$$

$$M(NO_3)_m \cdot (n\text{-}q)H_2O \xrightarrow{\geq 120\ ^\circ C} MO_{m/2} + (NO_2, NO, N_2O, O_2, H_2O) \quad (3a)$$

$$M(OH)_r(NO_3)_{m\text{-}r} \xrightarrow{\geq 120\ ^\circ C} MO_{r/2} + (NO_2, NO, N_2O, O_2, H_2O) \quad (3b)$$

The impact of the decomposition pathway on the final dispersion is debated in literature. For NiO obtained via intermediate nickel hydroxynitrate species a lower specific surface area (1 $m^2\ g^{-1}$) compared to NiO obtained via anhydrous nickel nitrate species (10 $m^2\ g^{-1}$) was found.[57-58] A similar relation between the nature of the intermediates and the dispersion was reported by Louis et al.[12,49] The authors found that drying of silica supported copper and zinc nitrate at elevated temperatures resulted in the growth of large copper and zinc hydroxynitrate crystals, and it was proposed that their formation was responsible for the broad particle size distribution that was found. Best results were obtained by drying at room temperature followed by a direct reduction treatment. On the other hand, for titania supported cobalt nitrate the opposite was reported.[59] In a patent application by Soled et al. a high temperature drying treatment was found to increase the cobalt dispersion. Aging of the dried sample in a wet environment prior to the calcination further improved the dispersion. It was hinted that the formation of cobalt nitrosyls during the high temperature drying step were the key to the improved dispersions. With regard to the function of the hydrolyzing step no further details were given, but it likely led to the formation of hydroxynitrates which is in contrast with the study on copper. In conclusion, although copper, nickel and cobalt are very similar metals, the decomposition and agglomeration behaviour of their nitrates can be very different, requiring separate studies.

Scope and outline of this thesis

The aim of the research described in this thesis was to gain fundamental insight in the relation between the decomposition pathway of supported metal nitrate catalysts precursors and the metal oxide dispersion in the final catalyst. To this end a wide range of silica supported metal nitrate precursors was studied, including; scandium, iron, manganese, cobalt, nickel, copper and zinc nitrate. Characterization techniques such as XRD, diffuse reflectance FTIR spectroscopy, thermal gravimetric analysis (TGA) and mass spectrometry (MS), were employed to study the phase and gas evolution *in situ*.

In **Chapter 2** the decomposition of a wide range of silica supported metal

nitrate catalyst precursors is studied using TGA and MS. It is demonstrated that the presence of nitric oxide during the decomposition significantly lowers the decomposition temperature of all investigated metal nitrates. In addition it is shown that for cobalt, nickel and copper nitrate the presence of nitric oxide induces nearly complete hydrolysis to the corresponding hydroxynitrates at low temperature, whereas in argon this occurs to a much smaller extent and at higher temperatures. **Chapter 3** demonstrates that this increased formation of cobalt and nickel hydroxynitrates is a key to prevent long range redistribution and agglomeration. *In situ* DRIFTS and XRD are combined with selective removal of the soluble species to relate the nature and fraction of the different phases present to the treatment drying conditions and final dispersion after calcination. Although the dispersion is significantly improved by applying drying treatment in NO, **Chapter 4** demonstrates that NO also plays a significant role in preventing agglomeration at higher temperatures. Here the influence of the gas atmosphere on the decomposition of supported nickel nitrate, dried at 120 °C in stagnant air, is shown using *in situ* DRIFTS, MS and isotopically labelled gasses. Above 200 °C NO acts as an oxygen scavenger, moderating the decomposition and creating NiO nuclei at lower temperatures compared to other gasses. Furthermore, this principle is extended to other oxygen scavenging gasses such as N_2O and H_2. **Chapter 5** deals with controlling the average particle size. It is demonstrated that by combining NO calcination with the use of ordered mesoporous materials with different pore diameters the average crystallite size can be varied while maintaining a narrow particle size distribution. **Chapter 6** discusses the decomposition of copper nitrate, which behaves quite differently from cobalt and nickel. During decomposition of silica supported copper nitrate hydrate in a flow of N_2 or air, a volatile anhydrous copper nitrate is formed which causes redispersion prior to the decomposition to copper oxide. The presence of nitric oxide induces hydrolysis of the copper nitrate hydrate to highly dispersed copper hydroxynitrate. Although an NO/N_2 flow effectively prevents the formation of anhydrous copper nitrate a similar surface area is obtained compared to calcination in an N_2 flow. Finally, a summary and the concluding remarks are presented in **Chapter 7**.

References

1. *Synthesis of Solid Catalysts*; de Jong, K. P., Ed.; Wiley-VCH Verlag GmbH & Co.: Weinheim, 2009.
2. *Catalyst Preparation: Science and Engineering*; Regalbuto, J. R., Ed.; Taylor & Francis, CRC Press: Boca Raton, 2007.
3. Miller, J. T.; Schreier, M.; Kropf, A. J.; Regalbuto, J. R. *J. Catal.* **2004**, *225*, 203.
4. Schreier, M.; Regalbuto, J. R. *J. Catal.* **2004**, *225*, 190.
5. Negrier, F.; Marceau, E.; Che, M.; Giraudon, J. *J. Phys. Chem. B* **2005**, *109*, 2836.
6. Sun, K. Q.; Marceau, E.; Che, M. *Phys. Chem. Chem. Phys.* **2006**, *8*, 1731.
7. Dumond, F.; Marceau, E.; Che, M. *J. Phys. Chem. C* **2007**, *111*, 4780.
8. Marceau, E.; Che, M.; Čejka, J.; Zukal, A. *ChemCatChem* **2010**, *2*, 413.
9. Burattin, P.; Che, M.; Louis, C. *J. Phys. Chem. B* **1999**, *103*, 6171.
10. Chouillet, C.; Villain, F.; Kermarec, M.; Lauron-Pernot, H.; Louis, C. *J. Phys. Chem. B* **2003**, *107*, 3565.
11. Louis, C.; Xing Cheng, Z.; Che, M. *J. Phys. Chem.* **1993**, *97*, 5703.
12. Toupance, T.; Kermarec, M.; Louis, C. *J. Phys. Chem. B* **2000**, *104*, 965.
13. Borg, Ø.; Blekkan, E. A.; Eri, S.; Akporiaye, D.; Vigerust, B.; Rytter, E.; Holmen, A. *Top. Catal.* **2007**, *45*, 39.
14. Borg, Ø.; Eri, S.; Blekkan, E. A.; Storsæter, S.; Wigum, H.; Rytter, E.; Holmen, A. *J. Catal.* **2007**, *248*, 89.
15. Borg, Ø.; Dietzel, P. D. C.; Spjelkavik, A. I.; Tveten, E. Z.; Walmsley, J. C.; Diplas, S.; Eri, S.; Holmen, A.; Rytter, E. *J. Catal.* **2008**, *259*, 161.
16. van der Meer, J.; Bardez, I.; Bart, F.; Albouy, P. A.; Wallez, G.; Davidson, A. *Micropor. Mesopor. Mat.* **2009**, *118*, 183.
17. Chu, W.; Wang, L.; Chernavskii, P.; Khodakov, A. Y. *Angew. Chem. Int. Ed.* **2008**, *47*, 5052.
18. Kresge, C. T.; Leonowicz, M. E.; Roth, W. J.; C., V. J.; Beck, J. S. *Nature* **1992**, *359*, 710.
19. Zhao, D.; Feng, J.; Huo, Q.; Melosh, N.; Fredrickson, G. H.; Chmelka, B. F.; Stucky, G. D. *Science* **1998**, *279*, 548.
20. Beck, J. S.; Vartuli, J. C.; Roth, W. J.; Leonowicz, M. E.; Kresge, C. T.; Schmitt, K. D.; Chu, C. T.-W.; Olson, D. H.; Sheppard, E. W.; McCullen, S. B.; Higgins, J. B.; Schlenker, J. L. *J. Am. Chem. Soc* **1992**, *114*, 10834.
21. Meynen, V.; Cool, P.; Vansant, E. F. *Micropor. Mesopor. Mat.* **2009**, *125*, 170.
22. Kleitz, F.; Choi, S. H.; Ryoo, R. *Chem. Commun.* **2003**, 2136.
23. Sietsma, J. R. A.; Meeldijk, J. D.; Versluijs-Helder, M.; Broersma, A.; van Dillen,

A. J.; de Jongh, P. E.; de Jong, K. P. *Chem. Mater.* **2008**, *20*, 2921.
24. Friedrich, H.; Sietsma, J. R. A.; de Jongh, P. E.; Verkley, A. J.; de Jong, K. P. *J. Am. Chem. Soc.* **2007**, *129*, 10249.
25. Khodakov, A. Y.; Griboval-Constant, A.; Bechara, R.; Villain, F. *J. Phys. Chem. B* **2001**, *105*, 9805.
26. Jentys, A.; Pham, N. H.; Vinek, H.; Englisch, M.; Lercher, J. A. *Catal. Today* **1998**, *39*, 311.
27. Li, H. L.; Li, J. L.; Ni, H. K.; Song, D. C. *Catal. Lett.* **2006**, *110*, 71.
28. Borg, O.; Walmsley, J. C.; Dehghan, R.; Tanem, B. S.; Blekkan, E. A.; Eri, S.; Rytter, E.; Holmen, A. *Catal. Lett.* **2008**, *126*, 224.
29. Wolters, M.; van Grotel, L. J. W.; Eggenhuisen, T. M.; Sietsma, J. R. A.; de Jong, K. P.; de Jongh, P. E. *Catal. Today* **2010**, 10.1016/j.cattod.2010.02.052.
30. Zhao, D.; Feng, J.; Huo, Q.; Feng, J.; Bradley, F.; Chmelka, B. F.; Stucky, G. D. *J. Am. Chem. Soc.* **1998**, *120*, 6024.
31. Imperor-Clerc, M.; Davidson, P.; Davidson, A. *J. Am. Chem. Soc* **2000**, *122*, 11925.
32. Galarneau, A.; Cambon, H.; Di Renzo, F.; Ryoo, R.; Choi, M.; Fajula, F. *New J. Chem.* **2003**, *27*, 73.
33. Soler-Illia, G. J. A. A.; Crepaldi, E. L.; Grosso, D.; Sanchez, C. *Curr. Opin. Colloid Interface Sci.* **2003**, *8*, 109.
34. Rumplecker, A.; Kleitz, F.; Salabas, E.; Schuth, F. *Chem. Mater.* **2007**, *19*, 485.
35. Joo, S. H.; Ryoo, R.; Kruk, M.; Jaroniec, M. *J. Phys. Chem. B* **2002**, *106*, 4640.
36. Ryoo, R.; Ko, C. H.; Kruk, M.; Antoschuk, V.; Jaroniec, M. J. *J. Phys. Chem. B* **2000**, *104*, 11465.
37. Tian, B.; Liu, X.; Solovyov, L. A.; Liu, Z.; Yang, H.; Zhang, Z.; Xie, S.; Zhang, F.; Tu, B.; Yu, C.; Terasaki, O.; Zhao, D. *J. Am. Chem. Soc.* **2004**, *126*, 865.
38. Tian, B.; Liu, X.; Yang, H.; Xie, S.; Yu, C.; Tu, B.; Zhao, D. *Adv. Mater.* **2003**, *15*, 1370.
39. Galarneau, A.; Nader, M.; Guenneau, F.; Di Renzo, F.; Gedeon, A. *J. Phys. Chem. C* **2007**, *111*, 8268.
40. Khodakov, A. Y.; Zholobenko, V. L.; Bechara, R.; Durand, D.; Sen, T. *Micropor. Mesopor. Mater.* **2005**, *79*, 29.
41. de Jong, K. P. *Curr. Opin. Solid State Mater. Sci.* **1999**, *4*, 55.
42. Bourikas, K.; Kordulis, C.; Lycourghiotis, A. *Catal. Rev. Sci. Eng.* **2006**, *48*, 363.
43. van der Lee, M. K.; Van Dillen, A. J.; Bitter, J. H.; de Jong, K. P. *J. Am. Chem. Soc.* **2005**, *127*, 13573.
44. van Dillen, A. J.; Terörde, R. J. A. M.; Lensveld, D. J.; Geus, J. W.; de Jong, K. P. *J. Catal.* **2003**, *216*, 257.

45. van de Loosdrecht, J.; Barradas, S.; Caricato, E. A.; Ngwenya, N. G.; Nkwanyana, P. S.; Rawat, M. A. S.; Sigwebela, B. H.; van Berge, P. J.; Visagie, J. L. *Top. Catal.* **2003**, *26*, 121.
46. Lensveld, D. J.; Mesu, J. G.; Van Dillen, A. J.; De Jong, K. P. *Micropor. Mesopor. Mat.* **2001**, *401*, 44.
47. Negrier, F.; Marceau, E.; Che, M. *Chem. Commun.* **2002**, 1194.
48. Infantes-Molina, A.; Mérida-Robles, J.; Braos-García, P.; Rodríguez-Castellón, E.; Finocchio, E.; Busca, G.; Maireles-Torres, P.; Jiménez-López, A. *J. Catal.* **2004**, *225*, 479.
49. Catillon-Mucherie, S.; Ammari, F.; Krafft, J. M.; Lauron-Pernot, H.; Touroude, R.; Louis, C. *J. Phys. Chem. C* **2007**, *111*, 11619.
50. Marceau, E.; Löfberg, A.; Giraudon, J.-M.; Négrier, F.; Che, M.; Leclercq, L. *Appl. Catal. A: Gen.* **2009**, *362*, 34.
51. Bartholomew, C. H.; Farrauto, R. J. *J. Catal.* **1976**, *45*, 41.
52. Sietsma, J. R. A.; Meeldijk, J. D.; den Breejen, J. P.; Versluijs-Helder, M.; van Dillen, A. J.; de Jongh, P. E.; de Jong, K. P. *Angew. Chem. Int. Ed.* **2007**, *46*, 7.
53. Sietsma, J. R. A.; Friedrich, H.; Broersma, A.; Versluijs-Helder, M.; van Dillen, A. J.; de Jongh, P. E.; de Jong, K. P. *J. Catal.* **2008**, *260*, 227.
54. Sietsma, J. R. A.; Van Dillen, A. J.; de Jongh, P. E.; De Jong, K. P., WO2007/071899, **2005**.
55. Paulik, F.; Paulik, J.; Arnold, M. *Thermochim. Acta* **1987**, *121*, 137.
56. Elmasry, M. A. A.; Gaber, A.; Khater, E. M. H. *J. Therm. Anal. Calorim.* **1998**, *52*, 489.
57. Estelle, J.; Salagre, P.; Cesteros, Y.; Serra, M.; Medina, F.; Sueiras, J. E. *Solid State Ionics* **2003**, *156*, 233.
58. Llewellyn, P. L.; Chevrota, V.; J. Ragaib; Cerclier, O.; Estienne, J.; Rouquerol, F. *Solid State lonics* **1997**, *101-103* 1293.
59. Soled, S. L.; Baumgartner, J. E.; Kliewer, C. E.; El-Malki, E.; Bielenberg, P. A.,US 2010/0022388 A1, **2010**.

Chapter 2

Thermal Decomposition of Silica-Supported First Row Transition Metal Nitrates

Abstract: The impact of NO on the decomposition of the silica supported first row transition metal nitrates of Sc, Mn, Fe, Co, Ni, Cu, Zn, was investigated using thermal gravimetric analysis and mass spectrometry. It was found that NO decreased the temperature of decomposition significantly for all investigated metal nitrates. For cobalt and nickel nitrate it was verified that decomposition in the presence of NO yielded high dispersions and narrow particle size distributions, whereas in Ar agglomeration resulted in broad particle size distributions. The beneficial effect of NO on the dispersion of cobalt and nickel oxide coincided with a large difference in the decomposition profiles of these metal nitrates compared to that in Ar. It was found that NO induced fast and complete hydrolysis to highly dispersed cobalt and nickel hydroxynitrates which decomposed to yield highly dispersed metal oxides. This is in contrast to literature reports that ascribe loss in dispersion to the formation of metal hydroxynitrate intermediates.

Adapted with permission from Mariska Wolters, Ignacio C. A. Contreras Andrade, Peter Munnik, Johannes H. Bitter, Petra E. de Jongh, Krijn P. de Jong, *Impact of NO on the decomposition of supported metal nitrate catalyst precursors and the final metal oxide dispersion*, Stud. Surf. Sci. Catal. 175 (2010) 69. Copyright 2010 Elsevier.

Introduction

Transition metal nitrate hydrates are industrially favoured precursors for the preparation of supported metal (oxide) catalysts because of their high solubility and facile nitrate removal. The final phase and particle size depend on the experimental conditions, as reported for both supported and unsupported metal nitrates.[1-3] Several authors report that decreasing the water partial pressure during the decomposition of unsupported nickel nitrate hexahydrate, via vacuum or a high gas flow, increases the final NiO surface area.[3-4] The low water partial pressure results in dehydration of the nickel nitrate hydrate to anhydrous nickel nitrate followed by decomposition to NiO. Decomposition at higher partial pressures, however, occurred through the formation of intermediate nickel hydroxynitrates prior to decomposition to NiO. Thus, NiO obtained via intermediate nickel hydroxynitrate species showed a poorer surface area (1 $m^2 g^{-1}$) compared to NiO obtained via anhydrous nickel nitrate species (10 $m^2 g^{-1}$).[3-4]

For supported zinc and copper nitrate a similar observation was reported. Louis et al. investigated the impact of the drying temperature on the copper and zinc oxide dispersion and found that drying at elevated temperatures (90-200 °C) resulted in the formation of wide particle size distributions.[5-7] The wide particle size distribution was ascribed to the formation of large copper and zinc hydroxynitrate crystals during drying, which decomposed to form large CuO and ZnO agglomerates. Highest dispersions were obtained by drying at room temperature, which prevents hydrolysis to the hydroxynitrate, followed by thermal decomposition in the presence of hydrogen. The latter was essential as decomposition in air yielded wide particle size distributions, irrespective of the drying treatment.

In the case of supported cobalt and nickel nitrate agglomeration during drying is limited, but extensive during high temperature decomposition (240-350 °C).[8-9] Again efficient decomposition gas removal positively affects the dispersion,[8] however, agglomeration cannot fully be prevented in this way. Our group recently reported a facile method to prevent agglomeration via thermal decomposition of silica supported nickel or cobalt nitrate in a 1% v/v NO/He flow, reducing the average metal oxide particle size from 10-35 nm in air to 2-7 nm in 1% v/v NO/He.[10-11]

This Chapter gives an overview of the impact of NO on the decomposition temperature and pathway of silica-supported first row d-metal nitrates and the resulting metal oxide dispersions. It was found that NO significantly lowered the decomposition temperatures of all investigated metal nitrates and changed the decomposition pathways of cobalt, nickel and copper nitrate. For nickel and cobalt nitrate it was verified that an improved dispersion was obtained after thermal

treatment in the presence of NO as compared to Ar. Copper nitrate will be discussed separately in Chapter 6 as it behaves differently from nickel and cobalt nitrate.

Experimental

Sample preparation

Silica supported samples were typically prepared by impregnation of Davicat 1404 silica gel, supplied by Grace Davidson (SA = 470 m^2 g^{-1}, PV = 0.9 ml g^{-1}, PD = 7 nm), to incipient wetness with a 3M solution of the appropriate metal nitrate. The metal nitrate solutions were made by dissolving the respective metal nitrate hydrate in a 0.1M HNO_3 solution. In view of the solubility of scandium nitrate a 2M solution was prepared. After an equilibration period of 15 minutes the impregnates were dried for 48 h in a dessicator to remove most of the solvent water, and stored in closed containers in a dessicator. This approach was preferred over drying at elevated temperatures or no drying because it leaves the nitrate intact and facilitates handling and storage, as compared to wet samples. SBA-15 (SA = 600 m^2 g^{-1}, PV = 0.7 ml g^{-1}, PD = 8 nm) samples were prepared similarly to the silica gel samples. Table 1 lists the used metal nitrates, intended metal loading and sample codes, where "SG" stands for silica gel and "SBA" for SBA-15.

Table 1. Sample codes and metal loadings

sample code	**metal nitrate**	**metal loading** (wt%)
SG-Sc / SBA-Sc	$Sc(NO_3)_3 \cdot 4H_2O$	8 / 6
SG-Mn / SBA-Mn	$Mn(NO_3)_2 \cdot 4H_2O$	14 / 10
SG-Fe / SBA-Fe	$Fe(NO_3)_3 \cdot 9H_2O$	14 / 10
SG-Co / SBA-Co	$Co(NO_3)_2 \cdot 6H_2O$	15 / 11
SG-Ni / SBA-Ni	$Ni(NO_3)_2 \cdot 6H_2O$	15 /11
SG-Cu / SBA-Cu	$Cu(NO_3)_2 \cdot 3H_2O$	16 /12
SG-Zn / SBA-Zn	$Zn(NO_3)_2 \cdot 6H_2O$	16 /12

Thermal analysis

Thermal gravimetric analysis (TGA) was performed with a Perkin-Elmer Pyris 1 apparatus. Typically 15 mg of impregnated silica gel was heated with a ramp of 5 °C min^{-1} to 750 °C in a 10 ml min^{-1} flow of Ar or 10% v/v NO/Ar. In parallel, evolved gas analysis was performed with a quadrupole Pfeiffer Omnistar mass spectrometer, which was connected to the outlet of the TGA apparatus. Ion currents were recorded for *m/z* values (*m* = molar mass of X^{z+} ion, *z* = charge of the ion) of 14, 15, 16, 17,

18, 28, 30, 32, 44, 46, 62 and 63.

Ex situ thermal treatment and characterization

Typically, 100 mg of SBA-15 impregnate was heated with a ramp of 1 °C min^{-1} to 300-500 °C (depending on the nitrate) in a 100 ml min^{-1} flow of air or 1% v/v NO/Ar. Thermal treatment in both air and Ar lead to significant agglomeration.[9] The resulting SBA-15 supported oxides were analyzed with powder X-ray diffraction (XRD) and transmission electron microscopy (TEM). XRD patterns ranging from 10 to 80° 2θ were obtained at room temperature with a Bruker-AXS D8 Advance X-ray Diffractometer setup using Co-$K_{\alpha 1,2}$ radiation. The average metal oxide crystallite size was calculated using the Debye-Scherrer equation on the most intense diffraction lines. TEM images were obtained on a Tecnai 20 operating at 200 keV.

Results and discussion

Impact of NO on the temperature of decomposition

In a previous communication it was shown that NO affects the decomposition temperature of nickel nitrate.[11] However, in this case a drying treatment at 120°C had been applied prior to the measurements, and hence the first hydrolysis step to nickel hydroxynitrate had already (partly) occurred. Here, we investigate the impact of NO on the temperature of decomposition of the metal nitrate hydrate, using TGA and MS. Figure 1 shows the TGA and MS results for the thermal treatment of Ni/SG in NO and Ar. The DTA plot, calculated from the TGA signal by taking the derivative, combines the weight-loss steps with the nature of the evolved gasses detected with MS. The temperature of decomposition (T_d) was determined from the MS results (Figure 1) by measuring the onset of the first NO/NO_2 evolution peak. The NO (*m/z=30*) signal was used for the Ar thermal treatment because of its high intensity, but for the NO thermal treatment NO_2 (*m/z=46*) was used because of the high NO background signal. In Figure 2 an overview is given of the T_ds of the investigated nitrates.

In general the T_d values found in this study are lower than reported previously, which may be ascribed to the presence of the support.[12] In the Ar treatment a clear trend in the T_d is observed; with the exception of scandium and iron nitrate, the T_d gradually decreases going from the left to right in the periodic table, which can be explained by the decreasing radius of the divalent metal cations. Scandium and iron are trivalent cations and therefore have a smaller cation radius compared to the divalent cations, which decreases the pK_a and thus facilitates hydrolysis to the metal hydroxynitrate. The hydrolysis reaction is depicted for copper nitrate in Equation 1.

$$2Cu(NO_3)_2 \bullet 3H_2O \rightarrow Cu_2(OH)_3NO_3 + 3HNO_3 + 3H_2O \quad (1)$$

The presence of NO decreases the T_d to below 100 °C for all investigated metal nitrates. We propose the decrease in T_d results from the facilitated decomposition of HNO_3 formed during hydrolysis, which will be further explained in Chapter 3.

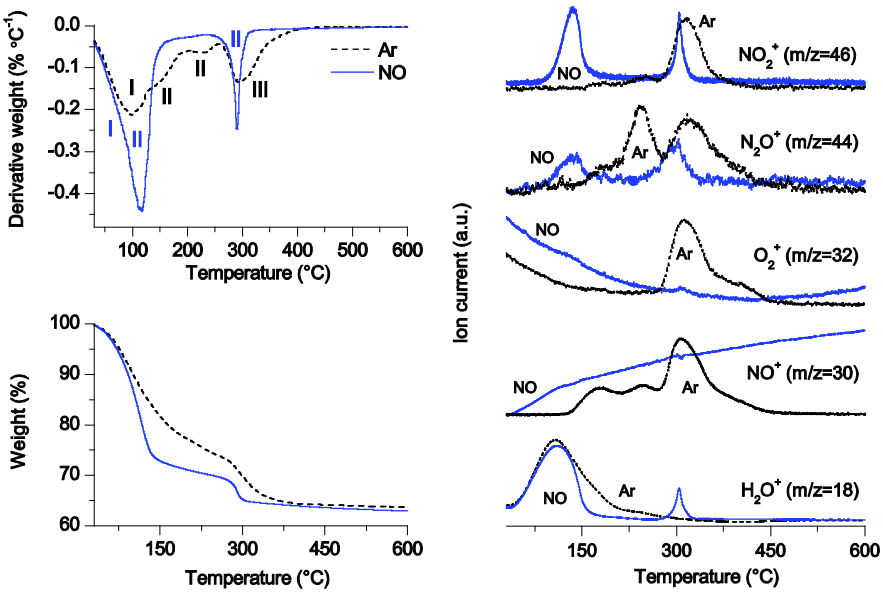

Figure 1. TGA (left, bottom), DTA (left, top) and MS (right) traces of nickel nitrate Ni/SG during thermal treatment in Ar (…) and NO (—).Gas evolution indicated as; I: H_2O, II: H_2O + NO_x, III: NO_x.

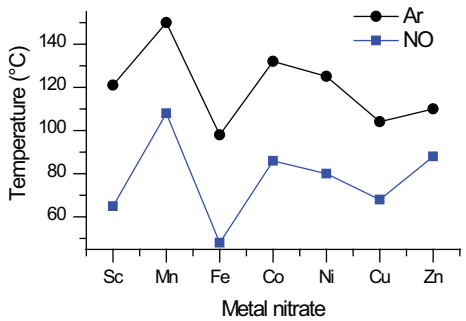

Figure 2. Temperature of the low temperature decomposition of SG supported metal nitrates during thermal treatment in 10% v/v NO/Ar (■) or Ar (●). Derived from the onset of the first NO/NO_2 evolution peak.

Impact of the gas atmosphere on the dispersion

The *ex situ* thermally treated samples were characterized using XRD and TEM. SBA-15 was chosen as a support because in this case TEM analysis yields more information. Of all investigated metal oxides only cobalt, nickel and copper oxide showed diffraction lines, indicating the other oxides were either amorphous or the particles too small to detect. For SBA-Co and Ni large differences between the air and NO thermal treatments were observed both with XRD and TEM (data not shown), in agreement with previous reports.[10-11] Air calcination resulted in broad particle size distributions and large average crystallite sizes, whereas NO thermal treatment yielded small particles with narrow size distributions (Table 2).

Table 2. Metal oxide crystallite sizes as obtained from XRD

sample	**particle size** (nm)	
	air	NO
SBA-Co	10	5
SBA-Ni	12	4
SBA-Cu	23	7

The large difference in CuO crystallite size calculated from XRD we report here for the first time. Although XRD suggests there is a large difference in CuO dispersion, both thermal treatments yield high dispersions, which will be explained in Chapter 6.

Impact of the gas atmosphere on the decomposition pathway

Scandium, manganese, iron and zinc nitrate

The DTA curves of the decomposition of SG-Sc, SG-Mn, SG-Fe and SG-Zn are shown in Figure 3. The gas evolution, as determined from the MS traces, is indicated in the curve as follows; I: H_2O, II: $H_2O + NO_x$ and III: NO_x. Manganese and iron nitrate decompose well below 200°C in Ar, where the first decomposition step involves only dehydration (I) and the second both dehydration and nitrate decomposition (II), in agreement with literature.[2,13] The limited stability of iron nitrate may be ascribed to the small radius and high valency, resulting in destabilization of the nitrate anion (*vide supra*). However, the radius of Mn^{2+} is comparable to Co^{2+} and Cu^{2+}, but still it decomposes at a significantly lower temperature. A possible explanation could be a difference in the extend of back donation. It is reported that transition metal nitrates decompose at lower temperatures than alkali metal nitrates with a similar charge

density, because of back-donation of d-electrons to empty π*-orbitals of the nitrate anion.[14] The presence of NO shifts the second decomposition step (II) to lower temperatures, now almost coinciding with the dehydration step (I).

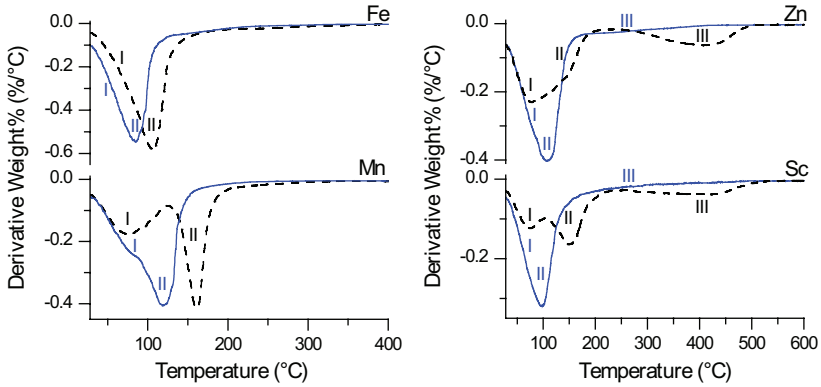

Figure 3. DTA curves of the decomposition of iron, manganese, zinc and scandium nitrate in Ar (…) and 10% v/v NO/Ar (—). Gas evolution indicated as; I: H_2O, II: H_2O + NO_x, III: NO_x.

In contrast, scandium and zinc nitrate show three step decomposition. After partial dehydration (I), both dehydration and nitrate decomposition occurs in the 100-200 °C temperature range (II). The last decomposition step occurs much high temperatures (200-500 °C) with only NO_x evolution and no significant water evolution (III). All steps are broad and continuous such that no intermediates can be identified. For zinc nitrate hydrolysis to $Zn(NO_3)_2 \cdot 2Zn(OH)_2$ has been proposed as the first decomposition step,[15] but the absence of water evolution at higher temperatures suggests anhydrous zinc nitrate was also formed. Moreover the significant evolution at higher temperatures suggests these species to be more stable than reported previously.[12,15-16] A likely explanation is the factor ten higher flow rate used in literature. A higher flow rate, i.e. faster removal of decomposition gasses, might accelerate decomposition.

The decomposition of supported scandium nitrate hydrate has not been reported before, therefore no comparison to literature can be made. In general the decomposition patterns of scandium nitrate and zinc nitrate are more similar to that of main group metal nitrates such as potassium and calcium nitrate, which typically display decomposition over a very broad temperature range.[14,17] The resemblance in behaviour between scandium and zinc, and non d-metal nitrates is possibly explained by their empty and full d-shell, respectively, resulting in a lower extent of back bonding between the metal ion and the nitrate. An additional explanation involves the fact that molecular oxygen has to evolve to complete the decomposition, and that

the combination of two oxygen radicals to O_2 is more efficiently catalyzed by oxides such as CuO, Mn_2O_3, Fe_2O_3 and NiO than ZnO and likely Sc_2O_3.[18] As a consequence the decomposition is not accelerated by the increasing oxide formation. For both scandium and zinc nitrate the presence of NO during decomposition shifts the decomposition steps involving NO_x evolution to lower temperatures, causing the first two decomposition steps in the 25-100 °C temperature range to overlap. The high temperature (III) decomposition step is also shifted to lower temperatures, but stretches over a larger temperature range.

Due to the amorphous nature of the metal oxides, no conclusion can be drawn regarding the difference in particle size distribution. However, no large agglomerates were observed for all samples indicating high dispersions were likely obtained in all cases.

Cobalt, nickel and copper nitrate

For this group of metal nitrates the difference between NO and Ar thermal treatment is much more apparent than for the other investigated metal nitrates (Figure 4). Decomposition in Ar results in all cases in a broad multi-step NO/NO_2 evolution ranging between 100-400 °C. Several intermediates have been reported, including several dehydration stages and metal hydroxynitrates.[4,19-20] However, the broad pattern suggests multiple phases are present. Heat treatment in NO on the other hand results in rapid hydrolysis of the metal nitrate to its respective metal hydroxynitrate. This was confirmed with *in situ* XRD and IR (Figure 5), which show the presence of metal hydroxynitrates (a hexagonal layered structure, and a strong ν_{OH} band around 3600 cm^{-1}). A more detailed description of this IR and XRD study is given in Chapter 3 and 6. This phase is then stable over a certain temperature range before decomposing to the metal oxide in a single sharp step (with the exception of the two step decomposition of copper hydroxynitrate to CuO).

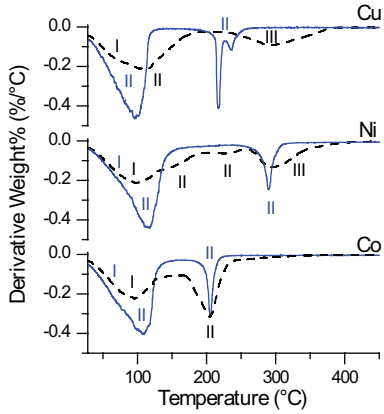

Figure 4. DTA curves of the decomposition of cobalt, nickel and copper nitrate in Ar (…) and 10% v/v NO/Ar (—). Gas evolution indicated as; I: H_2O, II: H_2O + NO_x, III: NO_x.

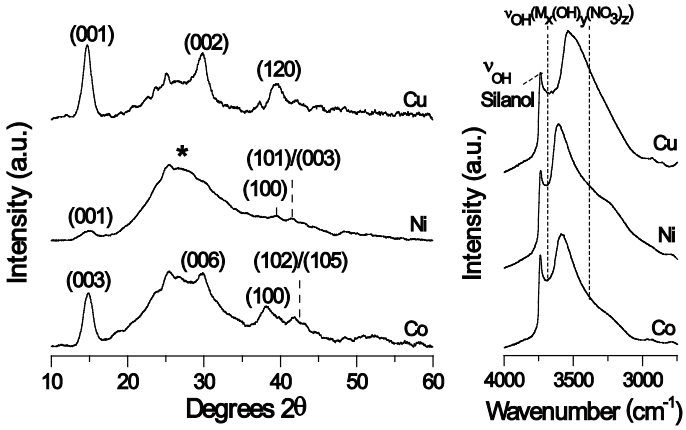

Figure 5. XRD patterns (left) and IR spectra (right) of copper, nickel and cobalt hydroxynitrate formed at 150 °C in 10% v/v NO/Ar.

Even though the decomposition is much faster in the presence of NO, in all cases the agglomeration is significantly reduced (Table 2). Metal hydroxynitrates bear close resemblance to metal hydroxides, which are generally less prone to agglomeration than metal nitrate hydrates. It is therefore postulated that the formation of highly dispersed hydroxynitrates is the key to the high dispersion obtained in NO, which will be further discussed in Chapter 3. In several previous reports hydroxynitrate formation resulted in the formation of very large copper oxide particles. An explanation for the apparent discrepancy is the high dispersion of the metal hydroxynitrate phase formed in NO (<10 nm crystal domains, Figure

5), in contrast to the large (>25 nm) copper hydroxynitrate crystal domains that are typically observed after drying at 120 °C in stagnant air.[5]

Conclusions

The impact of NO on the decomposition pattern and dispersion of first row transition metal nitrates was investigated using TGA-MS, XRD and TEM. The presence of NO lowered the temperature of decomposition significantly for all investigated metal nitrates. For cobalt, nickel and copper nitrate it was verified that the presence of NO during decomposition led to an improved metal oxide dispersion, where decomposition in Ar resulted in agglomeration. It was found that NO, in contrast to Ar, induced rapid hydrolysis of cobalt, nickel, and copper nitrate to highly dispersed metal hydroxynitrates, which was ascribed to a decrease in the decomposition temperature of nitric acid, the product of the hydrolysis. Hence, we show that NO affects the decomposition over the whole temperature range.

Acknowledgements
The authors kindly thank Marjan Versluijs and Fred Broersma for their help with the TGA-MS experiments and Cor van der Spek for the TEM analysis. Johnson Matthey Catalysts is acknowledged for the financial contribution to this work and Steve Pollington and John Casci for their scientific contributions.

References

1. Paulik, F.; Paulik, J.; Arnold, M. *Thermochim. Acta* **1987**, *121*, 137.
2. Elmasry, M. A. A.; Gaber, A.; Khater, E. M. H. *J. Therm. Anal. Calorim.* **1998**, *52*, 489.
3. Estelle, J.; Salagre, P.; Cesteros, Y.; Serra, M.; Medina, F.; Sueiras, J. E. *Solid State Ionics* **2003**, *156*, 233.
4. Llewellyn, P. L.; Chevrota, V.; J. Ragaib; Cerclier, O.; Estienne, J.; Rouquerol, F. *Solid State lonics* **1997**, *101-103* 1293.
5. Toupance, T.; Kermarec, M.; Louis, C. *J. Phys. Chem. B* **2000**, *104*, 965.
6. Chouillet, C.; Villain, F.; Kermarec, M.; Lauron-Pernot, H.; Louis, C. *J. Phys. Chem. B* **2003**, *107*, 3565.
7. Catillon-Mucherie, S.; Ammari, F.; Krafft, J. M.; Lauron-Pernot, H.; Touroude, R.; Louis, C. *J. Phys. Chem. C* **2007**, *111*, 11619.
8. van de Loosdrecht, J.; Barradas, S.; Caricato, E. A.; Ngwenya, N. G.; Nkwanyana, P. S.; Rawat, M. A. S.; Sigwebela, B. H.; van Berge, P. J.; Visagie, J. L. *Top. Catal.* **2003**, *26*, 121.
9. Sietsma, J. R. A.; Meeldijk, J. D.; Versluijs-Helder, M.; Broersma, A.; van Dillen, A. J.; de Jongh, P. E.; de Jong, K. P. *Chem. Mater.* **2008**, *20*, 2921.
10. Sietsma, J. R. A.; Meeldijk, J. D.; den Breejen, J. P.; Versluijs-Helder, M.; van Dillen, A. J.; de Jongh, P. E.; de Jong, K. P. *Angew. Chem. Int. Ed.* **2007**, *46*, 4547
11. Sietsma, J. R. A.; Friedrich, H.; Broersma, A.; Versluijs-Helder, M.; van Dillen, A. J.; de Jongh, P. E.; de Jong, K. P. *J. Catal.* **2008**, *260*, 227.
12. Nissinena, T.; Leskel, M.; Gasika, M.; Lamminen, J. *Thermochim. Acta* **2005**, *427*, 155.
13. Wieczorek-Ciurowa, K.; Kozak, A. J. *J. Therm. Anal. Calorim.* **1999**, *58*, 647.
14. Yuvaraj, S.; Fan-Yuan, L.; Tsong-Huei, C.; Chuin-Tih, Y. *J. Phys. Chem. B* **2003**, *107*, 1044.
15. Malecka, B.; Gajerski, R.; Malecki, A.; Wierzbicka, M.; Olszewski, P. *Thermochimica Acta* **2003**, *404*, 125.
16. Cseri, T.; Békássy; Kenessey, G.; Liptay, G.; Figueras, F. *Thermochim. Acta* **1996**, *288*, 137.
17. Ettarh, C.; Galwey, A. K. *Thermochim. Acta* **1996**, *288*, 203.
18. Dickens, P. G.; Sutcliffe, M. B. *Trans. Faraday. Soc.* **1964**, *60*, 1272.
19. Brockner, W.; Ehrhardt, C.; Gjikaj, M. *Thermochim. Acta* **2007**, *456*, 64.
20. Malecki, A.; Gajerski, R.; Labus, S.; Prochowska-Klisch, B.; Wojciechowski, K. T. *J. Therm. Anal.* **2000**, *60*, 17.

Chapter 3

NO-Induced Low Temperature Immobilization of Silica-Supported Cobalt and Nickel Nitrate

Abstract: Impregnation of porous silica supports with cobalt and nickel nitrate precursor solutions is a convenient method to prepare supported nickel and cobalt (oxide) catalysts. However, the metal (oxide) dispersion that is obtained is highly dependent on the gas atmosphere during the thermal treatment. The role of nitric oxide in the prevention of agglomeration of nickel and cobalt nitrate at low temperatures (25-150 °C) was studied using *in situ* DRIFTS and XRD. It was found that in an N_2 or O_2/N_2 flow a mixture of metal (hydroxy)nitrate hydrates were formed between 100 and 150 °C, whereas in the presence of NO nearly complete hydrolysis to anhydrous hydroxynitrates occurred. The anhydrous nickel and cobalt hydroxynitrates were shown to exhibit a severely reduced mobility upon decomposition and, therefore, it is proposed that their increased formation is the key to the high NiO and Co_3O_4 dispersions obtained in NO.

Introduction

Supported nickel and cobalt nanoparticles are efficient catalysts that are frequently applied in large industrial processes such as steam reforming, the hydrogenation of edible oils, methanation, hydrotreating, and the Fischer-Tropsch synthesis.[1-3] The method by which these materials are prepared directly influences their physical properties and thus determines their activity, selectivity and stability. Although the number of fundamental studies on the physico-chemical processes that take place during preparation is increasing,[4-18] many processes that take place are still not fully understood.

Impregnation of porous supports, such as silica and alumina, with metal nitrate precursors is a facile and cost effective method to prepare supported catalysts that produces only small waste streams and is, therefore, a preferred route in both academia and industry. However, the use of metal nitrates commonly results in poor metal oxide dispersions, which has been ascribed to agglomeration during the thermal decomposition step in air.[19-21] Several approaches to prevent agglomeration have been reported, ranging from the addition of chelating or viscosity increasing agents to tuning of the gas and temperature profiles.[9,11,21-26] Other successful approaches are the direct reduction[12,27-28] and glow discharge plasma assisted decomposition metal nitrates.[18] A highly effective method to prevent agglomeration is the replacement of the air flow during the calcination step by a 1% v/v NO/He flow.[28] Since this discovery, we have shown that during the nitrate decomposition rate, NO facilitates N-O bond cleavage, moderates the decomposition and scavenges oxygen radicals.[29-32] Similar observations were made with H_2 and N_2O, indicating the oxygen scavenging ability was essential to obtain high dispersions. However, the origin of the reduced mobility of the metal nitrate in the presence of NO still remained unclear. Conventional drying of silica-supported nickel nitrate at 120 °C prior to the calcination results in partial conversion of the nickel nitrate hexahydrate into nickel hydroxynitrate as shown in Equation 1.[29]

$$3[Ni(H_2O)_6](NO_3)_2\ (aq) \rightarrow Ni_3(NO_3)_2(OH)_4\ (s) + 4HNO_3\ (g) + 14H_2O\ (g) \qquad (1)$$

In Chapter 2 we have shown that NO already affects the phase evolution of cobalt and nickel nitrate below 120 °C. Therefore, we conducted the present study on silica supported nickel and cobalt nitrate hydrate dried at room temperature. Using *in situ* DRIFTS and XRD we will show that the role of NO in the prevention of agglomeration is two-fold. It's major role is at low temperatures (<150 °C), where the presence of a diluted NO/He flow during thermal treatment results in the nearly complete conversion of the highly mobile nickel and cobalt nitrate hydrate phases

into their hydroxynitrate counterparts. We will show that these hydroxynitrate phases exhibit a reduced mobility, even during a normally detrimental calcination in stagnant air. Still the agglomeration is further reduced by the continued presence of NO at high temperatures, which is discussed in more detail in Chapter 4.

Experimental

Sample preparation

SBA-15 (BET surface area. = 695 $m^2 g^{-1}$; pore volume = 0.77 $cm^3 g^{-1}$; pore diameter = 9.6 nm) was prepared according to the procedure outlined by Zhao et al.[33]. SBA-15 supported nickel and cobalt nitrate were prepared by impregnating small quantities of SBA-15 to incipient wetness with aqueous solutions of nickel nitrate hexahydrate (4.3M) and cobalt nitrate hexahydrate (3.0M), respectively. Following subsequent equilibration of an hour, the samples were transferred into a dessicator, containing 4Å molecular sieves, to remove water at ambient temperature from the sample while keeping the metal nitrate hydrate intact. The samples were labelled Ni/SBA and Co/SBA, respectively.

Characterization

Characterization of the samples was performed using Powder X-ray Diffraction (XRD), N_2-Physisorption, *in-situ* Diffuse Reflectance Infrared Fourier Transform Spectroscopy (DRIFTS) and Transmission Electron Microscopy (TEM). N_2 physisorption measurements were performed at -196 °C using a Micromeritics Tristar 3000 apparatus. Prior to analysis, samples were dried in a N_2 flow for 14 hours at 300 °C. Non-local density functional theory (NL-DFT) was used to derive the pore size distribution from the adsorption branch of the isotherm.[34] TEM images were obtained on a Technai 12 apparatus, operated at 120 keV. Powder XRD patterns were recorded with a Bruker-AXS D8 Advance 120 X-ray Diffractometer using Co-Kα_{12} radiation (λ = 1.78897 Å) at room temperature. Average crystallite sizes were calculated using the Debye-Scherrer equation (K=1) on the most intense diffraction lines at $2\theta = 50.7°$ and 43.1° for nickel and cobalt oxide, respectively. For *in situ* XRD experiments the diffractometer was equipped with an Anton-Paar XRK reaction chamber and the dried impregnate (40 mg) was heated to 350 °C (heating rate: 1 °C·min^{-1}) in a 10% v/v O_2/N_2 flow or in a 10% v/v NO/He flow (90 ml·min^{-1}).

In situ DRIFT measurements were performed with a Bruker Tensor 27 apparatus utilising a HVC-DRP-3 Diffuse Reflectance Reaction Chamber with CaF_2 windows and a high sensitivity liquid N_2 cooled MCT detector. In order to restrict temperature gradients within the sample due to the poor thermal conductivity of

the silica support, the bottom of the sample cup was filled with silicon carbide. To prevent contamination of the sample, a grid was placed on top of the SiC, creating a cup of about 1 to 2 mm deep for the actual sample (±15 mg). Non adsorbing KBr background scans were taken at 25 °C. The flow rate during all experiments was 10 ml·min^{-1} and the gas was flowed through the sample from top to bottom. The different gases used during experiments were N_2, 20% v/v O_2/N_2, 10% v/v NO/He and 1% v/v NO/9% v/v He/90% v/v N_2. Spectra were recorded every two minutes from 4000 to 1000 cm^{-1} as the accumulation of 50 scans at a resolution of 4 cm^{-1}. In a typical experiment the cell was first flushed with N_2 at 25 °C for 10 minutes, followed by the introduction of the gas flow to be used in the experiment, which was given 10 minutes to fully equilibrate. After this time, the temperature was raised to 350 °C with a ramp of 1 °C·min^{-1}.

Solubility and mobility of the nickel phases after drying

After impregnation with a 4.3M aqueous Nickel nitrate solution as described above, the impregnate was divided into three portions. A first sample was dried in a flow of 5% v/v NO/Ar for 3 hours at 150 °C. A second sample was dried similarly, but in flow of N_2 instead of 5% v/v NO/Ar. The third sample was dried in stagnant air at 150 °C for 18 hours, the long duration to promote completion of the hydrolysis step. The samples were labelled SBA-D_{NO}, SBA-D_{N2} and SBA-D_{air}, respectively. Next, the dried samples were split in two portions. The first part was redispersed in demineralised water for 10 minutes, filtered and dried in stagnant air at 120 °C, and the second was used as such. Small quantities (±400 mg) of the parent and redispersed impregnates were subsequently calcined in stagnant air at 350 °C for 1 hour. The nickel content of all samples was determined with X-ray Fluorescence. The calcined samples were labelled -RC and -C for the redispersed and directly calcined samples, respectively.

Results

In situ XRD

After impregnation the SBA-15 supported nickel and cobalt nitrate samples were dried in a dessicator at ambient temperature. The extent to which the samples were dried was determined from the weight loss, which indicated that over 85% of the solvent water was removed. The evolution of the crystalline phases during heating from 25 to 350 °C in 10% v/v O_2/N_2 and 10% v/v NO/He was studied with *in situ* XRD (Figure 1-3). In an O_2/N_2 flow the nitrate phases were amorphous and only crystalline metal oxide phases, i.e. NiO and Co_3O_4, were observed (Figure 1). After

the thermal treatment the average NiO and Co_3O_4 crystallite sizes were calculated from the diffraction line broadening using the Debye-Scherrer equation, and were 12 and 10 nm, respectively.

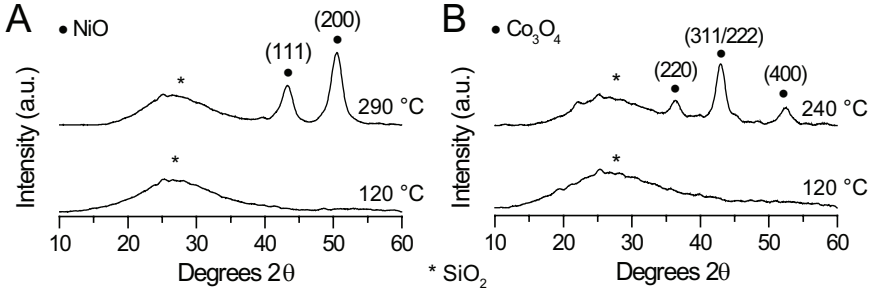

Figure 1. XRD patterns recorded during thermal treatment of Ni-SBA-15 (A) and Co-SBA-15 (B) in 10% v/v O_2/N_2.

In an NO/He flow (Figure 2), diffraction patterns typical for double layered nickel and cobalt hydroxide were observed between 60-225 °C, prior to the appearance of the metal oxide phase.[34-36] The diffraction patterns correspond very well to those of $Ni_3(OH)_4(NO_3)_2$ and α-$Co_2(OH)_3NO_3$. These isostructural compounds have a hexagonal unit cell in which the metal ions are octahedrally surrounded by hydroxyl and nitrate groups. However, this assignment is not fully unambiguous as double layered hydroxides are often non-stochiometric and the exact composition is highly dependent on the preparation method.[34,37] Furthermore, only crystalline materials are observed with XRD, while amorphous phases may also be present. Examples of similar compounds that could be present as amorphous phases include; $Ni_3(OH)_4(NO_3)_2$,[34] $Ni_2(OH)_3(NO_3)$,[36] $Ni(OH)(NO_3)\cdot H_2O$,[38] $Co_2(OH)_3(NO_3)\cdot 0.25H_2O$,[3,9] $Co_7(OH)_{12}(NO_3)_2\cdot 5H_2O$,[39] $Co(OH)(NO_3)\cdot H_2O$[40-41] and $Co_3(OH)_4(NO_3)_2$.[42] This issue will be addressed in more detail below. The diffraction pattern of $Ni_3(OH)_4(NO_3)_2$ was in agreement with previously reported samples that were dried at 120 °C in stagnant air for 18 h, although the diffraction lines in Figure 2 are much broader and the intensities lower.[27] Likely, most of the material was not well crystallized in view of the short duration. For the cobalt sample more intense diffraction lines corresponding to 9 nm α-$Co_2(OH)_3NO_3$ crystal domains were observed. In addition to the formation of an intermediate phase, the presence of NO also yielded very broad metal oxide diffraction lines indicating very small average NiO (3 nm) and Co_3O_4 (5 nm) crystal domains had formed.

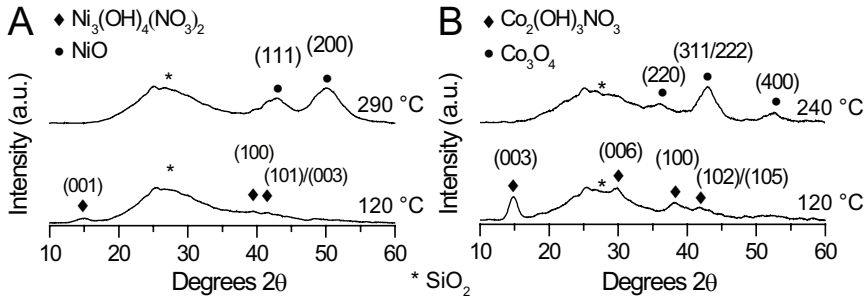

Figure 2. XRD patterns recorded during thermal treatment of Ni-SBA-15 (A) and Co-SBA-15 (B) in 10% v/v NO/He.

Figure 3 depicts the normalized intensity as a function of temperature for the most intense diffraction lines of $Ni_3(OH)_4(NO_3)_2$, $Co_2(OH)_3NO_3$, NiO and Co_3O_4, centred at 14.8, 14.9, 50.7 and 43.1 °2θ, respectively. For both metals the hydroxynitrate phase appeared between 60-80 °C in an NO/He flow and was more stable than the metal nitrate phase that was formed in an O_2/N_2 flow, as apparent from the higher temperature at which the metal oxide is formed. From these results it can be concluded that NO induces the formation of small metal hydroxynitrate crystallites and, as previously reported, increases the final metal oxide dispersion.

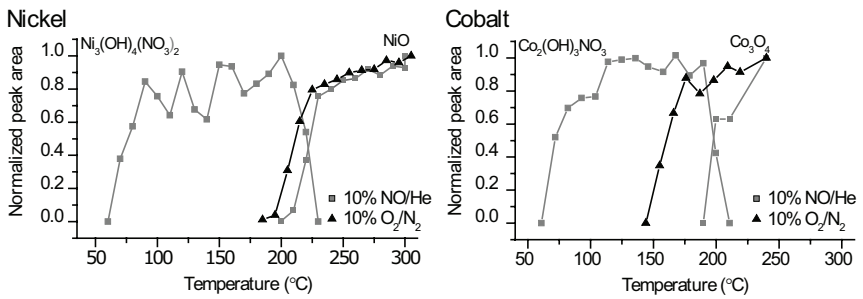

Figure 3. Normalized XRD peak areas of the different crystalline phases as a function of temperature for the thermal treatment of silica supported nickel and cobalt nitrate in 10% NO/He and 10% v/v O_2/N_2.

The much lower hydrolysis temperature in NO is remarkable. At 120 °C evaporation of water and nitric acid drives the equilibrium of Equation 1 towards the metal hydroxynitrate, but below the boiling point of both compounds this process is slow. We propose that the low temperature metal hydroxynitrate formation observed in the presence of NO occurs according to Equation 2, rather than Equation 1.

$$3[Ni(H_2O)_6](NO_3)_2\ (aq) + 2NO\ (g) \rightarrow Ni_3(NO_3)_2(OH)_4\ (s) + 6NO_2\ (g) + 16H_2O\ (g) \quad (2)$$

The difference in ΔG^0 between Equation 1 and 2 was estimated by calculating the Gibbs free energy of the decomposition of HNO_3 via a reaction with NO. Using HSC chemistry for windows 4.1 it was found that the ΔG^0 for Equation 2 was approximately 23 kJ mol^{-1} (based on one mol of nickel nitrate hydrate) lower than for Equation 1, showing that hydrolysis to the metal hydroxynitrate will occur at lower temperatures in the presence of NO. As XRD only shows the crystalline intermediates, and the diffraction lines for nickel hydroxynitrate are very weak, the phase evolution will be further investigated using DRIFT spectroscopy.

DRIFT spectroscopy

To validate comparison of the *in situ* XRD and DRIFTS measurements, XRD patterns were taken after the *in situ* thermal treatments at 350 °C in the IR apparatus. The average crystallite sizes were determined using Debye-Scherrer line broadening analysis. The NiO and Co_3O_4 crystallite size obtained after *in situ* XRD and DRIFTS measurements were of comparable size, justifying comparison of the results (Table 1).

Table 1. NiO and Co_3O_4 crystallite sizes obtained after thermal treatment

sample	**size** (nm)[a]				
	in situ XRD		*in situ* DRIFTS		
	10% O_2/N_2	10% NO/He	20% O_2/N_2	10% NO/He	N_2
Ni-SBA	12	3	12	3	8
Co-SBA	10	5	10	6	8

[a]determined via XRD line broadening analysis

Nickel nitrate

Figure 4 depicts the DRIFT spectra taken of the hydroxyl and nitrate region during thermal treatment in N_2, 1% v/v NO and 10% v/v NO. Although there is a significant difference in the dispersion obtained in 20% v/v O_2/N_2 and N_2, there is no significant difference in phase evolution. We will therefore only discuss the N_2 treatment. In the hydroxyl region shown between 3900-2700 cm^{-1}, the broad O-H band indicates the samples still contain a large amount of water. The sharp band at 3740 cm^{-1} is characteristic for silanol groups on the silica support. The spectrum between 1900 and 1350 cm^{-1} shows the evolution of the characteristic nitrate stretch frequencies. At 25 °C a peak, which can be ascribed to the $\nu_4(-ONO_2)$ vibration, is found at 1460

cm^{-1}. In literature a single band at 1390 cm^{-1} is reported for free nitrate groups in bulk nickel nitrate hydrate, whereas here the band shows a small degree of splitting (the 1350 cm^{-1} peak is not visible here due to the large silica absorption).[43-44] This splitting resulted from a change in symmetry from $3D_h$ to C_{2v}, which may have been caused by the presence of the support or partial dehydration.

Around 120 °C in N_2 a strong and sharp band appears at 3610 cm^{-1}, which is characteristic for isolated hydroxyl groups in hydroxynitrates.[34,36,43,45] Simultaneously the $\nu_4(-ONO_2)$ band at 1460 cm^{-1} shifts to 1550 cm^{-1}, closely resembling the frequency reported for $Ni_3(OH)_4(NO_3)_2$ and $Ni_2(OH)_3NO_3$.[34,36] Although the bands do not exactly match the frequencies reported for $Ni_3(OH)_4(NO_3)_2$ or $Ni_2(OH)_3NO_3$, these materials are usually non-stochiometric and depend on the preparation (*vide supra*).

Two weak bands at 3370 and 3290 cm^{-1} are visible above 200 °C. While this observation has been reported by Petrov et al. as well, no assignment was made and the nature of these bands is uncertain.[36] Likely the basic nitrate retained some crystal water, resulting in hydrogen bonded hydroxyl bands at lower frequencies.[46-48] The basic formula for hydroxynitrates is $x\text{Ni}(NO_3)_2{\cdot}y\text{Ni}(OH)_2{\cdot}zH_2O$, and several authors reported mono- or di-hydrated basic nickel nitrates as the predominant species during the decomposition of nickel nitrate hexahydrate.[34,49-50] Unfortunately, nickel hydroxynitrate hydrates such as $Ni_2(OH)_2(NO_3)_2{\cdot}2H_2O$ are poorly characterized in literature, making assignment difficult. However, spectra of the isostructural $Zn_2(OH)_2(NO_3)_2{\cdot}2H_2O$ phase shows similar features in the lower end of the hydroxyl region, unlike its anhydrous counterpart which shows only a single absorption band.[51] It is therefore likely that at least part of the nickel is present in the form of a hydrated nickel hydroxynitrate. As all peak positions and their evolution with temperature correspond very well to those found previously for SBA-15 supported nickel nitrate dried at 120 °C[31], we propose mixed hydrated and hydroxynitrate phases were formed during both treatments, albeit being mostly amorphous.

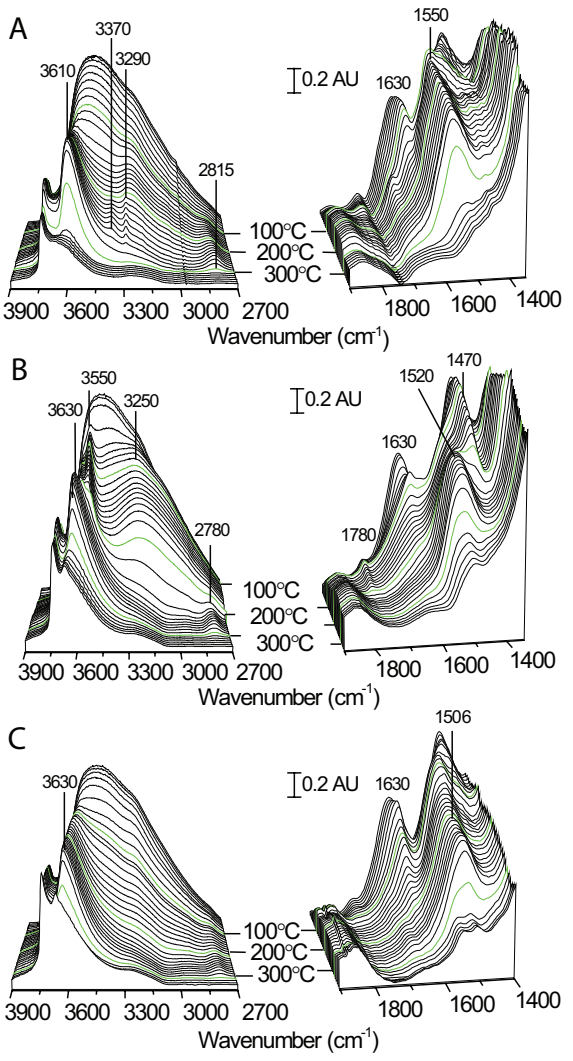

Figure 4. In situ DRIFT spectra of the OH region and nitrate region during the calcination of Ni-SBA in N_2 (A) and 1% v/v NO/He (B), 10% v/v NO/He (C).

In 1% v/v NO/He atmosphere the phase evolution is different from that in N_2. In addition to the appearance of a ν_{OH} band at 3630 cm^{-1} around 50 °C, a new peak at 3550 cm^{-1} arises around the same temperature, simultaneous with a broadening of the water band towards lower wave numbers. Furthermore, rather than gradually shifting to higher frequencies, the $\nu_4(-ONO_2)$ band remains at its initial position at 1470 cm^{-1}. As dehydration of the nickel nitrate hexahydrate, and thus further splitting of the ν_1

and ν_4 frequency, is inevitable at higher temperatures, it is likely that the new species responsible for the band at 3550 cm^{-1} is also responsible for a band around 1470 cm^{-1}. This explanation is supported by the simultaneous disappearance of the 3550 and 1470 cm^{-1} bands around 200 °C, where the latter is replaced by a band at 1520 cm^{-1}. Upon further heating the broad water band at 3200 cm^{-1} disappears. The peak at 3550 cm^{-1} matches very well with that of nitric acid in monomeric form[52-53], however, this does not explain the band at 1470 cm^{-1}. Furthermore, it is unlikely it would give rise to such a sharp peak in the presence of so much water. Isolated hydroxyl groups generally result in well defined bands in this region, where lower frequencies indicate increased hydrogen bonding and thus the presence of crystal water.[46-48] Therefore, we propose that the intermediate is a hydrated nickel hydroxynitrate that is converted into an anhydrous nickel hydroxynitrate at 200 °C. A very similar transformation has been reported for $Zn_2(OH)_2(NO_3)_2 \cdot 2H_2O$, which exhibited a similar intense but broad water band and two isolated hydroxyl bands.[51] Heating of this compound to 80-90 °C resulted in the further hydrolysis to $Zn_3(OH)_4(NO_3)_2$, which exhibited a single isolated hydroxyl band.

An increase in the NO concentration to 10% resulted in the direct conversion of nickel nitrate hexahydrate into anhydrous nickel hydroxynitrate, without formation of the proposed hydrated intermediate. In light of the differences between the measurements under NO and $(O_2/)N_2$, it is likely we observed a mono- or di-hydrated amorphous nickel hydroxynitrate phase in $(O_2/)N_2$, whereas NO has induced changes not only leading to a more crystalline, but also a fully dehydrated nickel hydroxynitrate phase. Comparing these results to those previously obtained with the sample that had been dried at 120 °C in stagnant air, a few differences should be noted. For the 120 °C dried sample (see Chapter 4) we observed a blue shift in the ν_{OH} frequency and a red shift in the $\nu_4(-ONO_2)$ frequency between 225-300 °C in the presence of NO, with the final peak positions at 3620 and 1525 cm^{-1}, respectively.[31] In the present work no shift is observed in this temperature range, rather, the spectrum in 10% v/v NO resembles that of the 120 °C-dried sample at 300 °C already at much lower temperatures (150 °C). This is in agreement with the direct decomposition to the anhydrous hydroxynitrate, rather than via a hydrated intermediate. It also implies the hydrated hydroxynitrate formed during drying at 120 °C is not so easily dehydrated as the hydrated hydroxynitrate observed during the 1% v/v NO/Ar thermal treatment, and that NO likely plays a different role in both cases.

Cobalt nitrate

Spectra of the thermal treatment of cobalt nitrate hexahydrate supported on SBA-15 in an N_2 and 1% v/v NO/He flow are shown in Figure 5. In both gasses the nitrate ν_4(O-NO_2) band has an initial frequency at 1460 cm^{-1}, which slowly shifts to higher frequencies at higher temperatures. In the presence of N_2 this frequency increases to 1550 cm^{-1}, while at 120 °C a shoulder is developed at 1590 cm^{-1} before decomposition takes place at 180 °C. A low intensity band is formed at 3575 cm^{-1} and around 3300 cm^{-1} the same water structure arises as was observed for nickel, which suggests some amorphous cobalt hydroxynitrate hydrate is formed. The intensity of these bands is very low, in agreement with the literature where basic cobalt nitrate formation is not observed under these conditions.[54-55] Instead, most of the cobalt nitrate hexahydrate is gradually dehydrated until the severely dehydrated or anhydrous cobalt nitrate decomposes into cobalt oxide.

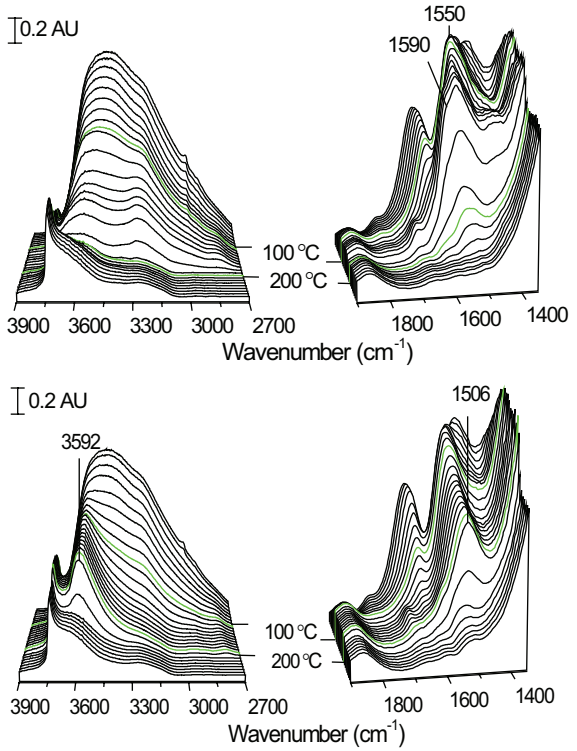

Figure 5. In situ DRIFT spectra of the OH region and nitrate region during the calcination of Co-SBA in N_2 (top) and 1% v/v NO/He (bottom).

In the presence of NO, a new band starts to form around 3592 cm^{-1} at 70 °C, indicating the formation of a new intermediate. In addition a single $\nu_4(O-NO_2)$ stretch vibration band is observed around 1506 cm^{-1} until decomposition starts around 210 °C. Similar to the nickel results a single sharp ν_{OH} band due to cobalt hydroxynitrate is observed, indicating the formation anhydrous cobalt hydroxynitrate. In the literature two distinct ν_{OH} bands at 3615 and 3525 cm^{-1} are reported for basic cobalt hydroxynitrate.[56] The band we observe is close to the average of the two reported, and can be explained by a change in morphology. $Co_2NO_3(OH)_3$ is known to have at least two modifications; an α-form with a hexagonal unit cell and a monoclinic β-form.[57] In its monoclinic form, the β-$Co_2NO_3(OH)_3$ has OH^- groups at different distances from Co^{2+}, giving rise to different bond strengths and therefore different IR frequencies, as observed by the two separate ν_{OH} bands in literature.[58] On the other hand, α-$Co_2NO_3(OH)_3$ is thought to be isostructural to the only hexagonal modification of $Ni_3(NO_3)_2(OH)_4$, which shows all OH^- groups at equal distances and thus at the same IR frequency. Therefore, observation of a single ν_{OH} band can be explained by formation of α-$Co_2NO_3(OH)_3$, which is in agreement with the XRD pattern. An increase in the NO concentration to 10% induced no further differences in the phase evolution and is, therefore, not discussed.

The relation between the dispersion and the phase evolution

In situ XRD and DRIFTS have shown that NO induces the hydrolysis of both cobalt and nickel nitrate hydrate to anhydrous hydroxynitrate, whereas much smaller amounts, and of a different nature, are formed in $(O_2/)N_2$. To determine the fraction of anhydrous nickel hydroxynitrates formed during drying and its impact on the dispersion, Ni/SBA-15 samples were dried at 150 °C in a flow of 5% v/v NO/Ar, N_2 or in stagnant air (Scheme 1).

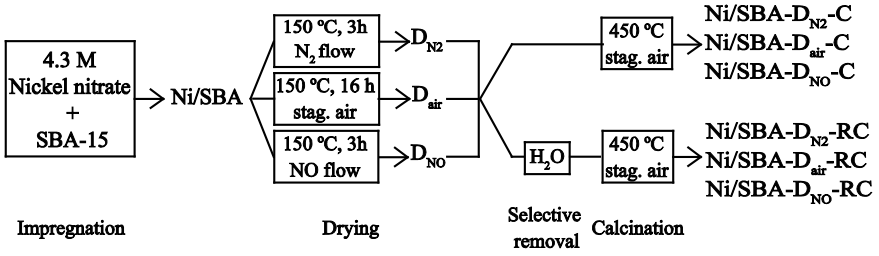

Scheme 1: Schematic overview of the different preparation steps.

Both the NO and air drying treatments resulted in intense nickel hydroxynitrate diffraction lines with a line width that indicated 9 nm crystallites

had been formed, whereas the sample dried in N_2 showed no diffraction pattern. After the drying treatment the samples were either directly calcined (Scheme 1, -C) in stagnant air or first re-dispersed in demineralised water, filtrated and dried prior to the calcination in stagnant air (Scheme 1, -RC). As anhydrous nickel hydroxynitrate is insoluble, in contrast to hydrated nickel (hydroxy)nitrate phases, the latter were selectively removed by dissolution. By comparing the nickel content, as determined by XRF, in the samples after calcination, the percentage of soluble species present after drying was determined.

Table 2 shows that drying in NO resulted in the smallest amount of soluble species (15%), whereas N_2 yielded the largest amount (75%). The difference in hydrolysis between drying in stagnant air (35% soluble) and an N_2 flow is in line with literature, where it is reported that efficient water removal, via a vacuum or gas flow, inhibits hydrolysis.[59-60] In addition, longer heating (16 h instead of 3 h) will also result in a higher degree of hydrolysis.

Table 2. Solubility after drying and NiO crystallite size after calcination in stagnant air

sample	**nickel nitrate fraction soluble in water** (%)	**size*** (nm)
Ni/SBA-D_{N2}-C	75	32
Ni/SBA-D_{N2}-RC	75	#
Ni/SBA-D_{air}-C	35	14
Ni/SBA-D_{air}-RC	35	7
Ni/SBA-D_{NO}-C	15	9
Ni/SBA-D_{NO}-RC	15	4

*Determined from XRD. #No diffraction lines detected

The high fraction of anhydrous nickel hydroxynitrates obtained in NO is in good agreement with the XRD and IR results. The impact of the degree of hydrolysis after drying on the dispersion after calcination is tremendous, as can be observed from Table 2. The average crystallite size decreases with the degree of hydrolysis, ranging from 32 nm for samples dried in N_2 to 9 nm for samples dried in NO. TEM (Figure 6-A) confirmed that drying in N_2 resulted in severe redistribution during calcination, which lead to a very broad particle size distribution that ranged from long NiO rods, confined by the 9 nm pores, to 150 nm crystals on the external surface. Prolonged drying in stagnant air reduced the migration during calcination slightly, but still resulted in a very wide particle size distribution (9-110 nm, see Figure 6-B). In contrast, drying in NO almost exclusively yielded short rods confined within the pores (Figure 6-C).

Thus, we have shown that the formation of anhydrous nickel hydroxynitrate during drying in the presence of NO prevents "long range" redistribution and significantly reduces agglomeration. However, it must be noted that intra-porous aggregation had still occurred to some extent. A schematic overview of the effect of the drying treatment on the dispersion is given in Figure 7.

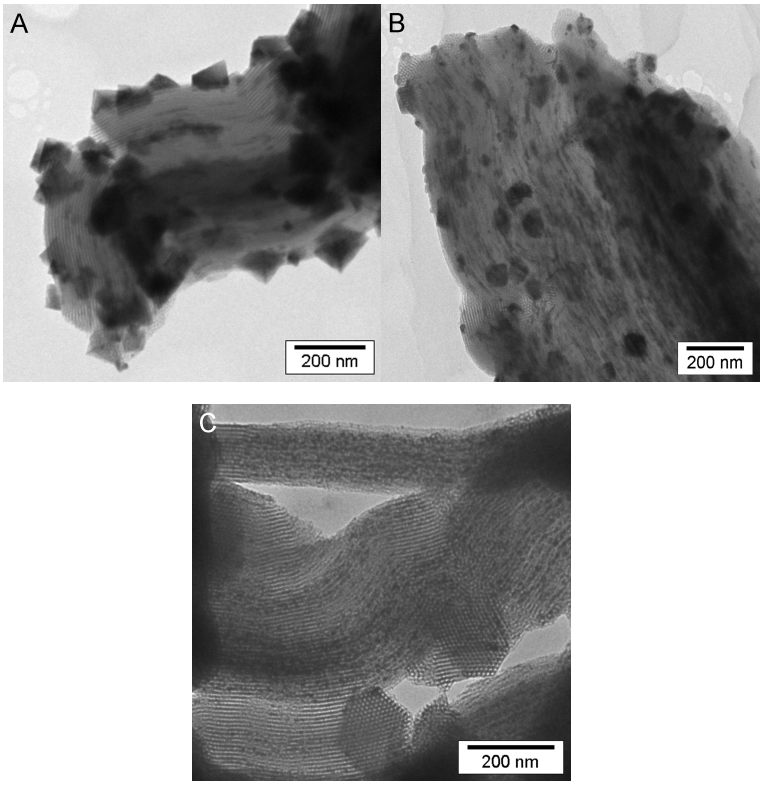

Figure 6. TEM images of NiO/SBA-15 samples after drying at 150 °C in A) N_2, B) stagnant air and C) 5% v/v NO/Ar, followed by a calcination in stagnant air.

For both the air and NO dried samples, the selective removal step lowers the average crystallite size after calcination (Table 2). This again confirms the contribution of the readily soluble species to the long range agglomeration, although a positive influence of the second drying step after the selective removal or the reduced metal loading cannot be fully excluded. Remarkable is the difference in crystallite size between the Ni/SBA-D_{air}-RC and Ni/SBA-D_{NO}-RC samples. The Ni/SBA-D_{NO}-RC sample has an average NiO crystallite size of 4 nm that is close to the value obtained after full NO thermal treatment (Table 1), whereas the Ni/SBA-D_{air}-RC sample has

an average NiO crystallite size of 7 nm. Thus, if nearly complete hydrolysis occurs during drying in NO, an additional effect of NO at high temperatures is limited. A possible explanation for the larger crystallite size (7 nm) observed for the Ni/SBA-D_{air}-RC sample is that the proposed more mobile hydrated nickel hydroxynitrate in the centre of the long SBA-15 pore system is not so readily removed.

Although a selective removal step prior to the calcination is an effective method to increase the dispersion, a high temperature thermal treatment in NO is both more facile and desirable, because it yields higher loadings and smaller waste streams. We can now speculate on the role of NO at higher temperatures (150-350 °C). For a sample dried in NO, we propose this role is small, facilitating completion of the hydrolysis around 200 °C, as no further changes in the spectra are observed from this point on. For a conventionally dried sample (120-150 °C in stagnant air) on the other hand, changes in the maxima of the ν_{OH} and $\nu_4(-ONO_2)$ bands are only observed above 200 °C.[31] In Chapter 4 it will be proposed that in this case oxygen scavenging by NO, which induces low temperature NiO nucleation, is the dominating mechanism by which agglomeration of nickel nitrate is prevented.

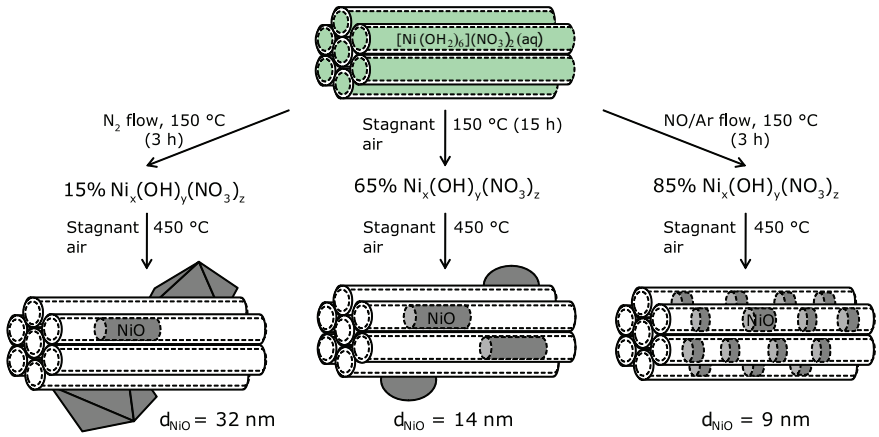

Figure 7. Schematic overview of the impact of the drying treatment on the hydrolysis of nickel nitrate and subsequent calcination on NiO dispersion.

Conclusions

The phase evolution of supported cobalt and nickel nitrate precursors during thermal treatment in 10% v/v O_2/N_2, N_2 and 1 or 10% v/v NO/He flow was investigated with *in situ* diffuse reflectance FTIR (DRIFT) spectroscopy and XRD, and related to the dispersion. Both XRD and DRIFTS showed that thermal treatment of the supported nickel and cobalt nitrates in the presence of nitric oxide resulted in rapid and virtually complete decomposition to anhydrous nickel and cobalt hydroxynitrates of the form $M_x(OH)_y(NO_3)_z$, while hydrolysis in N_2 or O_2/N_2 was slow and incomplete. Furthermore, based on the DRIFT spectra it is postulated that at least part of the species formed in the presence of N_2 or O_2 were hydrated hydroxynitrates of the form $M_x(OH)_y(NO_3)_z \cdot aH_2O$. Removal of the metal $M_x(NO_3)_y \cdot aH_2O$ and $M_x(OH)_y(NO_3)_z \cdot aH_2O$ species via dissolution showed that nickel hydroxynitrates of the form $Ni_x(OH)_y(NO_3)_z$, formed during NO thermal treatment, displayed a severely reduced mobility as compared to the other species.

Thus we have shown that a key to the high NiO and Co_3O_4 dispersions from nitrate precursors is the immobilization by means of hydrolysis to cobalt and nickel hydroxynitrates at relatively low temperatures.

Acknowledgments

The authors kindly thank Marjan Versluijs-Helder for the *in situ* XRD measurements, Fouad Soulimani for his assistance with the DRIFT measurements, and David Maclachlan for the XRF analysis. Johnson Matthey Catalysts is acknowledged for the financial support and, especially Dr. Steve Pollington and Dr. John Casci, for their scientific contributions.

References

1. Balakos, M. W.; Hernandez, E. E. *Catal. Today* **1997**, *35*, 415.
2. *Catalyst Preparation: Science and Engineering*; Regalbuto, J. R., Ed.; Taylor & Francis, CRC Press: Boca Raton, 2007.
3. *Synthesis of Solid Catalysts*; de Jong, K. P., Ed.; Wiley-VCH Verlag GmbH & Co.: Weinheim, 2009.
4. Miller, J. T.; Schreier, M.; Kropf, A. J.; Regalbuto, J. R. *J. Catal.* **2004**, *225*, 203.
5. Schreier, M.; Regalbuto, J. R. *J. Catal.* **2004**, *225*, 190.
6. Negrier, F.; Marceau, E.; Che, M.; Giraudon, J. *J. Phys. Chem. B* **2005**, *109*, 2836.
7. Sun, K. Q.; Marceau, E.; Che, M. *Phys. Chem. Chem. Phys.* **2006**, *8*, 1731.
8. Dumond, F.; Marceau, E.; Che, M. *J. Phys. Chem. C* **2007**, *111*, 4780.
9. Marceau, E.; Che, M.; Čejka, J.; Zukal, A. *ChemCatChem* **2010**, *2*, 413.
10. Burattin, P.; Che, M.; Louis, C. *J. Phys. Chem. B* **1999**, *103*, 6171.
11. Chouillet, C.; Villain, F.; Kermarec, M.; Lauron-Pernot, H.; Louis, C. *J. Phys. Chem. B* **2003**, *107*, 3565.
12. Louis, C.; Xing Cheng, Z.; Che, M. *J. Phys. Chem.* **1993**, *97*, 5703.
13. Toupance, T.; Kermarec, M.; Louis, C. *J. Phys. Chem. B* **2000**, *104*, 965.
14. Borg, Ø.; Blekkan, E. A.; Eri, S.; Akporiaye, D.; Vigerust, B.; Rytter, E.; Holmen, A. *Top. Catal.* **2007**, *45*, 39.
15. Borg, Ø.; Eri, S.; Blekkan, E. A.; Storsæter, S.; Wigum, H.; Rytter, E.; Holmen, A. *J. Catal.* **2007**, *248*, 89.
16. Borg, Ø.; Dietzel, P. D. C.; Spjelkavik, A. I.; Tveten, E. Z.; Walmsley, J. C.; Diplas, S.; Eri, S.; Holmen, A.; Rytter, E. *J. Catal.* **2008**, *259*, 161.
17. van der Meer, J.; Bardez, I.; Bart, F.; Albouy, P. A.; Wallez, G.; Davidson, A. *Micropor. Mesopor. Mat.* **2009**, *118*, 183.
18. Chu, W.; Wang, L.; Chernavskii, P.; Khodakov, A. Y. *Angew. Chem. Int. Ed.* **2008**, *47*, 5052.
19. Sietsma, J. R. A.; Meeldijk, J. D.; Versluijs-Helder, M.; Broersma, A.; van Dillen, A. J.; de Jongh, P. E.; de Jong, K. P. *Chem. Mater.* **2008**, *20*, 2921.
20. Lensveld, D. J.; Mesu, J. G.; Van Dillen, A. J.; De Jong, K. P. *Micropor. Mesopor. Mat.* **2001**, *401*, 44.
21. van de Loosdrecht, J.; Barradas, S.; Caricato, E. A.; Ngwenya, N. G.; Nkwanyana, P. S.; Rawat, M. A. S.; Sigwebela, B. H.; van Berge, P. J.; Visagie, J. L. *Top. Catal.* **2003**, *26*, 121.
22. Negrier, F.; Marceau, E.; Che, M. *Chem. Commun.* **2002**, 1194.
23. Infantes-Molina, A.; Mérida-Robles, J.; Braos-García, P.; Rodríguez-Castellón, E.; Finocchio, E.; Busca, G.; Maireles-Torres, P.; Jiménez-López, A. *J. Catal.*

2004, *225*, 479.
24. Catillon-Mucherie, S.; Ammari, F.; Krafft, J. M.; Lauron-Pernot, H.; Touroude, R.; Louis, C. *J. Phys. Chem. C* **2007**, *111*, 11619.
25. Marceau, E.; Löfberg, A.; Giraudon, J.-M.; Négrier, F.; Che, M.; Leclercq, L. *Appl. Catal. A: Gen.* **2009**, *362*, 34.
26. Bartholomew, C. H.; Farrauto, R. J. *J. Catal.* **1976**, *45*, 41.
27. Sietsma, J. R. A.; Meeldijk, J. D.; Versluijs-Helder, M.; Broersma, A.; van Dillen, A. J.; de Jongh, P. E.; de Jong, K. P. *Chem. Mater.* **2008**, *20*, 2921.
28. Sietsma, J. R. A.; Meeldijk, J. D.; den Breejen, J. P.; Versluijs-Helder, M.; van Dillen, A. J.; de Jongh, P. E.; de Jong, K. P. *Angew. Chem. Int. Ed.* **2007**, *46*, 4547
29. Sietsma, J. R. A.; Friedrich, H.; Broersma, A.; Versluijs-Helder, M.; Jos van Dillen, A.; de Jongh, P. E.; de Jong, K. P. *J. Catal.* **2008**, *260*, 227.
30. Schröder, D.; de Jong, K. P.; Roithová, J. *Eur. J. Inorg. Chem.* **2009**, 2121.
31. Wolters, M.; Daly, H.; Goguet, A.; Meunier, F. C.; Hardacre, C.; Bitter, J. H.; de Jongh, P. E.; de Jong, K. P. *J. Phys. Chem. C* **2010**, *114*, 7839.
32. Zhao, D.; Feng, J.; Huo, Q.; Melosh, N.; Fredrickson, G. H.; Chmelka, B. F.; Stucky, G. D. *Science* **1998**, *279*, 548.
33. Jaroniec, M.; Kruk, M.; Olivier, J. P.; Koch, S. *Characterization of Porous Solids V* **2000**, *128*, 71.
34. Gallezot, P.; Prettre, M. *Bull. Soc. Chim. Fr.* **1968**, *2*, 407.
35. Markov, L.; Ioncheva, R.; Marinov, M.; Ivanov, K. *Mater. Chem. Phys.* **1990**, *26*, 493.
36. Petrov, K.; Zotov, N.; Mirtcheva, E.; Garciamartinez, O.; Rojas, R. M. *J. Mater. Chem.* **1994**, *4*, 611.
37. Louer, D. *J. Solid State Chem.* **1975**, *13*, 319.
38. Louër, M.; Louër, D.; Grandjean, D.; Weigel, D. *Acta Cryst.* **1973**, *B29*, 1707.
39. Markov, L.; Petrov, K.; Petkov, V. *Thermochim. Acta* **1986**, *106*, 283.
40. Petrov, K.; Zotov, N.; Garcia-Martinez, O.; Rojas, R. M. *J. Solid State Chem.* **1992**, *101*, 145.
41. Dickinson, C.; Zhou, W.; Hodgkins, R. P.; Shi, Y.; Zhao, D.; He, H. *Chem. Mater.* **2006**, *18*, 3088.
42. Rajamathi, M.; Kamath, P. V. *Int. J. Inorg. Mater.* **2001**, *3*, 901.
43. Addison, C. C.; Gatehouse, B. M. *J. Chem. Soc.*. **1960**, 613.
44. Vratny, F. *App. Chem.* **1959**, *13*, 59.
45. Ramesh, T. N.; Kamath, P. V. *J. Power Sources* **2006**, *156*, 655.
46. Nakamoto, K.; Margoshes, M.; Rundle, R. E. *J. Am. Chem. Soc.* **1955**, *77*, 6480.
47. Le Bjhan, S.; Figlarz, M. *Thermochim. Acta* **1973**, *6*, 319.
48. Oliva, P.; Leonardi, J.; Laurent, J. F.; Delmas, C.; Braconnier, J. J.; Figlarz, M.;

Fievet, F.; de Guibert, A. *J. Power Sources* **1982**, *8*, 229.
49. Brockner, W.; Ehrhardt, C.; Gjikaj, M. *Thermochim. Acta* **2007**, *456*, 64.
50. Maneva, M.; Petroff, N.; Pankova, M. *J. Therm. Anal.* **1990**, *36*, 577.
51. Chouillet, C.; Krafft, J.; Louis, C.; Lauron-Pernot, H. *Spectrochim. Acta Part A* **2004**, *60*, 505.
52. Cao, Y.; Choi, J.-H.; Haas, B.-M.; Johnson, M. S.; Okumura, M. *J. Chem. Phys.* **1993**, *99*, 9307.
53. Miller, Y.; Chaban, G. M.; Gerber, R. B. *J. Chem. Phys.* **2005**, *313*, 213.
54. Ehrhardt, C.; Gjikaj, M.; Brockner, W. *Thermochim. Acta* **2005**, *432*, 36.
55. Mu, J.; Perlmutter, D. D. *Thermochim. Acta* **1982**, *56*, 253.
56. Zotov, N.; Petrov, K.; Dimitrova-Pankanova, M. *J. Phys. Chem. Solids* **1990**, *51*, 1199.
57. Feitknecht, W.; Kummer, A. *Z. Anorg. Allg. Chemie* **1955**, *282*, 41.
58. Petrov, K.; Zotov, N.; Mirtcheva, E.; Garciamartinez, O.; Rojas, R. M. *J. Mater. Chem.* **1994**, *4*, 611.
59. Llewellyn, P. L.; Chevrota, V.; J. Ragaib; Cerclier, O.; Estienne, J.; Rouquerol, F. *Solid State lonics* **1997**, *101-103* 1293.
60. Estelle, J.; Salagre, P.; Cesteros, Y.; Serra, M.; Medina, F.; Sueiras, J. E. *Solid State Ionics* **2003**, *156*, 233.

Chapter 4

NO-Moderated Decomposition of Silica-Supported Nickel Nitrate

Abstract: The mechanism by which NO prevents agglomeration at high temperature (120-350 °C) was investigated by using combined in situ diffuse reflectance infrared Fourier transform (DRIFT) spectroscopy and mass spectrometry (MS). After impregnation and drying at 120 °C, a supported nickel hydroxynitrate phase with composition $Ni_3(NO_3)_2(OH)_4$ had been formed. Comparison of the evolution of the decomposition gases during the thermal decomposition of $Ni_3(NO_3)_2(OH)_4$ in labelled and unlabeled NO and O_2 revealed that NO scavenges oxygen radicals, forming NO_2. The DRIFT spectra revealed that the surface speciation evolved differently in the presence of NO as compared with in O_2 or Ar. It is proposed that oxygen scavenging by NO depletes the $Ni_3(NO_3)_2(OH)_4$ phase of nitrate groups, creating nucleation sites for the formation of NiO, which leads to very small (4 nm) NiO particles and prevents agglomeration.

Adapted with permission from M. Wolters, H. Daly, A. Goguet, F. C. Meunier, C. Hardacre, J. H. Bitter, P. E. de Jongh, and K. P. de Jong, *DRIFTS/MS/Isotopic Labeling Study on the NO-Moderated Decomposition of a Silica-Supported Nickel Nitrate Catalyst Precursor*, J. Phys. Chem. C 114 (2010) 7839.

Introduction

Supported metal (oxide) catalysts are essential for the production of fuels and chemicals, as well as for the reduction of environmental pollution. Among these supported metal catalysts, nickel-based catalysts are most frequently used, as they are applied in many important industrial processes such as the hydrogenation of edible oils, steam reforming, and methanation.[1-2] In many catalytic reactions, the activity is proportional to the metal (oxide) surface area, thus high surface-to-volume ratios are beneficial.

Highly dispersed supported metals can be prepared by deposition of appropriate precursors from the vapour phase or liquid phase onto a support (e.g., SiO_2 or Al_2O_3).[3-5] Commonly, impregnation of a support material with aqueous solutions containing metal precursors is preferred, because of its simplicity and small waste streams. Organic precursors yield high dispersions; however, limited solubility often requires multiple impregnation steps to achieve the desired metal loading.[6] Inorganic precursors such as nitrates, sulphates, and chlorides generally have much higher solubility in water, which makes them more attractive to industry. Nitrate precursors, in contrast to sulphate and chloride precursors, are easily converted into oxides via so-called "calcination" in air and are, therefore, preferred. On the other hand, nitrate precursors have the major disadvantage that they often result in poorly dispersed metal oxide phases due to agglomeration during drying and thermal treatment.[6-7]

Different approaches to counter the agglomeration include the use of chelating and viscosity-increasing agents in the impregnation solution and the tuning of the drying conditions such as heating rate and temperature.[7-13] Other successful approaches are the direct reduction[14-16] and glow discharge plasma assisted decomposition metal nitrates.[17] Recently, we have reported a very effective and facile method for the prevention of agglomeration, i.e., the replacement of the traditional air calcination by a thermal treatment in 1% v/v NO/He, resulting for instance in high NiO and Co_3O_4 dispersions.[18-19] Samples obtained via this method showed a superior activity compared to samples prepared via air calcination or direct reduction.[20-21] Another advantage is that NO is already one of the nitrate decomposition constituents, and thus addition of NO during calcination will not bring about large changes in the catalyst manufacturing process that has already been equipped with exhaust gas cleanup facilities.

The increased dispersion in the presence of NO was attributed to the more moderate rate of decomposition.[22] On the basis of the evolved gas analysis and equilibrium calculations, it was proposed that NO scavenges oxygen radicals produced during decomposition. The proposed decomposition reactions in Ar and

NO atmosphere are given in Equations 1 and 2, respectively, where $Ni_3(NO_3)_2(OH)_4$ is the crystalline intermediate obtained after drying at 120 °C.[23-24]

$$Ni_3(NO_3)_2(OH)_4\ (s) \rightarrow 3\ NiO\ (s) + 2\ NO_2\ (g) + 2\ H_2O + \tfrac{1}{2}\ O_2 \quad (1)$$

$$Ni_3(NO_3)_2(OH)_4\ (s) + NO \rightarrow 3\ NiO\ (s) + 3\ NO_2\ (g) + 2\ H_2O \quad (2)$$

Control over the preparation conditions and understanding of the physicochemical processes involved are key to the development of more active catalysts and may ultimately allow tuning of the particle size distribution, which is relevant to many catalysts.[25-27] Although the effect of NO on the agglomeration is apparent and was shown to lead to a more moderated decomposition, the mechanism by which this occurs is not understood. In the present study, the decomposition of nickel nitrate in the presence of different labelled and unlabeled gases, such as Ar, NO, ^{15}NO, O_2, and $^{18}O_2$, was studied by combining in situ diffuse reflection infrared (DRIFT) spectroscopy and mass spectrometry (MS).[28] The gas evolution during decomposition was followed with MS and provided insight into the role of NO. Simultaneously the evolution of the supported nickel hydroxide nitrate phase was studied with DRIFTS, which revealed significant differences in the evolution of the metal nitrates phases in NO and inert/air atmosphere. On the basis of these results, we propose an explanation for the reduced agglomeration in the presence of NO.

Experimental

Catalyst Preparation

SBA-15 (BET surface area 600 $m^2\ g^{-1}$, pore volume 0.8 $cm^3\ g^{-1}$, pore diameter 9 ± 0.5 nm) was prepared according to a literature procedure.[29] Prior to impregnation, the SBA-15 support was dried at 80 °C in dynamic vacuum to remove water from the pores. Subsequently, the SBA-15 support was impregnated to incipient wetness with a 4.2M aqueous nickel nitrate ($Ni(NO_3)_2{\cdot}6H_2O$ (99%, Acros)) solution and dried at 120 °C in static air for 12 h (further denoted as SBA-D). Small quantities of the impregnate (100 mg) were calcined/heat treated in a plug-flow reactor at 350 °C with a ramp of 3 deg min^{-1} under a flow (100 ml min^{-1}) of either air, N_2, 1% v/v NO/Ar, 1% v/v N_2O/He, or 10% v/v H_2/Ar. The samples are denoted as SBA-C_{air}, SBA-C_{N2}, SBA-C_{NO}, SBA-C_{N2O}, and SBA-C_{H2}, respectively. To facilitate the handling SBA-C_{H2} was reoxidized via an air calcination treatment at 350 °C.

Bulk $Ni_3(NO_3)_2(OH)_4$ was prepared according to a method described by Gallezot.[23] Nickel nitrate hexahydrate from ($Ni(NO_3)_2{\cdot}6H_2O$ (99%, Acros)) was heated for 48 h at 160 °C in static air. $Ni_3(NO_3)_2(OH)_4$ was collected from the resulting

cake by washing extensively with demineralised water followed by a second drying step at 120 °C.

Characterization

Powder X-ray diffraction (XRD) patterns ranging from 10 to 80° 2θ were obtained at room temperature with a Bruker-AXS D8 Advance X-ray diffractometer setup using Co $K_{\alpha 1,2}$ radiation. The average $Ni_3(NO_3)_2(OH)_4$ and NiO crystallite size was calculated by using the Debye-Scherrer equation from the most intense lines at 14.9° and 50.8° 2θ, respectively. Scanning transmission electron microscopy images were obtained on a Tecnai 20 operating at 200 keV. High angle annular dark field (HAADF) images were typically taken at a camera length of 150 mm.

Diffuse reflectance FT-IR (DRIFTS) measurements were carried out *in situ* in a high-temperature cell (Spectra-Tech) fitted with ZnSe windows. The cell was modified to ensure plug flow conditions and a low dead volume as previously reported.[28] To avoid temperature gradients through the poorly heat-conducting sample, the ceramic crucible was filled with SiC. On top of the SiC a thin layer of SBA-15-D (5 mg) was placed. The sample was dried at 120 °C in a flow of Ar (20 ml min^{-1}) for 30 min followed by a thermal treatment by raising the temperature from 120 to 350 °C with a ramp of 3 deg min^{-1} in a 20 ml min^{-1} flow of gas. The following gas mixtures were used: Ar, 20% v/v O_2/Ar, 1% v/v NO/Ar, 20% v/v $^{18}O_2$/Ar, 1% v/v ^{15}NO/Ar, 1% v/v N_2O/He, and 10% v/v H_2/Ar. Spectra (50 scans, 4 cm^{-1} resolution) were recorded every 2 min. In parallel, evolved gas analysis was performed with a Hiden Analytical HPR20 quadrupole mass spectrometer (QMS), which was connected to the outlet of the DRIFT cell. The mass spectrometer was equipped with a capillary inlet system with bypass allowing fast response (i.e., 100 ms) for the sampling.

Results and Discussion

Influence of the gas atmosphere on the NiO dispersion.

According to XRD results, impregnation of SBA-15 with nickel nitrate followed by drying at 120 °C resulted in the formation of nickel hydroxide nitrate crystallites with composition $Ni_3(NO_3)_2(OH)_4$ and an average size of 9 nm (Table 1).[23-24,30] The close agreement between the SBA-15 pore size and the $Ni_3(NO_3)_2(OH)_4$ crystallite size suggests that the phase is confined by the pores. This was confirmed by TEM (data not shown), which is in agreement with previous work.[24]

Subsequent thermal treatment at 350 °C resulted in the decomposition of the $Ni_3(NO_3)_2(OH)_4$ phase into nickel oxide, or nickel metal in the case of H_2 thermal

treatment. The H_2 thermal treatment was followed by an oxidation step in air at 350 °C prior to the XRD measurements. The effect of different gases on the NiO crystallite size after thermal treatment was analyzed by the 50.8° 2θ line broadening. The results of the line broadening analysis are shown in Table 1.

Table 1. Phases and crystallite sizes as obtained from XRD

sample	**phase**	**size** (nm)
SBA-D	$Ni_3(NO_3)_2(OH)_4$	9
SBA-C_{air}	NiO	14
SBA-C_{N2}	NiO	12
SBA-C_{NO}	NiO	4
SBA-C_{H2}[a]	NiO	5
SBA-C_{N2O}	NiO	4

[a] thermal treatment followed by oxidation in air at 350°C.

In accordance with the literature, the largest average crystallite size (14 nm) is found for air and the smallest (4 nm) for NO and N_2O thermal treatment.[18] The slightly smaller crystallite size obtained in N_2 as compared to air is ascribed to the absence of O_2. Addition of O_2 will delay the decomposition as it will shift the equilibrium toward the nickel hydroxynitrate. The higher decomposition temperature will accelerate the decomposition and we propose that this leads to the lower dispersions. TEM revealed that the treatments in air and nitrogen led to the formation of plugs of NiO in the pores and large agglomerates of NiO (10-60 nm) on the external surface (Figure 1A). In contrast, NO, N_2O, and H_2 thermal treatment prevented agglomeration and redistribution to the external surface, resulting in much smaller NiO crystallites located inside the pores (Table 1, Figure 1B).

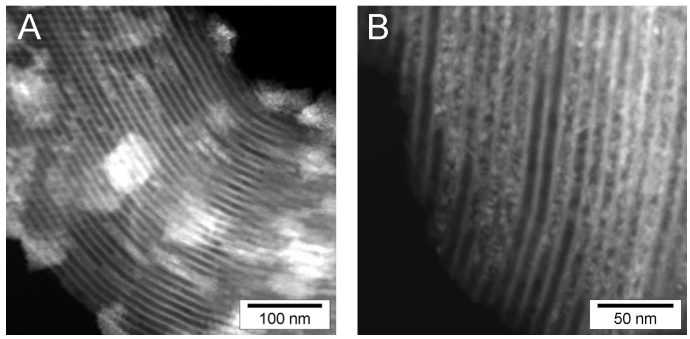

Figure 1. HAADF-STEM images of SBA-C_{N2} (A) and SBA-C_{NO} (B)

Assuming a one-to-one topotactic conversion of 9 nm $Ni_3(NO_3)_2(OH)_4$ crystallites into NiO, the expected final crystallite size can be calculated by taking into account the mass loss (40%) and density difference upon conversion from $Ni_3(NO_3)_2(OH)_4$ (~3.5 g cm^{-3}) into NiO (6.7 g cm^{-3}). The thus calculated average crystallite size is 6 nm, which is larger than the observed average NiO sizes after thermal decomposition in H_2 (5 nm) and N_2O and NO (4 nm). Fragmentation or anisotropy of the $Ni_3(NO_3)_2(OH)_4$ crystallites are possible explanations for the smaller NiO particle size. In the previous chapter it was determined that approximately 65% of the nickel nitrate phase is in the form of anhydrous nickel hydroxynitrates, the remaining 35% being amorphous hydrated nickel (hydroxy)nitrates. As only , $Ni_3(NO_3)_2(OH)_4$ is observed with XRD, the amorphous phases could have lowered the average NiO crystallite size.

Evolved Gas Analysis by MS.

The decomposition path of metal nitrates and the simultaneous evolution of NO_x and H_2O have been widely investigated.[31-37] The exact decomposition path and the composition of the evolved gases depend heavily on the experimental conditions and are still subject to discussion; therefore, it is only possible to write a global decomposition as in Equation 3:

$$Ni(NO_3)_2 \cdot 6\ H_2O \rightarrow NiO + (HNO_3, NO, NO_2, N_2O, O_2, H_2O) \quad (3)$$

Nitric acid formation is regularly observed as one of the decomposition constituents, as it is a product of the decomposition of metal nitrate hydrate into the intermediate metal hydroxide nitrate. In this study, decomposition into nickel hydroxide nitrate had already taken place to a large extent during the drying step in the catalyst preparation and, consequently, no HNO_3 formation was expected.

Previously, our group reported the absence of O_2 in the off-gas during decomposition in NO atmosphere, which was ascribed to oxygen scavenging by NO.[22] The hypothesis of oxygen scavenging was investigated in this study by comparing the gas evolution during decomposition in ^{15}NO, $^{18}O_2$, Ar, ^{14}NO, and $^{16}O_2$. Figure 2 shows the mass signals of the decomposition gases as a function of temperature for the NO and Ar thermal treatments. In accordance with the previous work, thermal treatment in Ar resulted in the evolution of H_2O (*m*/*z* 18), NO (*m*/*z* 30), O_2 (*m*/*z* 32), and NO_2 (*m*/*z* 46) around 300 °C.[15,32] A strong NO signal was observed, rather than the expected main product NO_2 (Equation 2). Fragmentation of NO_2 to NO and O in the spectrometer is a likely explanation for this observation. Similar fragmentation is expected during the NO thermal treatment, but was likely not observed due to

the high concentration of NO already present. Thermal treatment in oxygen yielded results similar to those in Ar and is, therefore, not shown herein. The slight delay of the H_2O evolution with respect to the other gases was observed with all treatments and is, therefore, ascribed to readsorption.

During NO thermal treatment O_2 was absent in the evolved gases. The absence of a peak in the NO evolution is due to the high background signal of NO in the feed gas. In addition, the NO_2 signal was much broader than that found under Ar and consisted of two maxima indicating a slower and possibly two-step decomposition. The presence of only one maximum in the water signal could indicate that only NO_2 is evolved in the first decomposition step, thereby showing that only nitrate groups are decomposed. As the complete decomposition of the nickel hydroxynitrate structure requires the condensation of the hydroxyl groups forming H_2O, this could indicate depletion of the structure of nitrate groups.

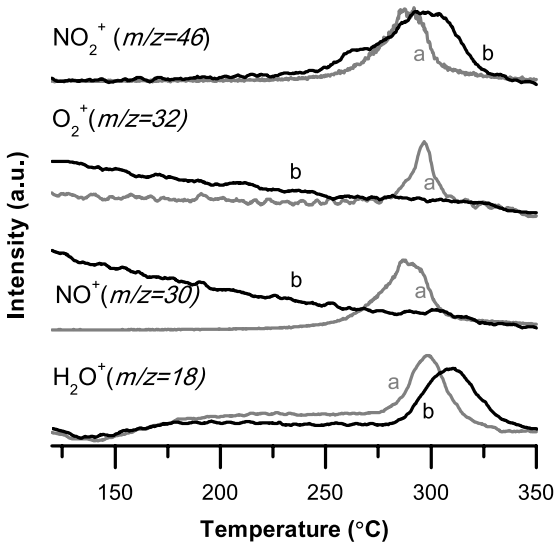

Figure 2. MS results obtained from the off gas during *in situ* thermal treatment of SBA-D in Ar (a) and 1% v/v NO/Ar (b)

Thermal treatment in ^{15}NO (Figure 3) exhibited an evolution pattern similar to that in ^{14}NO, yielding the expected unlabeled decomposition gases NO_2, NO, and H_2O, but not O_2. In addition to the unlabeled gases, a distinct peak with *m*/*z* 47 was observed in the 250-350 °C range, indicating the evolution of $^{15}NO_2$. As for the ^{14}NO experiment, two maxima appear in the $^{15}NO_2$ evolution, with the low temperature

maximum below the decomposition temperature in Ar or O_2/Ar. The concurrent ^{15}NO consumption confirms the proposed oxygen scavenging by NO takes place throughout the whole decomposition. The appearance of both $^{14}NO_2$ and $^{15}NO_2$ is in agreement with Equation 2, which predicts two-thirds of the evolved NO_2 molecules to be unlabeled, due to decomposition of the nitrates.

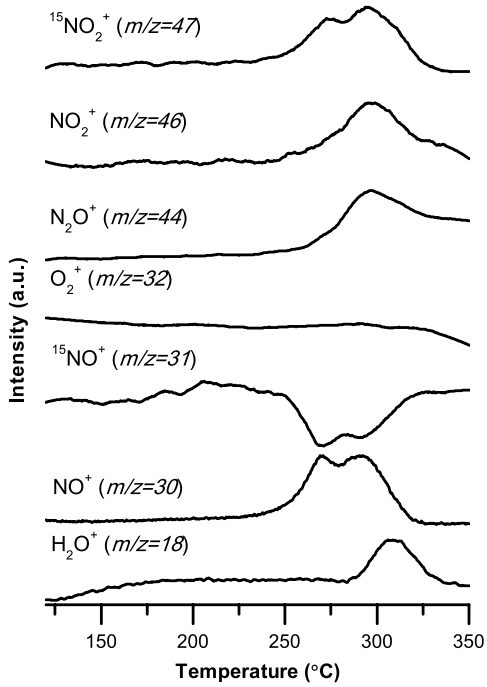

Figure 3. MS results obtained from the off gas during *in situ* thermal treatment of SBA-D in 1% v/v ^{15}NO/Ar.

Although ^{15}NO is unmistakably oxidized to $^{15}NO_2$ during the decomposition process, no conclusions can be drawn as yet regarding the reaction by which the oxidation takes place and its effect on the nitrate decomposition. In the next section the possible oxidation reactions will be considered. It is well-known that in the gas phase NO and O_2 may equilibrate with NO_2 (Equation 4). Thus, the addition of NO may push the equilibrium to the right, which might explain the lack of O_2 observed in the evolved gas. Equations 5 and 6 involve the reaction of adsorbed NO with the anions based on the strong oxidizing properties of nitrates. Finally, as proposed previously,[22] a surface reaction between nitric oxide and the oxygen radicals formed during nitrate decomposition (Equations 7 and 8) is proposed. This reaction is a

secondary reaction requiring no direct interaction between the nitrate and nitric oxide.

$$O_2(g) + 2\ NO(g) \leftrightarrow 2\ NO_2(g) \quad (4)$$
$$NO(ads) + NO_3^-(s) \rightarrow NO_2(g) + NO_2^-(s) \quad (5)$$
$$NO(ads) + 2\ NO_3^-(s) \rightarrow 3\ NO_2(g) + O^{2-}\ (as\ NiO) \quad (6)$$
$$Ni(NO_3)_2\ (s) \rightarrow NiO\ (s) + 2\ NO_2\ (g) + O\ (ads) \quad (7)$$
$$O\ (ads) + NO\ (ads) \rightarrow NO_2\ (g) \quad (8)$$

To verify equilibration of NO and O_2, according to Equation 4, a thermal treatment was performed in 20% v/v $^{18}O_2$/Ar (data not shown). No $N^{18}O_2$ or $NO^{18}O$ formation was observed, indicating the kinetics of reaction 4 are slow compared with the time scale of the measurement. Therefore, we conclude that the NO-NO_2 equilibrium is probably not the reason for the absence of O_2 in the off-gas during the NO treatment. Consequently, the oxidation has to be a surface reaction, which was further studied with DRIFT spectroscopy.

DRIFT spectroscopy.

DRIFT spectra of the SBA-D sample before and after NO treatment are shown in Figure 4. Before thermal treatment, the SBA-D sample exhibits intense peaks at 3606, 1555, and 1333 cm^{-1}, which were assigned to the symmetric OH stretch (ν_{OH}), antisymmetric NO_3^- stretch ($\nu_4(-ONO_2)$), and symmetric NO_3^- stretch ($\nu_1(-ONO_2)$) vibrations of $Ni_3(NO_3)_2(OH)_4$, respectively. After thermal treatment at 350 °C only intense silanol (Si-OH) vibration bands are visible at 3742 cm^{-1} and overtones of lattice vibrations of SiO_2 in the 1300-1000 cm^{-1} range.

An overview of all observed absorption bands and assignments according to literature is given in Table 2.[23,38] Decomposition of nitrate groups into nitrite groups according to Equation 5 would result in the appearance of strong vibration bands in the 1550-1050 cm^{-1} range,[39] which was not observed. However, this region partly overlaps with the Si-O-Si absorption region, possibly obscuring the bands. Thermal treatment of bulk nickel hydroxide nitrate under NO did confirm that nitrite formation does not take place to a significant extent during decomposition (data not shown). Moreover, literature studies involving NO_x adsorption on metal oxides almost never report nitrite formation, indicating its limited stability.[40] Therefore, it is less likely that NO reacts with NO_3^- to form NO_2 and NO_2^-.

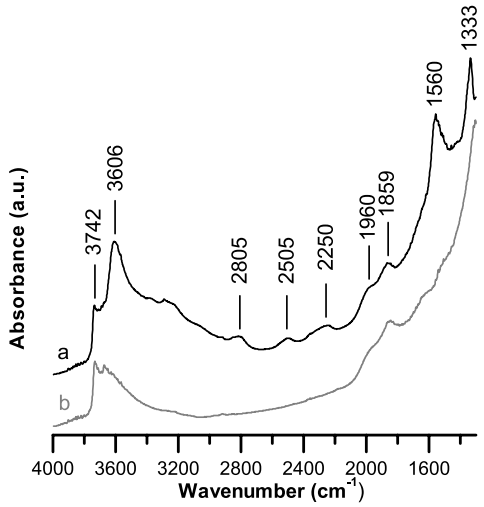

Figure 4. ***In situ*** **DRIFT spectra of the heat treatment of SBA-D taken after (a) pre-treatment in Ar at 120 °C (b) calcination in 1% v/v NO/Ar at 350 °C**

Table 2. Assignments of IR absorption bands

wavenumber (cm^{-1})		**assignment**
SBA-D	$Ni_2(OH)_3NO_3$[a]	
3742 s		ν_{OH} (SiOH)
3606 s	3625 s	ν_{OH} (NiOH)
2805 vw	2770 vw	$\nu_4 + \nu_1$
2506 vw	2490 vw	$\nu_4 + \nu_2$[b]
2250 w	2260 w	$\nu_1 + \nu_2$[b]
1960 vw		SiO_2 overtone
1859 vw		SiO_2 overtone
1560 s	1500 s	$\nu_4(-ONO_2)$
1300-1000 vs		Si-O-Si
1333 vs	1302 vs	$\nu_1(-ONO_2)$
-	1286 vs	

[a]Ref.[37]; [b]ν_2 NO stretch frequency of NO_3^- reported at 992 cm^{-1}. Abbreviations: vs, very strong; s, strong; w, weak; vw, very weak.

In both the ^{14}NO and ^{15}NO treatments no NO adsorption was observed over the whole temperature range. NO adsorption on NiO was observed after the thermal treatment had been completed, but only at temperatures below 100 °C. The absence of NO adsorption bands on supported or bulk $Ni_3(NO_3)_2(OH)_4$ suggests that adsorption on this phase is very weak. A number of reports have observed nitrate decomposition upon exposure to NO;[41-43] however, no evidence for a direct reaction between NO and nitrates was found. Therefore, it remains unclear whether the direct reaction of NO with $Ni_3(NO_3)_2(OH)_4$ (Equation 6) or the reaction of NO with surface oxygen species (Equations 7 and 8) is the most viable option to explain the moderated decomposition of transition metal nitrates.

Although no bands of adsorbed species appeared during the thermal treatments, there were distinct differences between the various thermal treatments. The two intense bands at 3606 and 1555 cm^{-1}, ascribed to the ν_{OH} and $\nu_4(\text{-}ONO_2)$ of $Ni_3(NO_3)_2(OH)_4$, evolved differently in NO compared with that found in Ar or O_2/Ar. Figure 5 shows the spectra of these vibrational regions during in situ NO and Ar thermal treatment. During thermal treatment the νOH and $\nu_4(\text{-}ONO_2)$ vibration frequencies shift depending on the gas atmosphere. To illustrate the trend in frequency, the peak maxima have been plotted as a function of temperature for NO, O_2/Ar, and Ar (Figure 6).

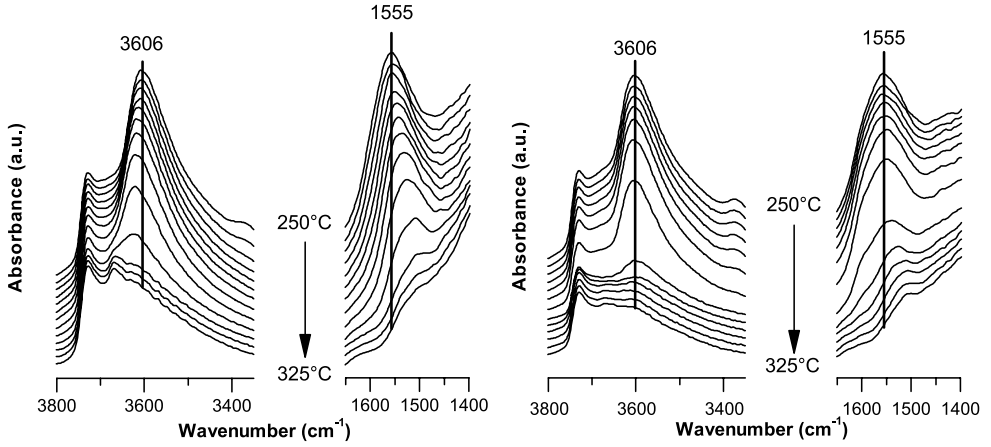

Figure 5. ***In situ*** **DRIFT spectra of the OH region and nitrate region during the calcination of SBA-D in 1% v/v NO/Ar (left) and Ar (right).**

Figure 6A depicts the peak maximum as a function of temperature for the ν_{OH} frequency of $Ni_3(NO_3)_2(OH)_4$ during the different treatments. A gradual blue shift is observed for the NO treatment, whereas no shift was found for the Ar and O_2 treatments. The impact of hydrogen bonding on the ν_{OH} frequency is well studied and clearly observed for turbostratic $Ni(OH)_2$, where removal of adsorbed or interlayer water during thermal treatment results in sharpening of the ν_{OH} band and a shift to higher frequencies.[44-46] However, no shift in the OH frequency is observed during the Ar and O_2/Ar thermal treatment, which excludes the influence of water removal on the observed shifts during NO treatment. As found with water, the nitrate groups in the structure may also influence the ν_{OH} frequency, and it is, therefore, expected that the ν_{OH} frequencies vary with the nitrate content of the structure. Indeed the ν_{OH} frequencies reported for different $Ni_x(NO_3)_y(OH)_z$ compositions vary between 3586 and 3630 cm^{-1},[23,38,47] and are in all cases significantly lower than the ν_{OH} frequency of-$Ni(OH)_2$ that is reported at 3650 cm^{-1}.[45] The gradual shift of the ν_{OH} frequency toward that of free hydroxyls in $Ni(OH)_2$ therefore suggests decomposition in NO results in the formation of "isolated" OH groups. This is in good agreement with the observed evolution of NO_2 prior to the evolution of water in the presence of NO (Figure 2).

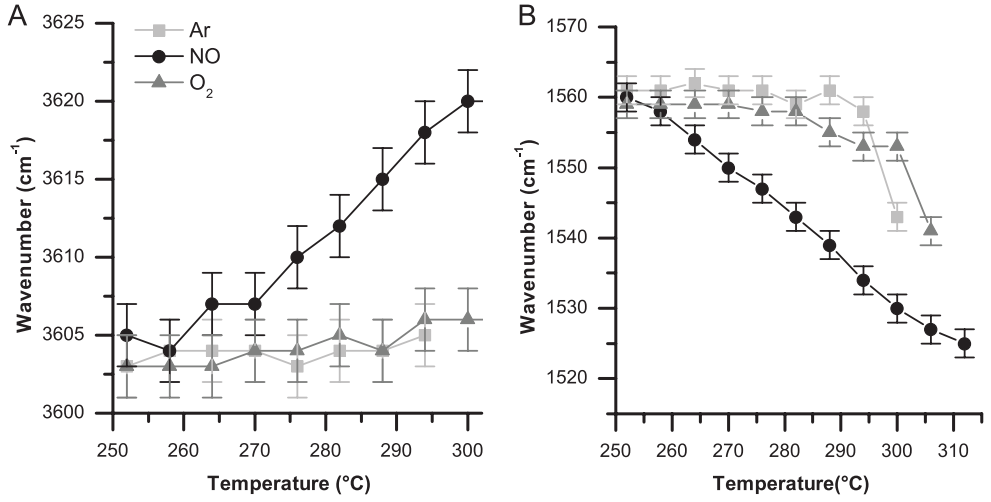

Figure 6. Peak maximum of the ν_{OH} band (A) and the $\nu_4(-ONO_2)$ band (B) as a function of temperature during the calcination of SBA-D in Ar (■), NO (●) and O_2 (▲).

Figure 6B shows a gradual red shift of the $\nu_4(-ONO_2)$ vibration frequency during the NO thermal treatment while a steep decline is observed for the other gases at much higher temperatures. Although definite quantitative information cannot be obtained, due to the absence of normalization possibilities, it is clear from the

intensity difference that the shift during treatment in Ar and O_2/Ar only occurs when most of the nitrate has decomposed. At this stage isolated nitrates adsorbed on NiO are predominant, which likely exhibit lower vibration frequencies. Although the ν_4(-ONO_2) frequency is influenced by adsorbed water, as observed during pre-treatment at 120 °C (not depicted), this cannot explain the observed shift during NO thermal treatment as otherwise it would have occurred during all treatments.

Further taking into account the high temperatures at which the shift was observed, it is not likely that it originates from the removal of adsorbed water. Therefore, the ν_4(-ONO_2) frequency shift during NO thermal treatment likely resulted from the gradual formation of isolated nitrate groups with a slightly different geometry (but likely still of the bidentate type). Although the exact nature of the isolated nitrate groups is not unambiguous, they are likely part of nickel nitrate fragments created by the collapse of the structure around the NiO nuclei and/or adsorbed nitrates on the NiO nuclei.

The spectra taken during N_2O and H_2 thermal treatment are given in Figure 7. In general, similar trends were observed as for NO, indicating a similar mechanism applies to other oxygen scavenging gases. It must be noted though that the shifts were not as gradual as for NO, which coincides with the higher effectiveness of NO to arrive at high NiO dispersions compared to the other molecules.

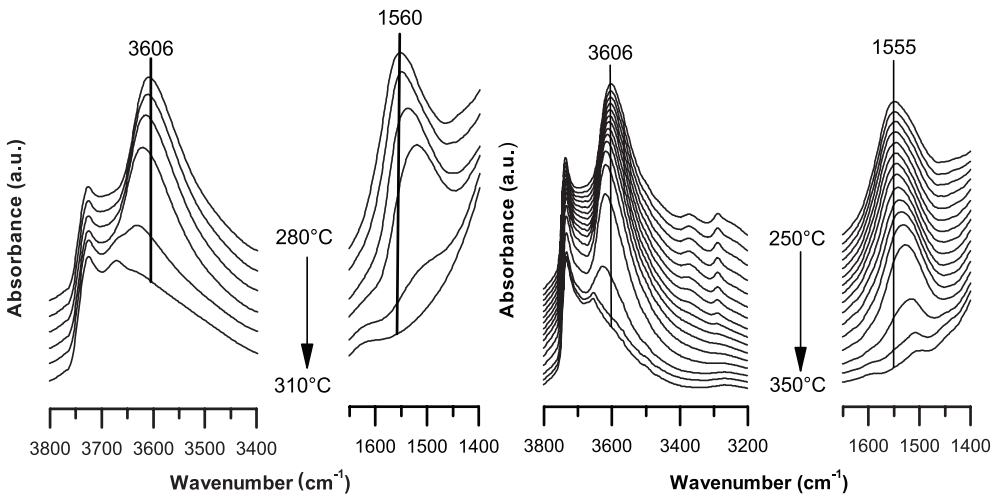

Figure 7. *In situ* DRIFT spectra of the OH region and nitrate region during the calcination of SBA-D in 10% v/v H_2/Ar (left) and 1% v/v N_2O/He (right).

Proposed mechanism by which NO affects the NiO dispersion.

Previously we have shown that the presence of NO affected the rate and temperature of decomposition of nickel hydroxynitrate. It was proposed that NO scavenges oxygen during decomposition, affecting several phase and reaction equilibria,[22] which was confirmed in this work by using labelled ^{15}NO. In addition, the gas evolution patterns suggested decomposition of the nitrate groups prior to condensation of the hydroxyl groups. The gradual blue and red shift of the ν_{OH} and $\nu_4(\text{-}ONO_2)$ frequencies, respectively, that was observed during NO thermal treatment, which have been ascribed to the formation of isolated OH and nitrate groups, is in good agreement with this proposal. On the basis of these observations an explanation for the high dispersion obtained in the presence of NO using the schematic representation in Figure 8 is proposed.

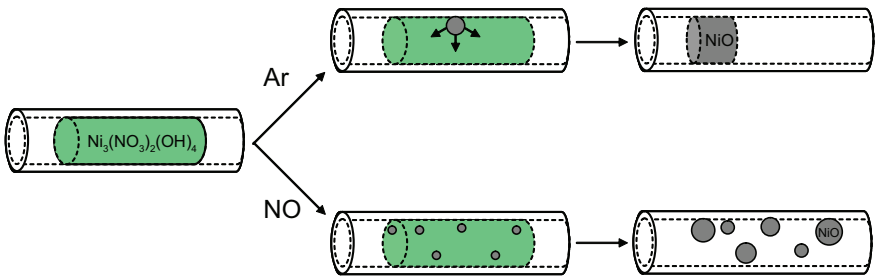

Figure 8. Schematic representation of the decomposition of $Ni_3(NO_3)_2(OH)_4$/SBA-15 in a flow of Ar or NO/Ar.

When during NO thermal treatment a nitrate group becomes unstable NO will react with the oxygen radical that is created, shifting the equilibrium toward NiO and creating a NiO nucleus (Figure 8). As the decomposition in NO starts at lower temperatures (vide supra), the rate of decomposition is still low, which combined with the high dispersion of the nickel hydroxynitrate ensures numerous NiO nuclei can be formed. The large number of NiO nuclei prevents extensive migration and sintering of the nickel hydroxynitrate and highly dispersed NiO particles are formed. However, in Ar, the oxygen radicals that are formed during the decomposition of a nitrate group will have to combine to form O_2 in order to complete the decomposition. If we assume this process is the rate-determining step and is catalyzed by NiO, as previously suggested,[22] the formation of a single NiO nucleus might trigger the decomposition of the nanorod of nickel hydroxynitrate (Figure 8). Due to the low number of nuclei and the higher decomposition temperature extensive migration and agglomeration leads to the observed relatively large NiO nanorods.

Conclusions

Highly dispersed supported NiO was obtained via thermal decomposition of a silica-supported nickel hydroxynitrate catalyst precursor in nitric oxide, whereas thermal treatment in air or inert atmosphere resulted in poor dispersions. The mechanism by which nitric oxide prevented agglomeration of the precursor during decomposition was investigated by using *in situ* DRIFT spectroscopy and mass spectrometry. A comparison of the gas evolution during thermal decomposition in ^{14}NO, ^{15}NO, $^{16}O_2$, $^{18}O_2$, and Ar revealed that NO scavenged oxygen species during decomposition. It was proposed that oxygen scavenging by NO resulted in the depletion of the nitrate groups of the precursor, thereby forming nucleation sites for NiO and immobilizing the nickel hydroxynitrate. DRIFTS spectra taken during the decomposition support this assignment, as, in the presence of NO not only is a decrease in the intensity of the ν_{OH} and $\nu_4(\text{-}ONO_2)$ precursor vibration bands observed, but also a simultaneous blue and red shift of their respective frequencies. Very similar observations for the decomposition in N_2O and H_2 indicated this research can be extended to a wide range of gases able to scavenge oxygen. Thus this research provided valuable insight into the mechanism by which metal nitrate agglomeration can be prevented, which is relevant to many catalysts.

Acknowledgments
The authors kindly thank Hans Meeldijk for the STEM analysis. Johnson Matthey Catalysts and the European Union (FP6 “Structuring the European Research Area” program) are acknowledged for the financial support.

References

1. Balakos, M. W.; Hernandez, E. E. *Catal. Today* **1997**, *35*, 415.
2. Chorkendorff, I.; Niemantsverdriet, H. *Concepts of Modern Catalysis and Kinetics*; 2 ed.; Wiley–VCH: Weinheim, 2007.
3. de Jong, K. P. *Curr. Opin. Solid State Mater. Sci.* **1999**, *4*, 55.
4. Bourikas, K.; Kordulis, C.; Lycourghiotis, A. *Catal. Rev. Sci. Eng.* **2006**, *48*, 363.
5. van der Lee, M. K.; Van Dillen, A. J.; Bitter, J. H.; de Jong, K. P. *J. Am. Chem. Soc.* **2005**, *127*, 13573.
6. van Dillen, A. J.; Terörde, R. J. A. M.; Lensveld, D. J.; Geus, J. W.; de Jong, K. P. *J. Catal.* **2003**, *216*, 257.
7. van de Loosdrecht, J.; Barradas, S.; Caricato, E. A.; Ngwenya, N. G.; Nkwanyana, P. S.; Rawat, M. A. S.; Sigwebela, B. H.; van Berge, P. J.; Visagie, J. L. *Top. Catal.* **2003**, *26*, 121.
8. Lensveld, D. J.; Mesu, J. G.; Van Dillen, A. J.; De Jong, K. P. *Micropor. Mesopor. Mat.* **2001**, *401*, 44.
9. Negrier, F.; Marceau, E.; Che, M. *Chem. Commun.* **2002**, 1194.
10. Chouillet, C.; Villain, F.; Kermarec, M.; Lauron-Pernot, H.; Louis, C. *J. Phys. Chem. B* **2003**, *107*, 3565.
11. Infantes-Molina, A.; Mérida-Robles, J.; Braos-García, P.; Rodríguez-Castellón, E.; Finocchio, E.; Busca, G.; Maireles-Torres, P.; Jiménez-López, A. *J. Catal.* **2004**, *225*, 479.
12. Catillon-Mucherie, S.; Ammari, F.; Krafft, J. M.; Lauron-Pernot, H.; Touroude, R.; Louis, C. *J. Phys. Chem. C* **2007**, *111*, 11619.
13. Marceau, E.; Löfberg, A.; Giraudon, J.-M.; Négrier, F.; Che, M.; Leclercq, L. *Appl. Catal. A: Gen.* **2009**, *362*, 34.
14. Bartholomew, C. H.; Farrauto, R. J. *J. Catal.* **1976**, *45*, 41.
15. Sietsma, J. R. A.; Meeldijk, J. D.; Versluijs-Helder, M.; Broersma, A.; van Dillen, A. J.; de Jongh, P. E.; de Jong, K. P. *Chem. Mater.* **2008**, *20*, 2921.
16. Louis, C.; Xing Cheng, Z.; Che, M. *J. Phys. Chem.* **1993**, *97*, 5703.
17. Chu, W.; Wang, L.; Chernavskii, P.; Khodakov, A. Y. *Angew. Chem. Int. Ed.* **2008**, *47*, 5052
18. Sietsma, J. R. A.; Meeldijk, J. D.; den Breejen, J. P.; Versluijs-Helder, M.; van Dillen, A. J.; de Jongh, P. E.; de Jong, K. P. *Angew. Chem. Int. Ed.* **2007**, *46*, 4547
19. Sietsma, J. R. A.; Van Dillen, A. J.; de Jongh, P. E.; De Jong, K. P., WO2007/071899, **2005**.
20. den Breejen, J. P.; Sietsma, J. R. A.; Friedrich, H.; Bitter, J. H.; de Jong, K. P. *Journal of Catalysis* **2010**, *270*, 146.
21. Sietsma, J. R. A. PhD thesis, Utrecht University, 2007.

22. Sietsma, J. R. A.; Friedrich, H.; Broersma, A.; Versluijs-Helder, M.; Jos van Dillen, A.; de Jongh, P. E.; de Jong, K. P. *J. Catal.* **2008**, *260*, 227.
23. Gallezot, P.; Prettre, M. *Bull. Soc. Chim. Fr.* **1968**, *2*, 407.
24. Sietsma, J. R. A.; van Dillen, A. J.; de Jongh, P. E.; de Jong, K. P. *Stud. Surf. Sci. Catal.* **2006**, *162*, 95.
25. Che, M.; Bennett, C. O. *Adv. Catal.* **1989**, *36*, 55.
26. Bezemer, G. L.; Bitter, J. H.; Kuipers, H.; Oosterbeek, H.; Holewijn, J. E.; Xu, X. D.; Kapteijn, F.; van Dillen, A. J.; de Jong, K. P. *J. Am. Chem. Soc.* **2006**, *128*, 3956.
27. van Santen, R. A. *Acc. Chem. Res.* **2009**, *42*, 57.
28. Goguet, A.; Meunier, F. C.; Tibiletti, D.; Breen, J. P.; Burch, R. *J. Phys. Chem. B* **2004**, *108*, 20240.
29. Zhao, D.; Feng, J.; Huo, Q.; Melosh, N.; Fredrickson, G. H.; Chmelka, B. F.; Stucky, G. D. *Science* **1998**, *279*, 548.
30. Estelle, J.; Salagre, P.; Cesteros, Y.; Serra, M.; Medina, F.; Sueiras, J. E. *Solid State Ionics* **2003**, *156*, 233.
31. Keely, W. M.; Maynor, W. *Chem. Eng. Data* **1963**, *8*.
32. Jackson, J. G.; Fonseca, R. W.; Holcombe, J. A. *Spectrochim. Acta Part B* **1995**, *50*, 1449.
33. Elmasry, M. A. A.; Gaber, A.; Khater, E. M. H. *J. Therm. Anal. Calorim.* **1998**, *52*, 489.
34. Zivkovic, Z. D.; Zivkovic, D. T.; Grujicic, D. B. *J. Therm. Anal. Calorim.* **1998**, *53*, 617.
35. Malecki, A.; Gajerski, R.; labus, S.; Prochowska-Klisch, B.; Wojciechowski, K. T. *J. Therm. Anal.* **2000**, *60*, 17.
36. Yuvaraj, S.; Fan-Yuan, L.; Tsong-Huei, C.; Chuin-Tih, Y. *J. Phys. Chem. B* **2003**, *107*, 1044.
37. Brockner, W.; Ehrhardt, C.; Gjikaj, M. *Thermochim. Acta* **2007**, *456*, 64.
38. Petrov, K.; Zotov, N.; Mirtcheva, E.; Garciamartinez, O.; Rojas, R. M. *J. Mater. Chem.* **1994**, *4*, 611.
39. Nakamoto, K. *Infrared and Raman Spectra of Inorganic and Coordination Compounds*; Fifth ed.; Wiley: New York 1997.
40. Hadjiivanov, K. I. *Catal. Rev. Sci. Eng.* **2000**, *42*, 71.
41. Djonev, B.; Tsyntsarski, B.; Klissurski, D.; Hadjiivanov, K. *J. Chem. Soc. Faraday Trans.* **1997**, *93*, 4055.
42. Manchot, W.; Waldmuller, A. *Ber. Deut. Chem. Ges.* **1926**, *59B*, 2363.
43. Venkov, T.; Hadjiivanov, K.; Milushev, A.; Klissurski, D. *Langmuir* **2003**, *19*, 3323.

44. Nakamoto, K.; Margoshes, M.; Rundle, R. E. *J. Am. Chem. Soc.* **1955**, *77*, 6480.
45. Le Bjhan, S.; Figlarz, M. *Thermochim. Acta* **1973**, *6*, 319.
46. Oliva, P.; Leonardi, J.; Laurent, J. F.; Delmas, C.; Braconnier, J. J.; Figlarz, M.; Fievet, F.; de Guibert, A. *J. Power Sources* **1982**, *8*, 229.
47. Biswick, T.; Jones, W.; Pacula, A.; Serwicka, E. *J. Solid State Chem.* **2006**, *179*, 49.

Chapter 5

Tuning the Nickel and Cobalt Oxide Particle Size

Abstract: Control over the size and size distribution of supported nanoparticles is a key to their efficient use in catalysis. In the preparation of nanoparticles by impregnation using nitrate precursors, the support pore diameter can be used to influence the average crystallite size. However, the particle size distributions obtained via this method are generally broad and the dispersions relatively low. Higher dispersions and narrow particle size distributions are obtained via thermal decomposition of the metal nitrate precursor in 1% (v/v) NO in Ar instead of air. In this chapter we will show that by combining the confinement effect of ordered mesoporous silica with a decomposition step of metal nitrates in NO, silica supported nickel and cobalt oxides with a tuneable particle size (2–4 nm) can be obtained at high loadings (10–20 wt%).

Adapted with permission from M. Wolters, L. J.W. van Grotel, T. M. Eggenhuisen, J. R. A. Sietsma, K. P. de Jong, P. E. de Jongh, *Combining confinement and NO calcination to arrive at highly dispersed supported nickel and cobalt oxide catalysts with a tuneable particle size*, Catal. Today, doi:10.1016/j.cattod.2010.02.052.

Introduction

Supported metal (oxide) catalysts are essential for the production of fuels and chemicals as well as the reduction of environmental pollution. Nickel and cobalt based catalysts are frequently used as they find application in industrial processes such as the hydrogenation of edible oils, steam reforming, methanation and the Fischer–Tropsch synthesis.[1-2] Recently, it has also been shown that small supported Co_3O_4 particles are efficient catalysts for the photo catalytic oxidation of water.[3] The activity and selectivity of catalyst nanoparticles strongly depend on their physical properties, such as size, distribution and shape.[4] Especially control over the size and size distribution is a key to the efficient use of metal (oxide) nanoparticles.[5-7] In most catalytic reactions, the activity is proportional to the metal (oxide) surface area, thus favouring high surface to volume ratios. However, non-continuous trends are observed for nanoparticles smaller than 10 nm. An example is the dependence of the Fischer–Tropsch synthesis activity on the cobalt particle size, where a sharp optimum in activity was found for 6 nm Co particles.[8-9]

Highly dispersed metals can be prepared by deposition from the vapour or liquid phase onto a support (e.g. SiO_2 or Al_2O_3).[10-12] In the industry, supported metal (oxides) are most often prepared by impregnation of a support material with aqueous solutions containing metal precursors. Organic precursors yield high dispersions, however, due to limited solubility multiple impregnation steps are often required to achieve the desired metal loading.[13] Inorganic precursors such as nitrates, sulphates and chlorides generally have much higher solubility in water, which allows high loadings in a single impregnation step. Nitrate precursors, in contrast to sulphate and chloride precursors, yield pure metal oxides after heat treatment and are therefore mostly used. On the other hand, nitrate precursors have the major disadvantage that they typically yield poor dispersions due to agglomeration during drying and thermal treatment (calcination).[13-14] Recently it was shown that replacement of the air calcination by a 1% v/v NO/He thermal treatment, prevents this agglomeration, resulting in highly dispersed supported cobalt and nickel oxides at high loadings.[15-16] The high dispersions were ascribed to the ability of NO to scavenge oxygen radicals which are produced during the decomposition of the nitrate, resulting in a moderated decomposition.[16]

Although yielding a very high dispersion, control over the particle size still remains a challenge. In literature the pore structure of the support has been used to confine the crystal growth. Cobalt clusters and nanoparticles with different diameters have been prepared from nitrate precursors by variation of the pore diameter of MCM-41,[17-18] albeit at loadings below 5 wt%. Li et al. used higher loadings (15 wt%

Co) for their studies on silica gel, SBA-15 and MCM-48, and confirmed that smaller pores resulted in a decrease in average particle diameter.[19] Similar observations were reported by Borg et al. on commercial alumina supports with varying pore diameters.[20] From these reports it is clear that confinement by the pores is a promising approach to tune the particle size of supported metal oxides prepared by impregnation. However, the average crystallite size was usually larger than the support pore diameter, and the particle size larger than the crystallite size, which may be expected considering the tendency of cobalt oxide to agglomerate.[20-22] In addition to the reduced metal surface area caused by agglomeration, reduced accessibility and stability of the active sites due to plugging of the pores may deteriorate the catalyst performance. In this chapter we have combined the use of ordered mesoporous supports with the moderated metal nitrate decomposition under NO to control the nickel and cobalt oxide particle size. We will show that this combination results in highly dispersed cobalt and nickel oxides with narrow particle size distributions. Furthermore, the average particle size can be tuned via the pore diameter of the support, and the crystallite size and particle size coincide.

Experimental

Sample preparation

SBA-15 was prepared according to literature.[23] Materials with different average pore diameters were obtained by aging at 80 °C (pore diameter (PD) = 9.7 nm), 60 °C (PD = 8.3) and 40 ◦C (PD = 6.7 nm). MCM-41 was synthesized according to the procedure reported by Cheng et al.[24] Materials with three different pore diameters were synthesized by variation of the template; $C_{13}H_{30}NBr$ (PD = 2.5 nm), $C_{19}H_{42}NBr$ (PD = 3.7 nm) and $C_{17}H_{38}NBr$ (PD = 4.6 nm). The aging temperature was 100 °C for the first two templates and 150 °C for the latter. After synthesis the support materials are coded as follows: support name followed by the pore diameter, e.g. SBA-9.6.

Nickel loaded samples were prepared by impregnating to incipient wetness with 4.2M aqueous nickel nitrate solution. After impregnation the sample was dried in stagnant air at 120 °C for 12 h. Calcination was performed at 350 ◦C in a flow of air or 1% v/v NO/Ar, using a heating rate of 5 °C/min and a dwell time of 2 h. Cobalt loaded samples were prepared similarly, by impregnating to incipient wetness with 3M aqueous cobalt nitrate solution. After impregnation the cobalt sample was dried at 60 °C for 12 h in stagnant air, and calcined at 240 °C in a flow of air or 1% v/v NO/Ar, using a heating rate of 1 °C/min and a dwell time of 2 h. The metal loading was 13–22 wt% depending on the specific pore volume of the support.

Impregnated samples are labelled by the addition of the metal type (e.g.

SBA-9.6-Ni) and heat treatment by addition of the gas atmosphere during calcination to the name (e.g. SBA-9.6-Ni-NO).

Characterization

Powder X-ray diffraction (XRD) patterns were obtained at room temperature from 10 to 80° 2θ with a Bruker-AXS D8 Advance X-ray Diffractometer setup using $CoK_{\alpha 1,2}$ radiation (λ = 0.179 nm). The average $Ni_3(NO_3)_2(OH)_4$, NiO and Co_3O_4 crystallite size was calculated from the most intense lines at 14.9° (0 0 1), 50.8° (2 0 0) and 43.1° (3 1 1) 2θ, respectively.

N_2-physisorption measurements were performed at −196 ◦C, using a Micromeretics Tristar 3000 apparatus. Prior to the measurement the samples were degassed in a flow of nitrogen at 300 ◦C for 12 h. Pore size distributions were derived from the adsorption branch of the isotherm, using non-local density functional theory (NL-DFT).[25] The mesopore surface area was determined with the t-method,[26] using the Harkins and Jura thickness equation,[27] by subtracting the slope of the t-plot in the 1.00–1.40 nm thickness range from the 0.35–0.55 nm range.

Scanning transmission electron microscopy (STEM) and transmission electron microscopy (TEM) images were obtained on a Tecnai 20 apparatus, operated at 200 keV. High angle annular dark field (HAADF) images were typically taken at a camera length of 150 mm. The average NiO particle size on the external surface was determined by counting a total of 150 NiO particles on 5 different support particles.

Results

Support characterization

MCM-41 and SBA-15 with different mesopore diameters were prepared by variation of the template and synthesis temperature. Characterization of these materials by N_2-physisorption (Figure 1) showed adsorption isotherms of the IV type, as expected for MCM-41 and SBA-15 materials. The textural properties derived from the measurements are given in Table 1. SBA-15, in contrast to MCM-41, shows a clear H1 type hysteresis loop and a high onset at low p/p_0 values originating from the intra wall micro porosity. The steep increase in adsorption at high p/p_0 values in the case of MCM-3.7 indicates the presence of macro pores which could have been caused by aggregation of the relatively small support particles, as observed with TEM (data not shown). The pore size distributions in Figure 1 show that all materials had uniform pore diameters, which ranged between 2.5 and 9.6 nm.

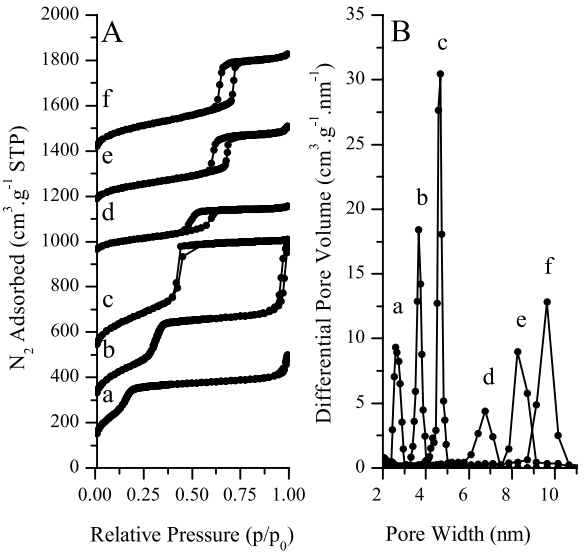

Figure 1. N_2-physisorption isotherms (A) and differential pore size distributions (B) of pristine (a) MCM-2.5, (b) MCM-3.7, (c) MCM-4.6, (d) SBA-6.7, (e) SBA-8.3 and (f) SBA-9.6.

Table 1. Overview N_2-physisorption results and unit cell sizes for the pristine supports

sample	d_{pore} [a] (nm)	a_o [b] (nm)	S_{meso} [c] ($m^2.g^{-1}$)	**porosity** ($cm^3.g^{-1}$)		
				V_{tot} [d]	V_{meso} [e]	V_{micro} [f]
MC-2.5	2.5	3.6	1188	0.65	0.60	0
MC-3.7	3.7	4.1	888	0.80	0.71	0
MC-4.6	4.6	5.3	914	0.94	0.92	0
SBA-6.7	6.7	8.8	264	0.38	0.37	0.05
SBA-8.3	8.3	10.3	338	0.59	0.57	0.05
SBA-9.6	9.6	11.0	450	0.79	0.77	0.08

[a]Pore diameter determined using NL-DFT. [b]Unit cell size determined from XRD ($a_o = 2 \times d(100)/\sqrt{3}$). [c]Mesopore surface area determined using t-method. [d]Total pore volume based on amount N_2 adsorbed at $P/P_0 = 0.95$. [e]Mesopore volume determined using NL-DFT. [f]Micropore volume determined using t-method.

The low-angle X-ray diffraction profiles of SBA-15 and MCM-41 showed reflections in the 2θ range of 1–8° (Figure 2) which could be indexed as the (1 0 0), (1 1 0) and (2 0 0) lattices of a unit cell with hexagonal symmetry.[23] The presence of higher order diffractions indicates uniformly ordered pore structures were obtained

in all cases, with the exception of MCM-2.5. The decreasing unit cell size going from SBA-9.6 to MCM-2.5 is evident from the shift of the diffractions to higher 2θ values, in agreement with the decreasing pore size (Table 1). The relatively larger shift in unit cell size between the SBA-6.7 and MCM-4.6 results from the thinner pore walls in MCM-41.[23]

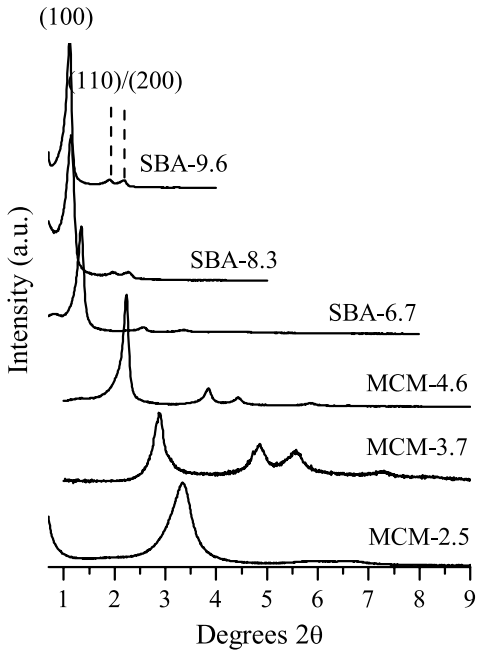

Figure 2. Low-angle XRD patterns of the pristine MCM-41 and SBA-15 samples.

Nickel oxide

First, the support materials were impregnated with an aqueous nickel nitrate solution, followed by drying at 120 °C. The resulting dried impregnate showed diffraction lines corresponding to a nickel hydroxynitrate phase with composition $Ni_3(NO_3)_2(OH)_4$.[28-29] $Ni_3(NO_3)_2(OH)_4$ belongs to the family of double layered hydroxides (DLHs) and has a hexagonal unit cell with parameters a = 3.13 Å and c = 6.89 Å. Formation of $Ni_3(NO_3)_2(OH)_4$ during heating of nickel nitrate hexahydrate at 100–210 ◦C has been reported previously and is proposed to occur via the following decomposition reaction.[29-32]

$$3[Ni(OH_2)_6](NO_3)_2(aq) \rightarrow Ni_3(NO_3)_2(OH)_4(s) + 4HNO_3(g) + 14H_2O(g) \quad (1)$$

Characterization of the samples after drying was facilitated by presence of the $Ni_3(NO_3)_2(OH)_4$ crystallites, which could be detected by XRD. The clear peak broadening of the diffraction lines (Figure 3) allowed calculation of the average crystallite size in the different samples. DLHs generally exhibit strong diffraction lines in the stacking direction, whereas the in-plane crystallization is generally poor. Consequently, only reliable calculations for the (0 0 1) diffraction line could be performed. In Fig. 4A the derived crystallite sizes are plotted as a function of the pore diameter. The clear one-to-one relation indicates that growth of the $Ni_3(NO_3)_2(OH)_4$ phase was confined by the pore walls. Indeed with TEM we observed no crystallites on the external surface of the material, indicating the phase was retained inside the pores during drying as we reported earlier.[29]

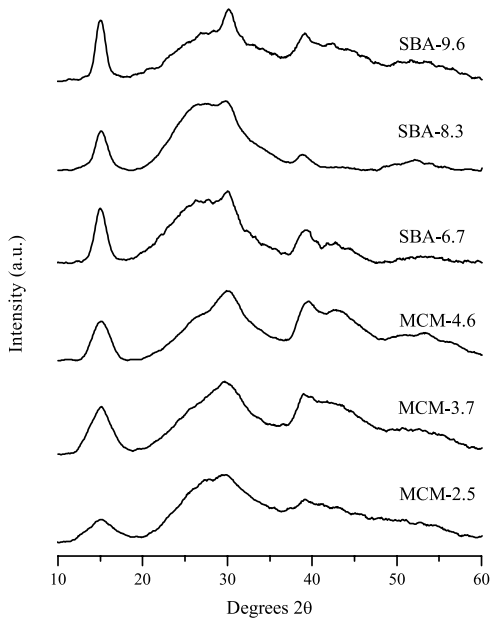

Figure 3. $Ni_3(NO_3)_2(OH)_4$ XRD patterns of the different samples after drying at 120°C

Upon thermal treatment at 350 °C the nickel hydroxynitrate phase is decomposed into nickel oxide. Topotactic conversion would result in a 30% shrinkage of the crystallite size, due to mass loss and density increase. However, the average NiO crystallite size after air thermal treatment was in all cases (with the exception of SBA-6.7-Ni) larger than the initial $Ni_3(NO_3)_2(OH)_4$ crystallite size (Figure 4B, curve ●). This indicated that not only agglomeration had taken place, but

also suggested that either transport to the external surface of the support particles had occurred, or that the pore structure had been destroyed by the crystallization process.

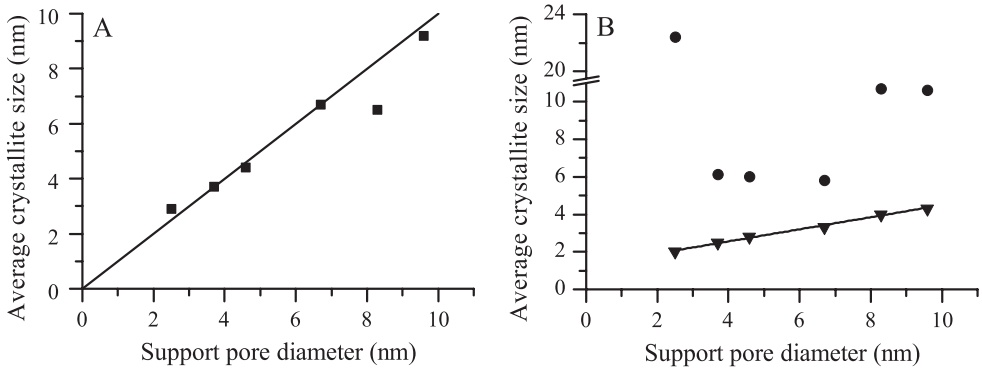

Figure 4. Relation between the support diameter and A) the average $Ni_3(NO_3)_2(OH)_4$ crystallite size obtained after impregnation and drying, B) the average NiO crystallite size obtained after NO (▼) and air calcination (●).

Combined evidence from low-angle XRD, N_2-physisorption and STEM indicated that the pore structure had been retained during calcination. Therefore, the large crystallite size can be ascribed to transport of the nickel nitrate phase to the external surface. Figures 5A and 6A show STEM images of SBA-9.6-Ni-air and SBA-4.6-Ni-air, which were representative for all samples. Part of the nickel oxide phase is retained inside the pores, exclusively forming rod like particles with a diameter equal to the pore diameter, further referred to as plugs. The remaining part is located on the external surface, forming 20–60 nm particles. However, with XRD no crystal domains of this size are detected, which suggests that the larger particles consist of multiple crystal domains. This is confirmed by the mesoporosity of the large NiO particles that is clearly observed in Fig. 6A.

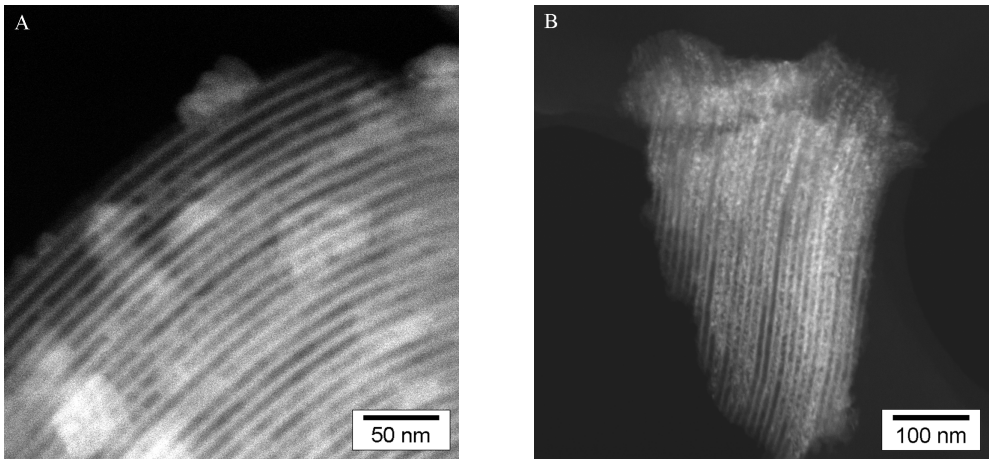

Figure 5. HAADF-STEM image of SBA-9.6-Ni after calcination in (A) air and (B) 1% NO/Ar.

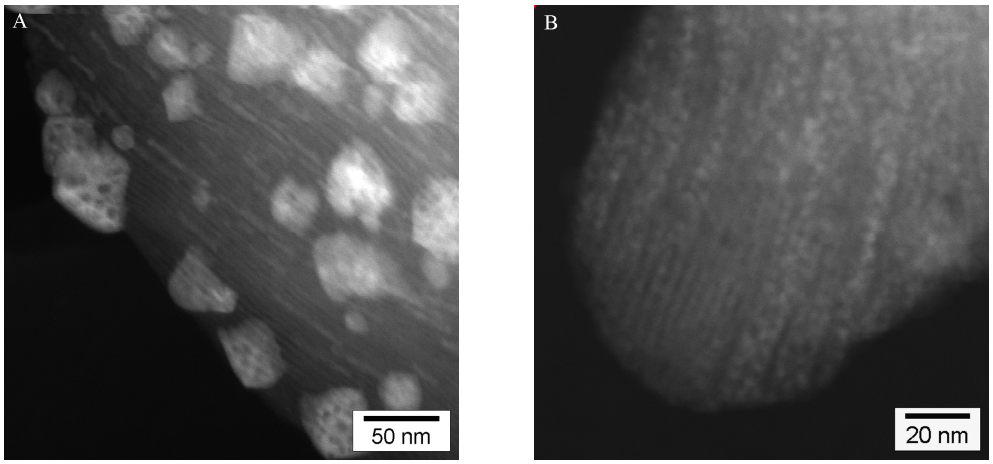

Figure 6. HAADF-STEM image of SBA-4.6-Ni after calcination in air (A) and 1% v/v NO/Ar (B)

The large average crystallite size derived for MCM-2.5-Ni-air is at first surprising. This cannot be attributed to larger particles on the external surface as the number average, determined from STEM, was around 25 nm for all three MCM-41 samples. The most likely explanation is that the crystal domains inside the smallest pores are so small that they cannot reliably be detected with XRD. For the somewhat larger pores of MCM-3.7, a clear bimodal distribution is observed in the XRD (Figure 7), where the sharp peak and the very broad feature can be ascribed to large crystals on the external surface and very small crystallites inside the pores. Therefore, the crystallites inside the even smaller MCM-2.5 pores are

likely undetectable. Consequently, the volume average in this sample will mostly be determined by the particles on the external surface.

Fig. 4B (curve ▼) shows that NO calcination in all cases yields much smaller crystallites than air calcination (diffraction patterns shown in Figure 7). STEM images of SBA- 9.6-Ni-NO and SBA-4.6-Ni-NO (Figures 5B and 6B) show that virtually all NiO particles are indeed located inside the pores and no plugs were formed. The retention of the phase in the pores, and the fact that the particle size is close to the crystallite size, explains the good correlation between the support pore diameter and the crystallite size shown in Figure 4. It must be noted that the average NiO crystallite size in the larger pore samples is significantly smaller than expected from topotactic conversion. This can be attributed to fragmentation of the $Ni_3(NO_3)_2(OH)_4$ particles upon decomposition. For the MCM-41 materials the crystallite size is closer to the value expected from topotactic conversion. The difference could be explained using a similar argument as for the air calcination, that the crystallites inside the smallest pores are not detected.

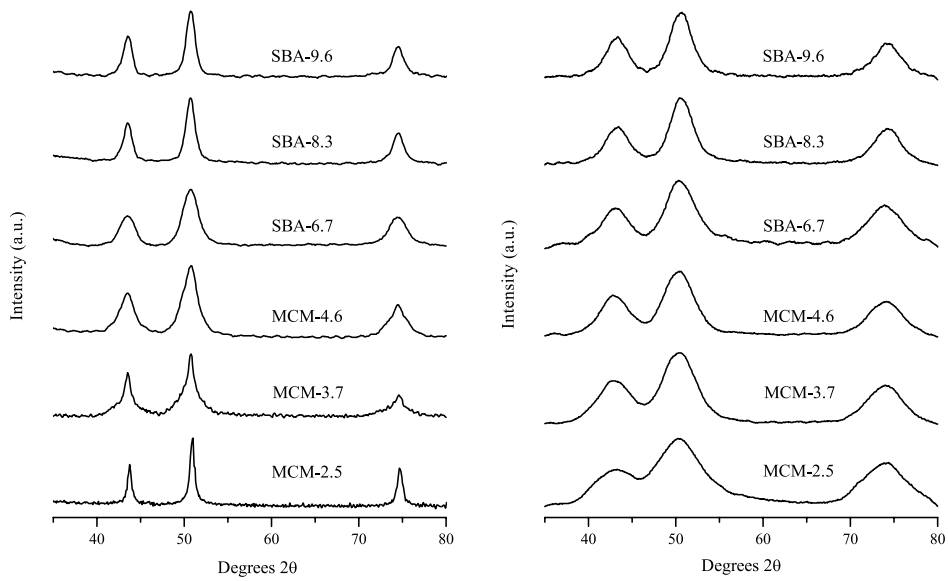

Figure 7. NiO XRD patterns of the different samples after air calcination (left) and NO calcination (right).

Cobalt oxide

To prevent decomposition of cobalt nitrate to Co_3O_4 prior to the calcination, the drying temperature was lowered to 60 °C. Consequently the dried samples did not exhibit any diffraction lines.

XRD after air and NO calcination of the different cobalt nitrate impregnated supports resulted in broad peaks corresponding to Co_3O_4. As for the nickel samples the peak broadening was used to calculate the average crystallite size, and plotted against the pore diameter (Figure 8). Here, also the air calcination (curve ●) of the cobalt samples yielded a clear relation between the average crystallite size and the pore diameter. However, the observed average crystallite size was still larger than the pore diameter. Closer investigation of MCM-4.6-Co-air and SBA-9.6-Co-air with TEM (Figures 9A and 10A) revealed that again two types of particles are present; large particles (6–20 nm) on the external surface and plugs inside the pores. In general less transport of metal oxide to the external surface is observed compared to nickel. Remarkably, for the SBA-15-Co samples the plugs appeared to be arranged into specific patches in the particle, whereas in the case of MCM-41 more isolated plugs were found. The difference between the two supports could originate from the difference in pore structure. SBA-15, unlike MCM-41, has microporous walls, and the apparent agglomeration suggests that transport of cobalt nitrate between adjacent pores has occurred. This phenomenon of clustering of Co_3O_4 crystallites has been observed before by others both with SBA-15 supports[3,21] and γ-Al_2O_3[20,22].

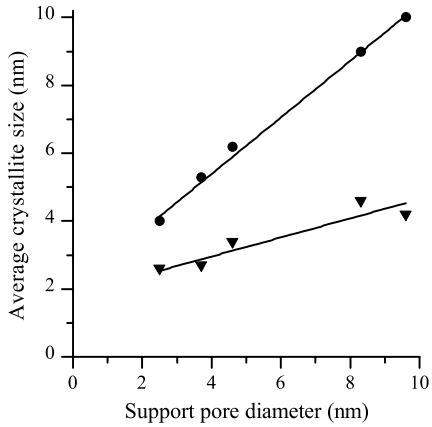

Figure 8. Relation between the support diameter and the average Co_3O_4 crystallite size obtained after NO (▼) and air calcination (●).

The transport of cobalt nitrate species is dependent on the gas atmosphere, as is apparent from the results after NO calcination. Figure 8, curve ▼ shows the average Co_3O_4 crystallite size after NO calcination as a function of the pore diameter. As for the nickel samples the size of the Co_3O_4 crystallites was related to the pore diameter, and were much smaller than for the air calcined samples. TEM images of MCM-4.6-Co-NO and SBA-9.6-Co-NO are depicted in Figures 9B and 10B, respectively. Samples calcined in NO show pores filled with small particles as well as empty pores (Figures 9B and 10B), which we previously ascribed to redistribution during drying rather than agglomeration during calcination.[29,33] However, cobalt oxide plugs and agglomeration to specific patches in the SBA-15 particles were no longer observed, indicating that an improved distribution over the support particle was obtained.

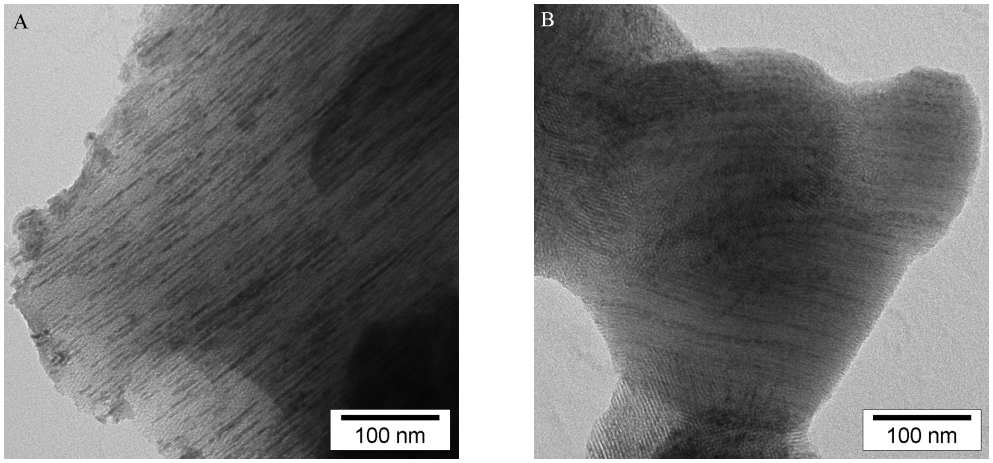

Figure 9. TEM image of MCM-4.6-Co after calcination in air (A) and 1% v/v NO/Ar (B).

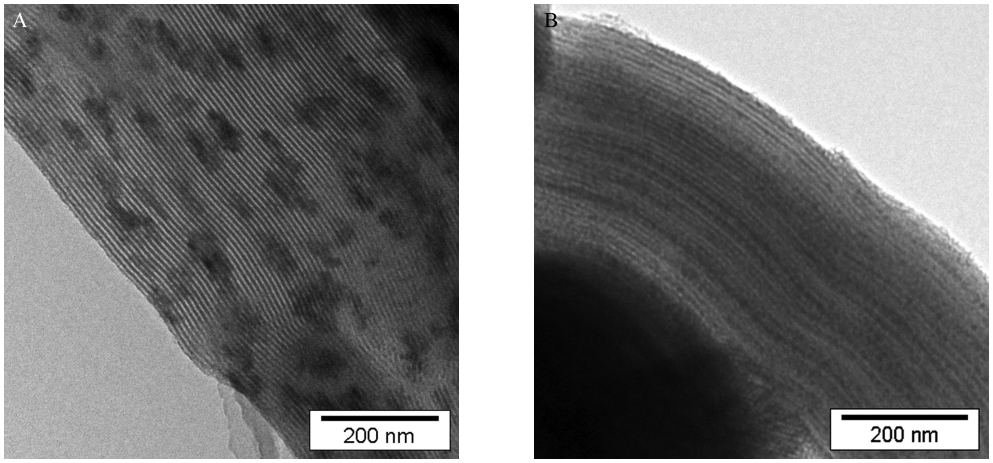

Figure 10. TEM image of SBA-9.6-Co after calcination in air (A) and 1% v/v NO/Ar (B).

Conclusions

We have shown that the average NiO and Co_3O_4 crystallite size can be tuned by variation of the support pore diameter. Essential to obtain highly dispersed particles with narrow particle size distributions from supported metal nitrates was the presence of NO during thermal decomposition of the precursor. Although the average Co_3O_4 and NiO crystallite sizes obtained by conventional thermal treatment in air were influenced by the pore size, particles typically consisted of agglomerates (2–60 nm) of crystallites that bear only a rather poor correlation to the pore diameter. NO calcination, on the other hand, yielded high metal oxide dispersions and narrow particle size distributions that were well in agreement with the average crystallite size. Control over the particle size and distribution over the support is an essential factor to the activity and stability of supported catalysts. In this contribution nickel and cobalt oxide on ordered mesoporous silica were investigated as a case study, but it is anticipated that similar results will be obtained for more conventional supports such as silica gel.

Acknowledgments

The authors kindly thank Hans Meeldijk and Cor van der Spek for the STEM and TEM analysis. Johnson Matthey Catalysts is acknowledged acknowledged for the financial support and, especially Steve Pollington and John Casci for their scientific contributions to this work.

References

1. Balakos, M. W.; Hernandez, E. E. *Catal. Today* **1997**, *35*, 415.
2. Chorkendorff, I.; Niemantsverdriet, H. *Concepts of Modern Catalysis and Kinetics*; 2 ed.; Wiley–VCH: Weinheim, 2007.
3. Jiao, F.; Frei, H. *Angew. Chem. Int. Ed.* **2009** *48*, 1841
4. Bell, A. T. *Science* **2003**, *299*, 1688.
5. Che, M.; Bennett, C. O. *Adv. Catal.* **1989**, *36*, 55.
6. Somorjai, G. A.; Park, J. Y. *Top. Catal.* **2008**, *49*, 126.
7. van Santen, R. A. *Acc. Chem. Res.* **2009**, *42*, 57.
8. Bezemer, G. L.; Bitter, J. H.; Kuipers, H.; Oosterbeek, H.; Holewijn, J. E.; Xu, X. D.; Kapteijn, F.; van Dillen, A. J.; de Jong, K. P. *J. Am. Chem. Soc.* **2006**, *128*, 3956.
9. den Breejen, J. P.; Radstake, P. B.; Bezemer, G. L.; Bitter, J. H.; Froseth, V.; Holmen, A.; de Jong, K. P. *J. Am. Chem. Soc.* **2009**, *131*, 7197.
10. de Jong, K. P. *Curr. Opin. Solid State Mater. Sci.* **1999**, *4*, 55.
11. Bourikas, K.; Kordulis, C.; Lycourghiotis, A. *Catal. Rev. Sci. Eng.* **2006**, *48*, 363.
12. van der Lee, M. K.; Van Dillen, A. J.; Bitter, J. H.; de Jong, K. P. *J. Am. Chem. Soc.* **2005**, *127*, 13573.
13. van Dillen, A. J.; Terörde, R. J. A. M.; Lensveld, D. J.; Geus, J. W.; de Jong, K. P. *J. Catal.* **2003**, *216*, 257.
14. van de Loosdrecht, J.; Barradas, S.; Caricato, E. A.; Ngwenya, N. G.; Nkwanyana, P. S.; Rawat, M. A. S.; Sigwebela, B. H.; van Berge, P. J.; Visagie, J. L. *Top. Catal.* **2003**, *26*, 121.
15. Sietsma, J. R. A.; Meeldijk, J. D.; den Breejen, J. P.; Versluijs-Helder, M.; van Dillen, A. J.; de Jongh, P. E.; de Jong, K. P. *Angew. Chem. Int. Ed.* **2007**, *46*, 4547
16. Sietsma, J. R. A.; Friedrich, H.; Broersma, A.; Versluijs-Helder, M.; Jos van Dillen, A.; de Jongh, P. E.; de Jong, K. P. *J. Catal.* **2008**, *260*, 227.
17. Khodakov, A. Y.; Griboval-Constant, A.; Bechara, R.; Villain, F. *J. Phys. Chem. B* **2001**, *105*, 9805.
18. Jentys, A.; Pham, N. H.; Vinek, H.; Englisch, M.; Lercher, J. A. *Catal. Today* **1998**, *39*, 311.
19. Li, H. L.; Li, J. L.; Ni, H. K.; Song, D. C. *Catal. Lett.* **2006**, *110*, 71.
20. Borg, O.; Walmsley, J. C.; Dehghan, R.; Tanem, B. S.; Blekkan, E. A.; Eri, S.; Rytter, E.; Holmen, A. *Catal. Lett.* **2008**, *126*, 224.
21. van der Meer, J.; Bardez, I.; Bart, F.; Albouy, P. A.; Wallez, G.; Davidson, A. *Micropor. Mesopor. Mat.* **2009**, *118*, 183.
22. Borg, Ø.; Dietzel, P. D. C.; Spjelkavik, A. I.; Tveten, E. Z.; Walmsley, J. C.; Diplas, S.; Eri, S.; Holmen, A.; Rytter, E. *J. Catal.* **2008**, *259*, 161.

23. Zhao, D.; Feng, J.; Huo, Q.; Melosh, N.; Fredrickson, G. H.; Chmelka, B. F.; Stucky, G. D. *Science* **1998**, *279*, 548.
24. Cheng, C.; Park, D. H.; Klinowski, J. *J. Chem. Soc. Faraday Trans.* **1997**, *93*, 193.
25. Jaroniec, M.; Kruk, M.; Olivier, J. P.; Koch, S. *Stud. Surf. Sci. Catal.* **2000**, *128*, 71.
26. Lippens, B. C.; de Boer, J. H. *J. Catal.* **1965**, *4*, 319.
27. Harkins, W. D.; Jura, G. *J. Am. Chem. Soc.* **1944**, *66*, 1366.
28. Gallezot, P.; Prettre, M. *Bull. Soc. Chim. Fr.* **1968**, *2*, 407.
29. Sietsma, J. R. A.; Meeldijk, J. D.; Versluijs-Helder, M.; Broersma, A.; van Dillen, A. J.; de Jongh, P. E.; de Jong, K. P. *Chem. Mater.* **2008**, *20*, 2921.
30. Petrov, K.; Zotov, N.; Mirtcheva, E.; Garciamartinez, O.; Rojas, R. M. *J. Mater. Chem.* **1994**, *4*, 611.
31. Brockner, W.; Ehrhardt, C.; Gjikaj, M. *Thermochim. Acta* **2007**, *456*, 64.
32. Estelle, J.; Salagre, P.; Cesteros, Y.; Serra, M.; Medina, F.; Sueiras, J. E. *Solid State Ionics* **2003**, *156*, 233.
33. Friedrich, H.; Sietsma, J. R. A.; de Jongh, P. E.; Verkley, A. J.; de Jong, K. P. *J. Am. Chem. Soc.* **2007**, *129*, 10249.

Chapter 6

Copper Nitrate Redispersion During Thermal Treatment

Impregnation of silica with copper nitrate followed by drying, calcination and reduction is a facile method to prepare supported copper catalysts. In this chapter we show that both the gas flow rate and the gas flow composition during calcination have a large effect on the copper nitrate genesis, final copper oxide and copper dispersion and catalytic activity for the butanal hydrogenation. Calcination in stagnant air resulted in severe agglomeration, yielding an average Cu particle size of 55 nm (calculated from N_2O chemisorption) after reduction. The presence of a flow of 2% v/v NO/N_2 during calcination resulted in highly dispersed CuO (6-8 nm, depending on the support type) with a narrow particle size distribution, in agreement with results obtained for cobalt and nickel in Chapter 2-5. *In situ* XRD and DRIFTS showed that the decomposition of copper nitrate in NO occurred via highly dispersed copper hydroxynitrate, while in N_2 or air decomposition occurred partly via copper nitrate anhydrate and partly via poorly dispersed copper hydroxynitrate. Unexpectedly, the copper specific surface areas and catalytic activities obtained after calcination in an N_2, air or NO flow, followed by reduction, were very similar. The high CuO dispersion after calcination in an N_2 or air flow, in contrast to results for NiO and Co_3O_4, was ascribed to the mobility of copper nitrate anhydrate, leading to redispersion of this phase over the support and thereby a higher copper oxide dispersion. In this case, a bi-modal distribution was obtained, which resulted in a poor correlation between the Cu particle and CuO crystallite size.

Introduction

Supported copper nanoparticles are widely applied because of their high activity in reactions such as the (de)hydrogenation of aldehydes and alcohols,[1-8] toluene oxidation,[9] the water-gas shift reaction,[10-11] the hydrogenolysis of esters[12-13] and the production of methanol from syngas.[14-17] Copper catalysts are often prepared via co-precipitation because of the high loadings that can be achieved while retaining a high copper dispersion and a good stability.[13-15,18] However, this method produces large amounts of waste water. Alternative methods have been explored such as chemical vapour deposition,[19-20] colloidal routes,[21] and sol-gel synthesis.[22] Preparation via pore volume impregnation is especially desirable because of its practical simplicity and small waste streams. A large number of metal precursors is available, including copper citrate, acetate, chloride and nitrate. The use of the latter precursor is generally preferred because of its low cost, high solubility in water and facile removal of the anion. However, metal particles prepared from nitrates are generally large (>10 nm), which has been ascribed to agglomeration during the drying and calcination step.[2,23-25]

A wide range of methods to (partially) counter the nickel, cobalt and copper nitrate agglomeration have been reported, including the replacement of the air calcination by glow discharge plasma assisted nitrate decomposition[26] and the direct reduction of the metal nitrate to the metal, omitting air thermal treatment.[5,25,27-28] Another approach is fast removal of the decomposition gasses via high space velocities or evacuation.[24,29] We have previously reported that agglomeration of cobalt and nickel nitrate can effectively be prevented by the replacement of the traditional air calcination by a thermal treatment in 1% v/v NO/He flow, resulting in high NiO and Co_3O_4 dispersions.[30-31] For silica supported copper nitrate, it was reported that the drying step is of vital importance to the particle size distribution.[5] Drying at elevated temperatures resulted in agglomeration during the hydrolysis of copper nitrate hydrate to copper hydroxynitrate.[5,32-33] Drying at ambient temperatures prevented the formation of large copper hydroxynitrate crystals, but subsequent calcination still resulted in broad particle size distributions. Direct reduction of the room temperature dried samples yielded a higher dispersion, but is generally undesirable due to the exothermic formation of ammonia. It is therefore desirable to obtain high dispersions via a calcination method.

In this Chapter the impact of the gas flow and composition during calcination on the final copper metal surface area and catalytic activity for the butanal hydrogenation was studied. It was found that the copper metal surface area is highly dependent on the gas flow rate during calcination, which is clearly demonstrated

by the large difference in copper surface area after calcination in stagnant air (~10 m^2 g_{cu}^{-1}) compared to an air flow (~100 m^2 g_{cu}^{-1}). In addition, the gas flow composition had a large effect on the copper nitrate genesis and dispersion after calcination, which will be demonstrated using *in situ* XRD and DRIFT spectroscopy.

Experimental

Catalyst preparation

Davicat 1404 silica gel, supplied by Grace Davidson (BET SA = 553 m^2 g^{-1}, PV = 0.9 ml g^{-1}, PD = 7 nm), was sieved to a particle size of 200-400 μm. Samples containing 18 wt% of Cu were prepared by impregnation of the sieved silica support to incipient wetness with a 4M copper nitrate solution (acidified to pH 1 with HNO_3). After an equilibration time of 15 minutes, two different routes were taken. The first route involved transfer to a tubular reactor, where after a 15 min drying period in a flow of gas (equal to the gas flow during calcination), the sample was heated to 350 °C (2 °C min^{-1}) in a flow of 2% v/v NO/N_2, air, or N_2 and kept at this temperature for 30 min. In addition, the gas hourly space velocity (GHSV) during thermal treatment was varied from 0-15000 h^{-1}. Alternatively, the impregnate was first dried at 120 °C in static air for 16 hours before calcination in a flow of air at a GHSV of 15000 h^{-1}.

For the *in situ* XRD and DRIFTS measurements, and TEM analysis, SBA-15 (BET surface area 705 m^2 g^{-1}, pore volume 0.8 cm^3 g^{-1}, pore diameter 9 ± 0.5 nm)[35] supported copper nitrate was used. The impregnation was performed as for the silica gel samples, yielding a 17 wt% Cu loading. The samples used for the *in situ* XRD experiments and TEM were impregnated with a solution with a slightly lower concentration (3M instead of 4M), leading to a 13 wt% Cu loading. After impregnation the sample was dried in a dessicator at room temperature for 24 hours, and is further denoted as Cu/SBA. Calcination in a tubular reactor in air or 2% v/v NO/N_2 was performed as described above at a GHSV of 15000 h^{-1}. The samples will be further denoted as CuSBA-air and CuSBA-NO, respectively.

An overview of the experimental details of the treatments and corresponding sample designations and physical properties is given in Table 1.

Table 1. Sample preparation, designation and physical properties. CuO crystallite size calculated from XRD line broadening analysis of the calcined catalysts, and copper surface area and particle size determined from N_2O chemisorption of the reduced catalyst.

Sample	**Drying**	**Calcination**			**Physical properties**		
	Gas, temperature, duration	Temperature** (°C)	Gas atmosphere	GHSV (h^{-1})	CuO crystallite size (nm)	Cu surface area ($m^2\ g_{cu}^{-1}$)	Cu particle size (nm)
CuSG-0	air flow, RT, 15 min	350	Air	0	36	12	55
CuSG-250	air flow, RT, 15 min	350	Air	250	34	88	7.6
CuSG-1000	air flow, RT, 15 min	350	Air	1000	30	85	7.9
CuSG-5000	air flow, RT, 15 min	350	Air	5000	28	91	7.3
CuSG-15000	air flow, RT, 15 min	350	Air	15000	20	110	6.0
CuSBA-air	dessicator*, RT, 24 h	350	Air	15000	23	130	5.2
CuSG-120-air	stagnant*, 120°C, 16 h	350	Air	15000	20	106	6.3
CuSG –NO	2% NO/N_2 flow, RT, 15 min	350	2% NO/N_2	15000	8.5	84	8.0
CuSBA-NO	dessicator*, RT, 24 h	350	2% NO/N_2	15000	6.5	120	5.6
CuSG-N_2	N_2 flow, RT, 15 min	350	N_2	15000	28	108	6.2

*Dried prior to loading into the reactor. **The temperature ramp during thermal treatment was 2 °C min^{-1}

Characterization

XRD patterns were obtained at room temperature from 20° to 60° 2θ with a Bruker-Nonius D8 Advance X-ray diffractometer set-up using Co-$K_{\alpha 12}$ (λ=1.79026 Å) radiation. The diffraction patterns were normalized to the intensity of the amorphous silica scattering band. Average crystallite sizes were calculated from XRD line broadening using the Debye-Scherrer equation. For *in situ* XRD experiments the Bruker-Nonius D8 Advance X-ray diffractometer was equipped with an Anton-Paar XRK reaction chamber. In a typical experiment the dried impregnate (40 mg) was heated in a 10% v/v O_2/N_2 or a 10% v/v NO/He flow (90 ml·min^{-1}) to 350 ºC with a ramp of 1 ºC·min^{-1}.

The copper surface area was determined via N_2O chemisorption at 68 °C after reduction at 230 ºC, assuming an N_2O:Cu stochiometry of 0.5 and a copper surface atom density of $1.0 \cdot 10^{19}$ atoms m^{-2}. The copper particle diameter (d_{cu}) was calculated assuming a spherical particle shape using the equation below:

$$d_{Cu}(\text{nm}) = \frac{6000}{S \cdot \rho_{Cu}}$$

with *S:* copper specific surface area (m^2 g^{-1}), ρ_{cu}= copper density (8.92 g cm^{-3}).

Transmission electron microscopy images were obtained on a Technai 20 apparatus, operated at 200 keV.

In situ DRIFTS measurements were performed with a Bruker Tensor 27 apparatus utilising a HVC-DRP-3 diffuse reflectance reaction chamber with CaF_2 windows and an MCT detector. In order to minimize temperature gradients within the sample, the bottom of the sample cup was filled with silicon carbide and covered by a grid, creating a cup of about 1 to 2 mm deep for the actual sample (±15 mg). Non absorbing KBr background scans were taken at 25 ºC. The flow rate during all experiments was 10 ml·min^{-1} and the gas was flowed through the sample from top to bottom. The different gasses used during the experiments were 20% v/v O_2/N_2, N_2 and 1% v/v NO/He. Usually 50 scans were recorded from 4000 to 1000 cm^{-1} at a resolution of 4 cm^{-1}. Spectra were taken at two minute intervals. In a typical experiment the cell was first flushed with N_2 at ambient temperature for 10 minutes, followed by the introduction of the gas flow to be used in the experiment. After 10 minutes equilibration, the temperature was raised to 350 ºC with a ramp of 1 ºC·min^{-1}.

Catalytic testing

The silica-gel based catalysts were tested for the gas phase hydrogenation of butanal. Typically 200 mg of catalyst was mixed with 500 mg silicon carbide

and loaded into a ¼ inch diameter reactor. Quartz wool was used to support the catalyst bed. A total of 7 catalysts were tested in parallel. Prior to the reaction the catalysts were reduced at 230 °C at a pressure of 2 bar in a 400 ml min^{-1} 2% H_2/N_2 flow. After activation the 2 bar pressure was maintained and the temperature decreased to 160 °C. The reaction was started by feeding butanal (98% pure) with a liquid flow rate of 0.167 ml min^{-1} (LHSV = 25 h^{-1}) and H_2 with a flow rate of 400 ml min^{-1} (H_2/butanal = 10 mol/mol). The hydrogenation was done at 160 °C for 72 hours, followed by 24 hours at 150 °C. The yield and selectivity were determined via liquid sample analysis on a HP6890 series GC apparatus.

Results

Structural characterization

A series of silica-supported copper catalysts was prepared by variation of the gas composition and the gas flow during calcination, and characterized using XRD, N_2O chemisorption and TEM. An overview of the CuO crystallite sizes after calcination, and copper surface areas and calculated Cu particle sizes after reduction is given in Table 1.

Calcined catalysts

After calcination, CuO diffraction lines were observed for all samples. Line broadening analysis suggested poorly dispersed copper oxide was obtained after calcination in air or N_2 flow, irrespective of the flow rate. However, the intensity of the diffraction lines, as normalized on the silica scattering band (Figure 1), indicated the amount of crystalline material was significantly higher for the sample calcined in stagnant air compared to samples calcined in a gas flow. Thus, it is likely that only a fraction of the CuO is crystalline in the samples calcined in a flow of air, while the remainder is amorphous and/or highly dispersed. Thermal treatment in a flow of N_2 (CuSG-N_2) showed only very weak diffraction lines, which could indicate a very high dispersion was obtained in this case. Calcination in a flow of NO/N_2 (CuSG-NO), resulted in a much smaller average crystallite size compared to air and N_2, as expected from the results for Ni and Co in the previous chapters. However, the crystallinity after calcination in NO was significantly higher compared to CuSG-N_2 and Cu-SG-15000. The difference between the samples calcined in air and NO/N_2 flow was further investigated using TEM.

TEM analysis of the sample calcined in a 2% v/v NO/N_2 flow (Figure 2) showed numerous small (2-9 nm) CuO particles inside the pores in addition to a few 10-30 nm particles on the external surface. The small average crystallite size

and narrow particle size distribution is well in agreement with the results previously obtained for nickel and cobalt (Chapter 2-5). Furthermore, a good agreement between the CuO crystallite size (XRD) and the CuO particle size (TEM) was found.

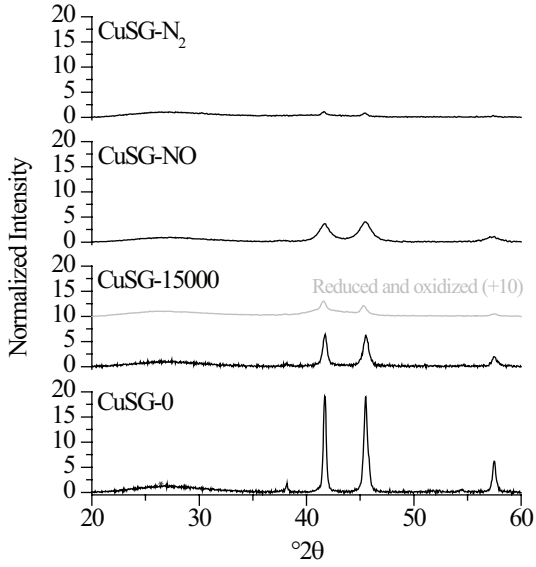

Figure 1. CuO diffraction patterns of CuSG samples after calcination as a function of gas atmosphere and flow rate. The intensity has been normalized to that of the amorphous SiO_2 scattering band (*).

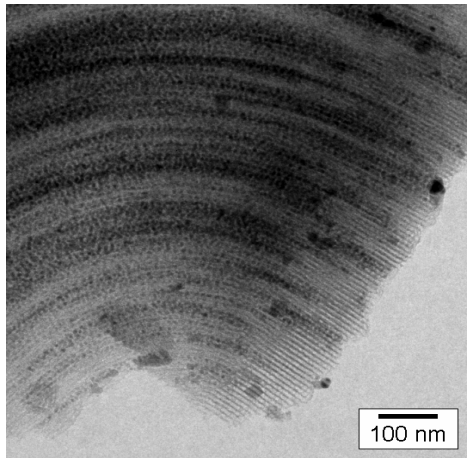

Figure 2. TEM image of Cu/SBA-15 after calcination in 1% v/v NO/He

Analysis of a CuSBA-air (GHSV = 15000 h^{-1}) sample, on the other hand,

did not show severely agglomerated CuO, as would be expected based on the results for cobalt and nickel. Instead, very few large CuO crystals were observed on the external surface and the pores seemed empty (Figure 3), indicating the copper phase was mostly highly dispersed. Combining XRD and TEM results, we conclude that for thermal treatment in an air flow a bi-modal particle size distribution of finely dispersed CuO, not detected with TEM or XRD (Figure 3, left), and very large CuO agglomerates (Figure 3, right) was apparent. The CuO agglomerates are responsible for the large average crystallite size that is observed for the samples calcined in a flow of N_2 or air, while the highly dispersed CuO explains the low crystallinity. The origin of the unexpectedly high dispersion after calcination in an N_2 or air flow is further investigated below.

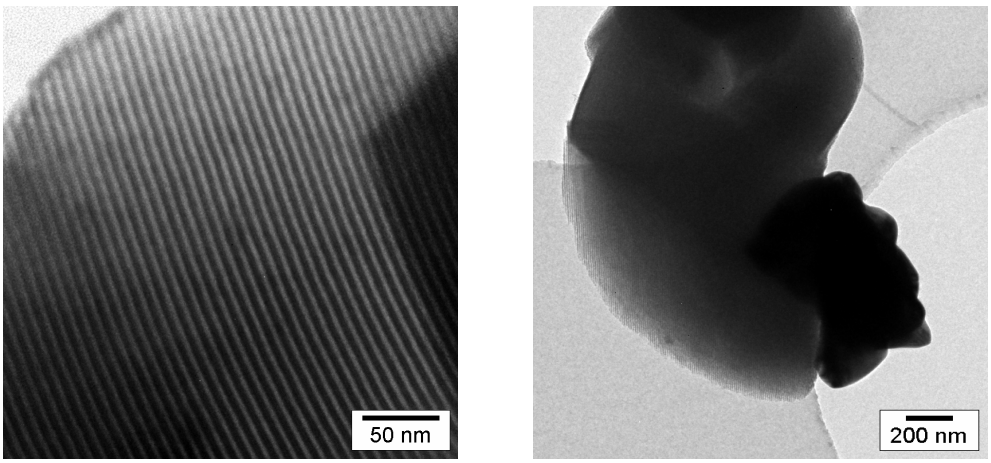

Figure 3. TEM images of Cu/SBA-15 calcined in an air flow (GHSV = 15000 h^{-1}).

Reduced catalysts

The copper surface areas of the reduced catalysts were determined using N_2O chemisorption (Table 1). It was found that a gas flow during calcination was essential to obtain a high copper surface area (Table 1). A low gas flow was already sufficient to significantly enhance the copper surface area when compared to calcination in stagnant air. A gradual increase in surface area was observed with increasing space velocity. The beneficial effect of a flow of gas during calcination is in agreement with previous work on Co/Al_2O_3 by Van de Loosdrecht et al.[24] They postulated that the faster removal of the decomposition gasses was responsible for the higher dispersion, which was based on a report where inhibited removal of the decomposition gasses increased the particle size.[35] For unsupported nickel nitrate hexahydrate a similar

effect has been reported, where a decreased pressure yielded higher surface areas.[29]

The CuO crystallite sizes from XRD were distinctly different from the Cu particle sizes calculated from the N_2O data. That the crystallite size calculated from the line broadening of the CuO diffraction lines is not directly related to the copper surface area can be explained by a low degree of crystallinity and a broad particle size distribution observed with TEM (Figure 3). The diffraction pattern of CuSG-15000 taken after reduction and re-oxidation suggests a bi-modal distribution (Figure 1). The crystallinity after reduction and oxidation appeared lower, which may either have resulted from fragmentation of the larger crystals or poor crystallization.

The sample calcined in NO/N_2 was the only sample where the CuO crystallite size and the Cu particle size coincided, which is in line with the results for Ni and Co in Chapter 4. Furthermore, the average copper particle size is retained during reduction, indicating limited sintering. That the copper specific surface areas of the samples calcined in air and NO/N_2 are similar is unexpected and probably excidental as for cobalt and nickel large differences in surface area and catalytic activity were observed.[37-39]

Previously it has been reported that drying of silica impregnated with copper nitrate at elevated temperatures (≥90 °C) results in broad particle size distributions, due to the formation of large copper hydroxynitrate crystals.[5,32] We investigated the effect of this drying treatment on the copper surface area by comparison of the CuSG-15000 sample, which had been dried in a flow of air at room temperature, with a sample that had been dried at 120 °C (CuSG-120-air, GHSV = 15000 h^{-1}). As shown in Table 1, no significant difference in copper surface area is observed between the CuSG-15000 and CuSG-120-air sample. This is surprising as, in agreement with literature, very large copper hydroxynitrate crystals had formed during drying (confirmed by XRD and TEM, not shown) and, therefore, partial redispersion must have occurred. This observation will be further discussed below.

It must be noted that the copper surface areas that were obtained on SBA-15 were higher, i.e. 130 $m^2\ g_{Cu}^{-1}$ for air and 120 $m^2\ g_{Cu}^{-1}$ for 2% NO/N_2, than for silica gel (Table 1). This can be ascribed to the higher support surface area and the smaller mesoscopic particle size (~90 μm for silica gel and ~1-5 μm for SBA-15), resulting in more facile water removal during the drying/decomposition. This influences the mobility of the hydrolyzed species and thus the extent of agglomeration, which is further explained below.

Catalytic activity

The catalytic activities of the silica-gel based (CuSG) samples after reduction were

measured at 160 °C in the gas-phase hydrogenation of butanal. Conversions ranging from 10-80% were obtained for the different samples. The butanol selectivity of the samples was around 97% in all cases, with the exception of CuSG-0 which had a lower selectivity (80%). Deactivation studies were not performed, but within the 72 hour test the deactivation was negligible. The influence of the GHSV during calcination on the activity is shown in Figure 4.

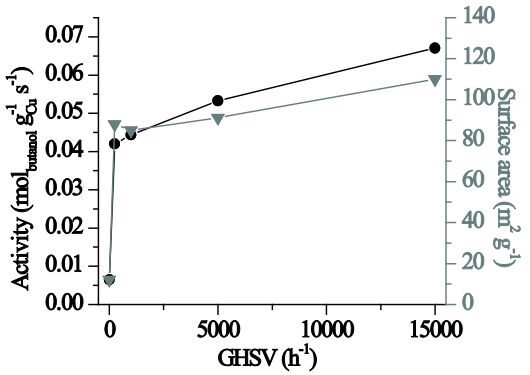

Figure 4. Copper weight normalized activity for the butanal hydrogenation at 160 °C (●) as a function of the air flow rate during calcination. The specific copper surface area (▼) is also shown. Butanal liquid space velocity 25 h^{-1} (H_2:Butanal = 10 mol/mol).

The surface area and the activity followed the same trend upon increasing GHSV during calcination. As with the copper surface area, the activity sharply increased going from calcination in stagnant air to a flow of air, while it only slightly increased upon further increasing of the space velocity. Often the crystallite size from XRD is taken as a measure of the dispersion and correlates to the activity. However, from these results we can conclude that in the case of copper, the CuO crystallite size from XRD does not directly correlate to catalytic activity of Cu/SiO_2.

The activities of the samples thermally treated in different atmospheres at a constant GHSV of 15000 h^{-1} are shown in Figure 5. In general, very similar activities were observed, which is in agreement with the similar copper surface areas. It must be noted that the CuSG-120-air sample showed a slightly lower activity than expected from the surface area, while the NO thermally treated sample has a slightly higher activity than expected. The origin thereof remains unclear. Nevertheless, we can conclude that the difference between the air and NO thermal treatment of silica supported copper nitrate is much smaller than for nickel and cobalt nitrate. In these cases a much higher dispersion and catalytic activity was observed after calcination

in a diluted NO flow as compared to calcination in an air flow.[31,37] The origin of the small difference lies in the high dispersion after calcination in air and N_2 flow, which will be discussed below.

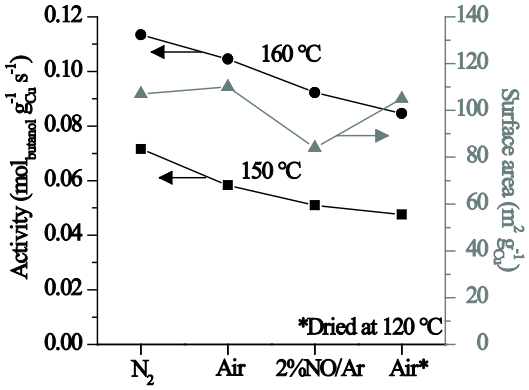

Figure 5. Copper weight normalized activity for the butanal hydrogenation as a function of the gas atmosphere during thermal treatment (GHSV = 15 000 h^{-1}). Activity at (■) 150 °C, (●) 160 °C, and the copper surface area (▲). Butanal liquid space velocity 50 h^{-1} (H_2:butanal = 10).

Vapour phase transport

The large discrepancy between the results obtained for copper nitrate compared to cobalt and nickel nitrate might be related to a remarkable observation during thermal treatment. In Figure 6 two empty glass reactors that have been used previously to calcine silica-supported copper nitrate samples under two different gas flows, i.e. air (left) and 2% v/v NO/N_2 (right), are depicted. The left reactor had a very thin layer of deposited copper species on the walls, which could be removed using an acidic solution. This black layer was observed after the calcination in an N_2 or air flow (dried and undried samples). The presence of the black layer indicates the copper species were mobile during calcination. Other authors also observed deposition of copper species on a glass IR cell during measurements on gaseous anhydrous copper nitrate above 225 °C.[38] The similarity between the observations could indicate anhydrous copper nitrate was formed during calcination. On the right side, the reactor used for calcination in a 2% NO/N_2 flow is shown. Here, no black layer was observed, indicating NO effectively inhibited vapour phase transport of copper species. For calcinations of supported nickel and cobalt nitrate samples no black layer has been observed, which indicates this behaviour is characteristic for copper nitrate.

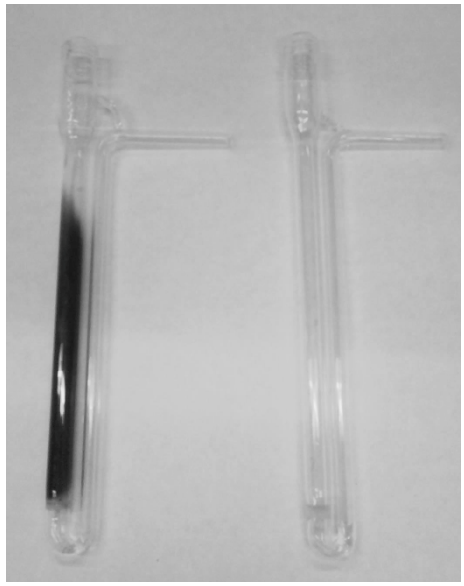

Figure 6. Image of a reactor used for calcination of silica supported copper nitrate in an N_2 or air flow(left), or in a 2% v/v NO/N_2 flow (right). The reactors have been emptied and washed with water.

The vapour phase transport was confirmed by the following experiment. A glass reactor (as depicted in Figure 6) was loaded with a thin layer of copper nitrate trihydrate, then a layer of glass wool, followed by a layer of silica gel. Subsequently, an up-flow heat treatment in N_2 or NO was performed, as described earlier. Above 200 °C during thermal treatment in N_2, the glass wool and the bottom part of the silica started to turn black and the top layers green, indicating the deposition of CuO. It must be noted that a large part of the copper oxide was still located on the bottom after completion of the calcination, indicating only a small part of the copper had been transported via the vapour phase. In contrast, calcination in NO left both the glass wool and silica completely white, indicating NO indeed effectively prevents the formation of gaseous intermediates during calcination. To elucidate the origin of this difference in mobility, the phase evolution was further investigated using *in situ* DRIFTS and XRD.

In situ XRD

The *in situ* studies were conducted using the model support SBA-15. The impregnation was conducted similar to the silica gel and a reference CuSG sample was measured with DRIFTS, which indicated the phase behaviour was the same on both supports. Figure 7 shows the XRD patterns recorded during the thermal treatment of Cu/SBA-15 in 10% v/v O_2/N_2 or 10% v/v NO/He flow. Two crystalline phases were identified, i.e. $Cu_2(OH)_3NO_3$ and CuO. In the presence of NO crystalline $Cu_2(OH)_3NO_3$ appeared at lower temperatures than in O_2/N_2, as observed previously for nickel and cobalt nitrate (Chapter 3).

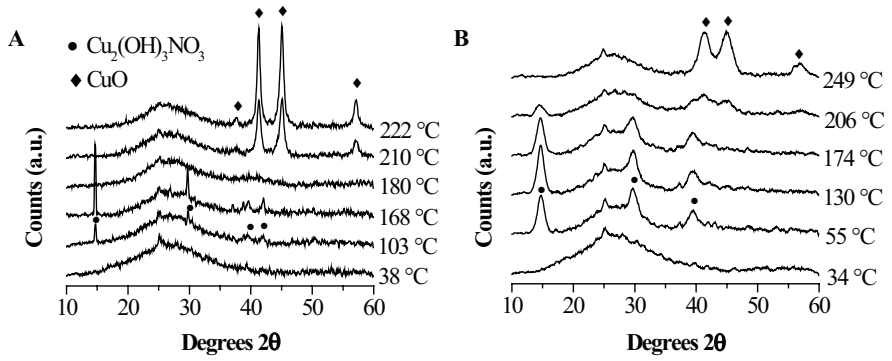

Figure 7. Diffraction patterns recorded during the thermal treatment of Cu/SBA-15 in A) 10% v/v O_2/N_2 and B) 10% v/v NO/He.

The $Cu_2(OH)_3NO_3$ (0 0 1) and CuO (1 1 1) diffraction lines were normalized to the maximum peak area during thermal treatment and plotted as a function of temperature in Figure 8. The low temperature appearance of $Cu_2(OH)_3NO_3$ in the presence of NO is clearly illustrated and it is now also apparent that this phase was stable up to higher temperatures in NO. In the O_2/N_2 thermal treatment the $Cu_2(OH)_3NO_3$ diffraction lines completely disappeared prior to the appearance of CuO diffraction lines. This result is in agreement with the proposed formation of a gaseous intermediate prior to the decomposition to CuO. In NO the intensities of the $Cu_2(OH)_3NO_3$ diffraction lines gradually decreased in intensity while the CuO intensity increased, indicating direct conversion of the one phase in the other, as was previously observed for nickel.[31] This is also in agreement with the absence of black deposits on the glass reactor. The nature of the possible intermediate that was formed during the O_2/N_2 thermal treatment was further investigated with diffuse reflectance Fourier transform infrared (DRIFT) spectroscopy.

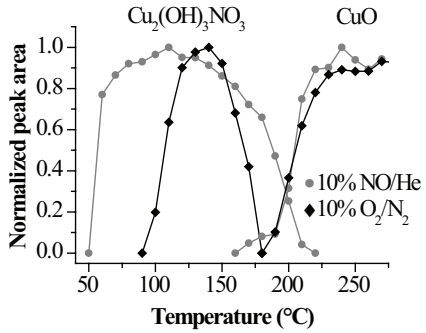

Figure 8. Normalized 14.6° ($Cu_2(OH)_3NO_3$) and 45.1° (CuO) 2θ peak areas as a function of temperature. Normalization on the maximum area during thermal treatment.

In situ DRIFTS

Figure 9 depicts the spectra recorded during calcination of Cu/SBA-15 in a 1% v/v NO/He flow. The spectra recorded during calcination in a 10% v/v NO/He flow did not significantly differ from those obtained in a 1% v/v NO/He flow, therefore, the former will not be discussed.

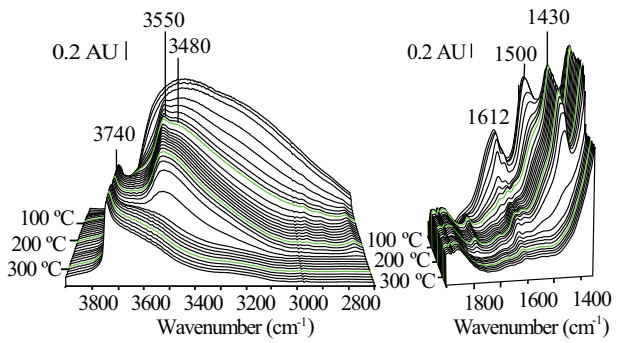

Figure 9. DRIFTS spectra recorded during the calcination of Cu/SBA-15 in a 1% v/v NO/He gas flow.

At room temperature, the spectra show a broad band in the hydroxyl region due to the presence of water in the sample. Already at 50 ºC, two bands at around 3550 and 3480 cm^{-1} appeared in the O-H region concurrent with a peak at 1430 cm^{-1}, belonging to the ν_{OH} and $\nu_4(NO_3^-)$ vibrations of copper hydroxynitrate, respectively.[32,39] The appearance of a $\nu_{as}(NO_2)$ band at 1612 cm^{-1} due to evolved NO_2 confirms significant decomposition took place already at low temperature. The initial peak at 1500 cm^{-1}, attributed to hydrated copper nitrate, rapidly disappeared upon

increasing of the temperature to 100 ºC. At 100 ºC the copper hydroxynitrate phase is almost exclusively present, but its intensity almost immediately starts to decline in agreement with XRD (Figure 8). Since copper hydroxynitrate was formed rapidly at slightly raised temperatures, it was suspected to form at room temperature under NO as well. This was confirmed by leaving a sample at 30 ºC while introducing NO; after 30 minutes basic copper nitrate was almost exclusively present in the sample (data not shown). Thus, we propose the phase evolution of copper nitrate in NO proceeds as shown below.

$$Cu(NO_3)_2 \cdot 3H_2O \xrightarrow{30\,^{\circ}C} Cu_2NO_3(OH)_3 \xrightarrow{200\text{-}230\,^{\circ}C} CuO \qquad (1)$$

The spectra recorded during the thermal treatment of Cu/SBA-15 in N_2 flow (Figure 10) are distinctly different from those in NO. Addition of O_2 to the stream of N_2 did not significantly affect the results and therefore only those obtained in an N_2 flow are discussed.

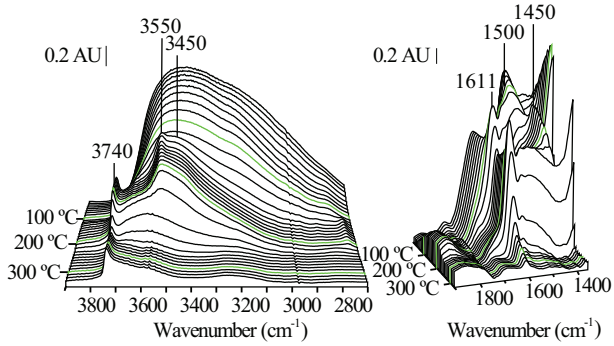

Figure 10. DRIFTS spectra recorded during the calcination of Cu/SBA-15 in a N_2 gas flow.

In Figure 10, a $\nu_4(NO_3^-)$ stretch vibration band is observed at 1500 cm^{-1}, which is ascribed to copper nitrate hydrate. The deviation from bulk copper nitrate trihydrate, which is reported to show one single degenerate ν_3 band at 1387 cm^{-1}, indicates the symmetry of the nitrate groups changed from D_{3h} to C_{2v} due to coordination to the support.[40] Dehydration was observed until at 120 ºC three bands appeared around 3550, 3450 and 1450 cm^{-1}, indicating the formation of copper hydroxynitrate. The higher temperature at which these bands appeared as compared to in NO is well in agreement with XRD results (Figure 8), and clearly shows that NO facilitates the formation of hydroxynitrates, as reported for nickel and cobalt nitrate in Chapter 3. In addition, a new band, that was only very weakly observed in NO, developed around 1611 cm^{-1}. At 210 ºC the copper hydroxynitrate decomposed, as is evident by the declining 3540, 3450 and 1450 cm^{-1} bands, while simultaneously the band at

1611 cm^{-1} became more intense. This suggested part of the copper hydroxynitrate was converted into another intermediate before decomposing into copper oxide, as was also observed with XRD. While the copper hydroxynitrate band disappeared and the band at 1611 cm^{-1} starts to decline, the ν_{SiOH} band at 3742 cm^{-1} also decreased in intensity. This was not observed for the NO thermal treatment, as is more apparent from Figure 11. Here, the intensity of the ν_{SiOH} band at 3742 cm^{-1}, normalized on the maximum intensity during thermal treatment, is plotted as a function of temperature.

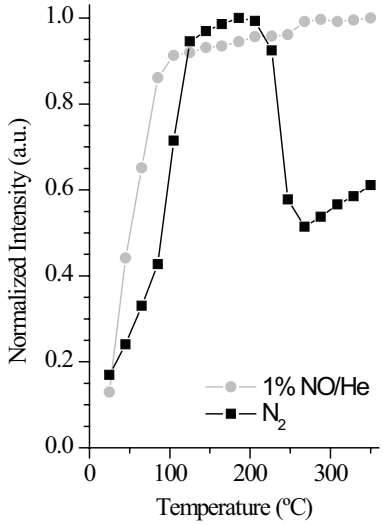

Figure 11. Intensity of the silanol ν_{OH} band at 3745 cm^{-1} as a function of temperature during the calcination of Cu/SBA-15 in N_2 (■) or 10% v/v NO/He (●) flow.

At room temperature the intensity of the silanol band is low due to interactions with water in the sample, but gradually increases as water is removed. A large increase in the ν_{SiOH} intensity was observed for both treatments concurrent with the formation copper hydroxynitrate, which was at lower temperatures for NO. In N_2 the intensity of the silanol band sharply decreased upon increasing intensity of the intermediate at 1611 cm^{-1}. Upon decomposition of the intermediate to CuO it slightly increased again, but did not fully recover. A blank experiment with the parent SBA-15 and the sample treated in NO indicated that no dehydroxylation took place under these conditions, and that the decrease in silanol band intensity could thus be ascribed to an interaction or reaction with the intermediate.

At 240 ºC, after the hydroxyl vibrations around 3500 cm^{-1} had largely disappeared, the band at 1611 cm^{-1} and its features at lower wave numbers were still

present (Figure 10), suggesting a dehydrated or even anhydrous copper nitrate had formed. Liberation of $Cu(NO_3)_2(g)$ from copper hydroxynitrate has been suggested before,[38] and at least two different structures of $Cu(NO_3)_2$ are known and have been studied by IR before, although actual details about the different structures are scarce.[41-42] Addison et al. found bands for β-$Cu(NO_3)_2$ at 1592, 1565, 1546 and 1504 cm^{-1}, in fair agreement with the sharp 1611 cm^{-1} band and accompanying features displayed here.[43] They attributed the bands at 1565 and 1546 cm^{-1} to the asymmetric ν_4, but thought the band at 1592 cm^{-1} originated from the $2\nu_6$ overtone. Given the original intensity of the ν_6 vibration they report this is actually unlikely; the alleged combination band is more intense than the original vibration, whereas overtones are always lower in intensity. Therefore, it is more likely this is also a ν_4 nitrate band, which was also proposed by Logan et al. after observing the same bands.[41] Taking into account the high mobility of the copper nitrate species during calcination and the assignment of vibrational bands both in position and intensities with β-anhydrous copper nitrate we propose the copper nitrate evolution in the presence of N_2 proceeds as shown in equation 2. As the anhydrous copper nitrate bands are already observed above 110 ºC, it is likely that part of the decomposition occurs via route 3. Especially at higher flow rates, where hydrolysis is suppressed, the latter route might be dominant.

$$Cu(NO_3)_2 \cdot 3H_2O\,(s) \xrightarrow{110^{\circ}C} Cu_2NO_3(OH)_3\,(s) \xrightarrow{150\text{-}230^{\circ}C} Cu(NO_3)_2\,(s,g)\,(+CuO\,(s)) \xrightarrow{180\text{-}300^{\circ}C} CuO\,(s) \quad (2)$$

$$Cu(NO_3)_2 \cdot 3H_2O\,(s) \xrightarrow{110\text{-}210^{\circ}C} Cu(NO_3)_2\,(s,g) \xrightarrow{180\text{-}300^{\circ}C} CuO\,(s) \quad (3)$$

It is now postulated that the relatively high dispersions that are obtained via thermal treatment in N_2 result from sublimation of anhydrous copper nitrate (at 255 ºC) and decomposition when in contact with a silica surface, leading to redispersion of the copper phase. A high reactivity towards various organic compounds is reported for anhydrous copper nitrates and bi-dentate nitrates in general.[44] Therefore we tentatively propose the loss of silanol groups resulted from a reaction of the silica surface with anhydrous copper nitrate. Assuming a silanol density of 2 OH groups per nm^2 and grafting of Cu onto two silanol groups, up to one third of the Cu can be atomically dispersed in this way. We tentatively propose the reaction proceeds as indicated below:

$$Cu(NO_3)_2\,(g) + 2\,Si(OH)\,(s) \longrightarrow (SiO)_2 - Cu\,(s) + H_2O\,(g) + 2\,NO_2\,(g) + \tfrac{1}{2}\,O_2\,(g) \quad (4)$$

The presence of a moderate gas flow is essential to remove water and thereby facilitate dehydration of copper nitrate hydrate, where after redispersion of copper nitrate anhydrate takes place. In addition, a high flow rate will inhibit the formation of copper hydroxynitrate agglomerates which will further increase the dispersion. In previous work on cobalt and nickel nitrate, gas phase redispersion was not observed and it is proposed that this explains the lower dispersions after N_2 and air thermal treatment.

Conclusions

Silica supported copper catalysts were prepared via copper nitrate impregnation, drying, calcination and reduction. The impact of the gas flow rate and composition during calcination on the copper nitrate genesis, final metal (oxide) dispersion and catalytic activity for the butanal hydrogenation was studied. A flow of gas during calcination was found to be essential to obtain a high dispersion (average Cu particle size <10 nm) and an active catalyst, but only moderate flows were needed to significantly enhance the copper specific surface area when compared to stagnant air (55 nm average Cu particle size). It is postulated that water removal during decomposition is essential to prevent agglomeration.

In addition, *in situ* XRD and DRIFTS showed that the composition of the gas flow had a major impact on the copper nitrate genesis and final metal oxide dispersion. In a flow of NO/N_2, copper nitrate hydrate was rapidly and fully converted to small (9 nm) copper hydroxynitrate crystallites followed by decomposition to CuO particles with an average size of 6-8 nm and a narrow particle size distribution. Surprisingly, decomposition in an O_2 and/or N_2 flow also yielded a high copper oxide dispersion, in contrast to results presented for nickel and cobalt nitrate in Chapter 2-5. Decomposition in O_2/N_2 occurred at least partly via an intermediate that was identified as copper nitrate anhydrate, a species able to sublime. Mobility of this compound during the thermal treatment in the presence of a flow resulted in redispersion of the copper nitrate phase, as apparent from the (limited) deposition on the reactor walls and loss of silanol groups. Due to partial decomposition via poorly dispersed copper hydroxynitrate (>25 nm crystallites), a bi-modal distribution was obtained, which resulted in a poor correlation between the CuO crystallite size (XRD) and the CuO particle size (TEM). It is proposed that gas phase redispersion, which is not observed for cobalt and nickel nitrate, is the origin of the high copper oxide dispersions in an N_2 and air flow. These results illustrate the importance of in-depth fundamental studies of phase transitions during catalyst preparation.

Acknowledgments
The authors kindly thank Marjan Versluijs-Helder for the *in situ* XRD measurements, Fouad Soulimani for his assistance with the DRIFT measurements, Heiner Friedrich for the TEM analysis, Colin Ranson for the copper surface area determination and David Maclachlan for the XRF analysis. Anders Gabrielsson, Steve Pollington, Gareth Headdock and John Casci are acknowledged for the hydrogenation experiments and valuable discussions.

References

1. Ai, M. *Appl. Catal.* **1984**, *11*, 259.
2. Guerreiro, E. D.; Gorriz, O. F.; Larsen, G.; Arrúa, L. A. *Appl. Catal. A: Gen.* **2000**, *204*, 33.
3. Guerreiro, E. D.; Gorriz, O. F.; Rivarola, J. B.; Arrúa, L. A. *Appl. Catal. A: Gen.* **1997**, *165*, 259.
4. Guerrero-Ruiz, A.; Rodriguez-Ramos, I.; Fierro, J. L. G. *Appl. Catal.* **1991**, *72*, 119.
5. Toupance, T.; Kermarec, M.; Louis, C. *J. Phys. Chem. B* **2000**, *104*, 965.
6. Wang, Z.; Liu, Q.; Yu, J.; Wu, T.; Wang, G. *Appl. Catal. A* **2003**, *239*, 87.
7. Marchi, A. J.; Fierro, J. L. G.; Santamaría, J.; Monzón, A. *Appl. Catal. A: Gen.* **1996**, *142*, 375.
8. Marchi, A. J.; Gordo, D. A.; Trasarti, A. F.; Apesteguía, C. R. *Appl. Catal. A: Gen.* **2003**, *249*, 53.
9. Suh, M.-J.; Ihm, S.-K. *Topics in Catalysis* **2010**, *53*, 447.
10. Kuijpers, E. G. M.; Tjepkema, R. B.; van der Wal, W. J. J.; Mesters, C. M. A. M.; Spronck, S. F. G. M.; Geus, J. W. *Appl. Catal.* **1986**, *25*, 139.
11. Yeragi, D.; Pradhan, N.; Dalai, A. *Catal. Lett.* **2006**, *112*, 139.
12. Chen, L.; Guo, P.; Zhu, L.; Qiao, M.; Shen, W.; Xu, H.; Fan, K. *Appl. Catal. A: Gen.* **2009**, *356*, 129.
13. Huang, Z.; Cui, F.; Kang, H.; Chen, J.; Zhang, X.; Xia, C. *Chem. Mater.* **2008**, *20*, 5090.
14. Herman, R. G.; Klier, K.; Simmons, G. W.; Finn, B. P.; Bulko, J. B.; Kobylinski, T. P. *J. Catal.* **1979**, *56*, 407.
15. Liu, X.-M.; Lu, G. Q.; Yan, Z.-F.; Beltramini, J. *Ind. Eng. Chem. Res.* **2003**, *42*, 6518.
16. Kasatkin, I.; Kurr, P.; Kniep, B.; Trunschke, A.; Schlögl, R. *Angew. Chem. Int. Ed.* **2007**, *46*, 7324.
17. Behrens, M.; Furche, A.; Kasatkin, I.; Trunschke, A.; Busser, W.; Muhler, M.;

Kniep, B.; Fischer, R.; Schlögl, R. *ChemCatChem* **2010**, *2*, 816.
18. Porta, P.; De Rossi, S.; Ferraris, G.; Lo Jacono, M.; Minelli, G.; Moretti, G. *J. Catal.* **1988**, *109*, 367.
19. Becker, M.; d'Alnoncourt, R. N.; Kähler, K.; Sekulic, J.; Fischer, R. A.; Muhler, M. *Chem. Vapor Depos.* **2010**, *16*, 85.
20. Kurtz, M.; Bauer, N.; Büscher, C.; Wilmer, H.; Hinrichsen, O.; Becker, R.; Rabe, S.; Merz, K.; Driess, M.; Fischer, R.; Muhler, M. *Catal. Lett.* **2004**, *92*, 49.
21. Schimpf, S.; Rittermeier, A.; Zhang, X.; Li, Z.-A.; Spasova, M.; van den Berg, Mauritz W. E.; Farle, M.; Wang, Y.; Fischer, Roland A.; Muhler, M. *ChemCatChem* **2010**, *2*, 214.
22. Sun, Y.; Sermon, P. A. *Top. Catal.* **1994**, *1*, 145.
23. van Dillen, A. J.; Terörde, R. J. A. M.; Lensveld, D. J.; Geus, J. W.; de Jong, K. P. *J. Catal.* **2003**, *216*, 257.
24. van de Loosdrecht, J.; Barradas, S.; Caricato, E. A.; Ngwenya, N. G.; Nkwanyana, P. S.; Rawat, M. A. S.; Sigwebela, B. H.; van Berge, P. J.; Visagie, J. L. *Top. Catal.* **2003**, *26*, 121.
25. Sietsma, J. R. A.; Meeldijk, J. D.; Versluijs-Helder, M.; Broersma, A.; van Dillen, A. J.; de Jongh, P. E.; de Jong, K. P. *Chem. Mater.* **2008**, *20*, 2921.
26. Chu, W.; Wang, L.; Chernavskii, P.; Khodakov, A. Y. *Angew. Chem. Int. Ed.* **2008**, *47*, 5052
27. Bartholomew, C. H.; Farrauto, R. J. *J. Catal.* **1976**, *45*, 41.
28. Louis, C.; Xing Cheng, Z.; Che, M. *J. Phys. Chem.* **1993**, *97*, 5703.
29. Llewellyn, P. L.; Chevrota, V.; J. Ragaib; Cerclier, O.; Estienne, J.; Rouquerol, F. *Solid State lonics* **1997**, *101-103* 1293.
30. Sietsma, J. R. A.; Meeldijk, J. D.; den Breejen, J. P.; Versluijs-Helder, M.; van Dillen, A. J.; de Jongh, P. E.; de Jong, K. P. *Angew. Chem. Int. Ed.* **2007**, *46*, 4547
31. Sietsma, J. R. A.; Friedrich, H.; Broersma, A.; Versluijs-Helder, M.; Jos van Dillen, A.; de Jongh, P. E.; de Jong, K. P. *J. Catal.* **2008**, *260*, 227.
32. Catillon-Mucherie, S.; Ammari, F.; Krafft, J. M.; Lauron-Pernot, H.; Touroude, R.; Louis, C. *J. Phys. Chem. C* **2007**, *111*, 11619.
33. Catillon-Mucherie, S. p.; Lauron-Pernot, H. l. n.; Louis, C. *J. Phys. Chem. C* **2010**, *114*, 11140.
34. Zhao, D.; Feng, J.; Huo, Q.; Melosh, N.; Fredrickson, G. H.; Chmelka, B. F.; Stucky, G. D. *Science* **1998**, *279*, 548.
35. Reinalda, D.; Kars, J., EP 0,421,502, **1990**.
36. Advances in Fischer-Tropsch Synthesis, Catalysts and Catalysis; Davis, B. H.; Occelli, M. L., Eds.; CRC Press, 2009.
37. den Breejen, J. P.; Sietsma, J. R. A.; Friedrich, H.; Bitter, J. H.; de Jong, K. P. *J.*

Catal. **2010**, *270*, 146.
38. Addison, C. C.; Hathaway, B. J. *J. Chem. Soc.* **1958**, 3099.
39. Zotov, N.; Petrov, K.; Dimitrova-Pankova, M. *J. Phys. Chem. Solids* **1990**, *51*, 1199.
40. Hadjiivanov, K. I. *Catal. Rev. Sci. Eng.* **2000**, *42*, 71.
41. Logan, N.; Simpson, W. B. *Spectrochim. Acta* **1965**, *21*, 857.
42. James, D. W.; Kimber, G. M. *Inorg. Nucl. Chem. Letters* **1969**, *5*, 609.
43. Addison, C. C.; Gatehouse, B. M. *J. Chem. Soc.*. **1960**, 613.
44. Addison, C. C. *Coordin. Chem. Rev.* **1966**, *1*, 58.

Chapter 7

Summary and Concluding Remarks

High surface area supported metal oxide catalysts are essential for the production of fuels, chemicals, pharmaceuticals and the abatement of environmental pollution. Impregnation of high surface area supports, often silica or alumina, followed by drying and calcination is one of the most frequently applied methods to prepare these materials because of its practical simplicity, cost efficiency and small waste streams. Metal nitrates are often preferred as precursor because of their high solubility in water and low costs. However, often low specific metal surface areas are obtained due to metal nitrate redistribution and agglomeration during drying and calcination. Previous studies in this group revealed that decomposition of nickel or cobalt nitrates supported on silica in a flow of 1% v/v NO/He prevents agglomeration, yielding highly dispersed NiO and Co_3O_4. The goal of the research described in this thesis is to understand the mechanism by which NO prevents agglomeration of metal nitrates, and the relation between the metal nitrate decomposition pathway and the final metal oxide dispersion. To this end, the phase evolution of a wide range of metal nitrates was studied using advanced *in* and *ex situ* characterization techniques, including x-ray diffraction (XRD), diffuse reflectance FTIR spectroscopy (DRIFTS), thermal gravimetric analysis (TGA) and transmission electron microscopy (TEM).

In **Chapter 2,** TGA combined with mass spectrometry (MS), XRD and TEM was used to explore the impact of an 10% v/v NO/Ar flow on the decomposition pathway and dispersion of the transition metal nitrates of Sc, Fe, Mn, Co, Ni, Cu and Zn in the 25-750 °C temperature range. It was shown that the presence of NO lowered the temperature of decomposition significantly for all investigated metal nitrates. For cobalt and nickel nitrate it was verified that an NO/Ar flow during decomposition led to an improved metal oxide dispersion, where decomposition in an Ar flow resulted in agglomeration. It was found that NO, in contrast to Ar, induced rapid hydrolysis of cobalt, nickel, and copper nitrate to highly dispersed metal hydroxynitrates at low temperatures (≤150 °C). Hence, it was demonstrated that NO affects the decomposition already at low temperature.

The impact of NO at low temperature (≤150 °C) was further investigated in **Chapter 3** where *in situ* XRD and DRIFTS were employed to study the phase evolution of supported nickel and cobalt nitrate in more detail. Both XRD and DRIFTS showed that thermal treatment of the supported nickel and cobalt nitrates in an NO/N_2 flow resulted in rapid and nearly complete hydrolysis to anhydrous nickel or cobalt hydroxynitrates of the form $M_x(OH)_y(NO_3)_z$ below 150 °C , while hydrolysis in an N_2 or O_2/N_2 flow was slow and incomplete. The increased hydrolysis at low temperatures was ascribed to the decrease in the Gibbs free energy of the decomposition in the presence of NO. Furthermore, based on DRIFT spectra it is postulated that at least part of the species formed in N_2 or O_2 were hydrated

hydroxynitrates of the form $Ni_x(OH)_y(NO_3)_z \bullet aH_2O$. From an experiment in which all soluble compounds ($Ni_x(NO_3)_y \bullet aH_2O$ and $Ni_x(OH)_y(NO_3)_z \bullet aH_2O$) formed after thermal treatment at 150 °C were removed, it was determined that NO thermal treatment at 150 °C converted 85% of the nickel nitrate hydrate to insoluble $Ni_x(OH)_y(NO_3)_z$. In contrast, the same thermal treatment in N_2 converted only 25% to $Ni_x(OH)_y(NO_3)_z$. Direct stagnant air thermal treatment after the drying treatment at 450 °C, without removing the soluble species, yielded 9 nm and 32 nm NiO crystal domains, respectively. Thus it was shown that the insoluble $Ni_x(OH)_y(NO_3)_z$ species exhibited a reduced mobility. In conclusion, a key to the high NiO and Co_3O_4 dispersions from nitrate precursors is the immobilization by means of hydrolysis to cobalt and nickel hydroxynitrates at relatively low temperatures.

Although the major impact of NO/N_2 flow is at low temperature (≤150 °C), the dispersion is further improved by the presence of NO during the entire decomposition process. The impact of an NO/He flow on the decomposition of silica supported nickel (hydroxy)nitrate at high temperature (>120 °C) was investigated in **Chapter 4**. Here, a comparison of the gas evolution during thermal decomposition in ^{14}NO, ^{15}NO, $^{16}O_2$, $^{18}O_2$, and Ar revealed that NO scavenges oxygen species during the final decomposition step in the 225-300 °C temperature range. It was proposed that oxygen scavenging by NO results in the depletion of the nitrate groups of the precursor, thereby forming more nucleation sites for NiO and immobilizing the nickel hydroxynitrate. DRIFTS spectra taken during the decomposition support this assignment as in the presence of NO not only a decrease in the intensity of the ν_{OH} and $\nu_4(\text{-}ONO_2)$ precursor vibration bands is observed, but also a simultaneous blue and red shift of their respective frequencies. Similar observations for the high temperature (≥150 °C) decomposition in N_2O or H_2 flow indicated this research can be extended to a wide range of gases able to scavenge oxygen.

For many catalytic processes such as the Fisher-Tropsch synthesis there is an optimum particle size for the activity and therefore control over the particle size and distribution is essential. In **Chapter 5** ordered mesoporous supports were applied to tune the average NiO and Co_3O_4 crystallite size by variation of the support pore diameter. Essential to obtain highly dispersed particles with narrow particle size distributions from supported metal nitrates was the presence of NO during thermal decomposition of the precursor. Although the average Co_3O_4 and NiO crystallite sizes obtained by conventional thermal treatment in air were influenced by the pore size, particles typically consisted of agglomerates (2–60 nm) of crystallites that bear only a rather poor correlation to the pore diameter. NO calcination, on the other hand, yielded high metal oxide dispersions and narrow particle size distributions that were well in agreement with the average crystallite size. Nickel and cobalt oxide on

ordered mesoporous silica were investigated as a case study, but it is anticipated that similar results will be obtained for more conventional supports such as silica gel.

From chapter 2-5 it can be concluded that for cobalt and nickel nitrate the dispersion critically depends on the composition of the gas flow during decomposition. As is shown in **Chapter 6**, the situation is different for silica supported copper catalysts prepared by copper nitrate impregnation and calcination. The presence of a flow of gas during calcination was found to be essential to obtain a high dispersion and thus an active catalyst. Only moderate flows were needed to significantly improve the dispersion (average Cu particle size <10) over that observed after calcination in stagnant air (55 nm average Cu particle size), which was ascribed to the more efficient removal of water. *In situ* XRD and DRIFTS indicated that the composition of the gas flow had a large impact on the copper nitrate genesis and final metal oxide dispersion over the support. In the presence of an NO/N_2 flow, copper nitrate hydrate was rapidly and fully converted to highly dispersed copper hydroxynitrate followed by decomposition to highly dispersed CuO (6-8 nm) with a narrow particle size distribution, in agreement with results obtained for cobalt and nickel in Chapter 2-5. The average particle size was retained upon reduction, resulting in a good correlation between the CuO crystallite size, the CuO particle size and Cu particle size. In an O_2 and/or N_2 flow, decomposition occurred partly via an intermediate that was identified as copper nitrate anhydrate, a reactive species able to sublime. Sublimation of this compound during the thermal treatment in the presence of a flow resulted in redispersion, a similar process as chemical vapour deposition, yielding highly dispersed copper species. The other part decomposed via copper hydroxynitrate which agglomerated into large crystals and, thus, a bi-modal distribution was obtained. Due to the wide particle size distribution and the poor crystallinity there was no correlation between the CuO crystallite size obtained from XRD and the Cu particle size from N_2O chemisorption. Surprisingly, the copper specific surface area obtained after calcination in an O_2 and/or N_2 flow followed by reduction was similar to that obtained in NO. It is proposed that gas phase redispersion, which is not observed for cobalt and nickel nitrate, is the origin of the high copper oxide dispersions in an N_2 and air flow in comparison to cobalt to nickel oxide.

Summarizing the results described in this thesis we have shown that in-depth fundamental studies provide valuable insight into the physico-chemical processes that occur during catalyst preparation. Using this methodology we succeeded in identifying the mobile and immobile metal nitrate phases during decomposition and were able to steer the decomposition pathway towards the phases that yielded

high metal oxide dispersions. For silica supported nickel and cobalt nitrate hydrate, mobility and agglomeration is reduced by inducing complete hydrolysis to the anhydrous hydroxynitrate. Nearly complete hydrolysis can be attained by a low temperature (≤150 °C) thermal treatment in a flow of diluted nitric oxide. Full decomposition (25-350 °C) in a flow of diluted nitric oxide further decreases mobility at high temperatures, leading to a further increase in the dispersion. Although good results are obtained for silica supported copper nitrate via this method, similar to better results are obtained by dehydration to anhydrous copper nitrate, which will be able to redisperse via the gas phase. Dehydration occurs via the decomposition in a moderate to fast flow of gas, not containing NO. Thus, although copper, nickel and cobalt nitrates may look similar at first glance, their decomposition and agglomeration behavior is very different.

Chapter 8

Nederlandse Samenvatting

Katalysatoren op basis van metaaloxiden fijverdeeld over een dragermateriaal zijn onontbeerlijk voor de productie van brandstoffen, chemicaliën, medicijnen en het vrijkomen van mileuvervuiling. Impregnatie van silica- en/of aluminadragers met een waterige oplossing van metaalzouten, gevolgd door een droogstap en een thermische ontledingsstap, is een van de meest gebruikte methoden om deze materialen te maken. De reden hiervoor is de praktische eenvoud van de methode, de lage kosten en de geringe afvalstroom. Metaalnitraten worden hierbij vaak gebruikt, omdat deze goedkoop en zeer goed oplosbaar in water zijn. De resulterende dispersie van het metaaloxide is echter vaak laag doordat de metaalnitraten agglomereren en redistribueren tijdens de droog- en ontledingsstap. Eerdere studies hebben laten zien dat een gasstroom van 1% v/v stikstofmonoxide (NO) in helium tijdens de ontleding van nikkel- of kobaltnitraat op silica agglomeratie van de nitraten voorkomt, wat resulteert in de vorming van hoog dispers nikkel- of kobaltoxide. Het doel van het onderzoek beschreven in deze dissertatie is om te begrijpen hoe NO de agglomeratie van metaalnitraat voorkomt en wat de relatie is tussen het ontledingspad van het metaalnitraat en de verkregen dispersie van het metaaloxide. Hiertoe is de ontleding van verschillende metaalnitraten bestudeerd met geavanceerde *in* en *ex situ* karakteriseringsmethoden zoals röntgendiffractie (XRD), diffuse reflectie infrarood spectroscopie (DRIFTS), thermisch gravimetrische analyse (TGA) en transmissie electronen microscopie (TEM).

In **Hoofdstuk 2** zijn TGA in combinatie met massa spectrometrische analyse van de geproduceerde gassen (MS), XRD en TEM gebruikt om de invloed van een NO/Ar gasstroom op het ontledingspad en de dispersie van de overgangsmetaalnitraten van Sc, Fe, Mn, Co, Ni, Cu en Zn te verkennen. De resultaten lieten zien dat de ontledingstemperatuur van alle metaalnitraten significant lager was wanneer er NO aanwezig was tijdens de ontleding. Voor zowel kobaltnitraat als nikkelnitraat is geverifieerd dat na ontleding in een NO/Ar gasstroom een hogere metaaloxidedispersie verkregen wordt dan in een Ar gasstroom. Daarbij resulteerde de aanwezigheid van NO ook in een hogere omzettingsgraad van metaalnitraten naar metaalnitraathydroxiden bij een lage temperatuur (≤150 °C). Deze lagere hydrolysetemperatuur werd toegeschreven aan een lagere Gibbs vrije energie voor de reactie in NO. Hiermee is aangetoond dat NO al bij lage temperatuur een significante invloed heeft op de ontleding van metaalnitraten.

De invloed van NO op de de fase-evolutie van nikkel- en kobaltnitraat tijdens de thermische ontleding is in meer detail onderzocht in **Hoofdstuk 3**. De resultaten van zowel *in situ* XRD als DRIFTS lieten zien dat een thermische ontleding van gedragen nikkel- and kobaltnitraat in een NO/N_2 gasstroom leidde tot een snelle en bijna complete hydrolyse naar anhydridisch nikkel- en kobaltnitraathydroxide

met stochiometrie $M_x(OH)_y(NO_3)_z$. Hydrolyse in een N_2 of O_2/N_2 gasstroom was daarentegen langzaam en incompleet. Op basis van de DRIFTS resultaten is gepostuleerd dat tenminste een deel van de fasen gevormd tijdens ontleding van metaalnitraat in een N_2 of O_2 gasstroom uit gehydrateerde nitraathydroxiden met stochiometrie $M_x(OH)_y(NO_3)_z \bullet aH_2O$ bestond. Door middel van een wasstap werden alle oplosbare nikkelnitraatfasen ($Ni_x(NO_3)_y \bullet aH_2O$ en $M_x(OH)_y(NO_3)_z \bullet aH_2O$) gevormd gedurende een thermische behandeling bij 150 °C in NO/N_2 verwijderd. Op basis hiervan werd geconcludeerd dat 85% van het nikkelnitraathydraat was omgezet naar onoplosbaar $M_x(OH)_y(NO_3)_z$ gedurende deze behandeling. Dezelfde thermische behandeling in een N_2 gasstroom, daarentegen, resulteerde in een omzettingsgraad van slechts 25% naar $M_x(OH)_y(NO_3)_z$. Thermische ontleding van de bij 150 °C gedroogde samples in stagnante lucht bij 450 °C, zonder verwijdering van de oplosbare fasen, resulteerde in respectievelijk 9 nm en 32 nm NiO kristaldomeinen voor de in NO/N_2 en N_2 gedroogde samples. Deze resultaten laten duidelijk zien dat de onoplosbare $M_x(OH)_y(NO_3)_z$-fase een geringere mobiliteit heeft vergeleken met de andere fasen. In conclusie, een sleutel tot het verkrijgen van hoge NiO en Co_3O_4 dispersies vanuit nitraatzouten is immobilisatie door middel van hydrolyse naar kobalt- en nikkelnitraathydroxiden bij lage temperatuur.

Hoewel de grootste toename in dispersie bewerkstelligd wordt door een ontleding bij lage temperatuur (≤150 °C) in een NO/N_2 gasstroom kan deze verder verbeterd worden door de gehele ontleding in een NO/N_2 gasstroom uit te voeren. De invloed van een NO/He gasstroom op de ontleding van silica gedragen nikkelnitraat(hydroxide) bij hoge temperatuur (>120 °C) werd bestudeerd in **Hoofdstuk 4**. Hier is een vergelijk gemaakt tussen de gasevolutie gedurende de thermische ontleding in ^{14}NO, ^{15}NO, $^{16}O_2$, $^{18}O_2$, en Ar, waaruit kon worden afgeleid dat NO zuurstofradicalen afkomstig van het metaalnitraat verwijderd tijdens de ontleding naar NiO (225-300 °C). Op basis hiervan is gepostuleerd dat de reactie van NO met zuurstofradicalen resulteert in een nitraatverarming van de nikkelnitraat(hydroxide)-fase, wat de vorming van kiemen voor NiO bevordert en daarmee de dispersie van NiO. DRIFTS resultaten ondersteunen deze toeschrijving omdat de aanwezigheid van NO niet alleen resulteerde in een afname van de intensiteit van de ν_{OH} en $\nu_4(-ONO_2)$ nikkelnitraathydroxide- vibratiebanden tijdens de ontleding, maar ook in een respectievelijke blauw- en roodverschuiving van deze frequenties. Vergelijkbare observaties tijdens de ontleding bij hoge temperatuur (≥150 °C) in een N_2O of H_2 gasstroom laten zien dat dit effect optreedt voor een breder spectrum aan gassen die zuurstofradicalen kunnen verwijderen.

Voor veel katalytische processen is er een optimale deeltjesgrootte voor de activiteit en daarom is controle over de gemiddelde deeltjesgrootte en

deeltjesgrootteverdeling essentieel. In **Hoofdstuk 5** zijn geordende mesoporeuze dragermaterialen met verschillende poriediameters gebruikt om de gemiddelde NiO en Co_3O_4 kristallietgrootte te variëren. De aanwezigheid van NO gedurende de ontleding van nikkel- en kobaltnitraat was essentieel om hoog dispers NiO en Co_3O_4 met een smalle deeltjesgrootteverdeling te verkrijgen. Hoewel de gemiddelde Co_3O_4 and NiO kristallietgrootte verkregen door conventionele thermische ontleding in lucht correleerde met de poriediameter, bestonden de deeltjes typisch uit agglomeraten (2–60 nm) van kristallieten die geen correlatie met de poriediameter vertoonden. Thermische onleding in NO daarentegen resulteerde in hoog dispers NiO en Co_3O_4 met een nauwe deeltjesgrootteverdeling, overeenkomend met de gemiddelde kristallietgrootte. Nikkel- en kobaltoxide op mesoporeus silica is onderzocht als een case-study maar het is de verwachting dat vergelijkbare resultaten verkregen zullen worden met meer conventionele dragers zoals silicagel.

Op basis van hoofdstuk 2-5 kunnen we concluderen dat voor kobalt- en nikkelnitraat de dispersie sterk wordt beïnvloed de samenstelling van de gasstroom tijdens de ontleding. **Hoofdstuk 6** laat echter zien dat voor silica-gedragen koperkatalysatoren bereid met kopernitraat de effecten anders zijn. In plaats van de gasstroomsamenstelling is de aanwezigheid van een gasstroom op zichzelf essentieel om een hoge dispersie en dus een actieve katalysator te verkrijgen. Een geringe gasstroom zorgt hierbij al voor een significant hogere dispersie in vergelijking met stagnante lucht. Het grote verschil in dispersie werd toegeschreven aan de verbeterde afvoer van water tijdens de ontleding. De discrepantie tussen de resultaten verkregen voor nikkel- en kobaltnitraat in vergelijking tot kopernitraat wordt uitgelegd aan de hand van het ontledingspad van kopernitraathydraat. Ontleding van kopernitraat in een O_2 en/of N_2 gasstroom vond gedeeltelijk plaats via een intermediair geïndentificeerd als het reactieve anhydridisch kopernitraat. Sublimatie van dit intermediair tijdens de thermische ontleding in een gasstroom resulteerde in redispersie van deze fase, wat leidde tot een hogere koper dispersie. Aangezien een deel van het kopernitraathydraat ontleedde via slecht gedispergeerd kopernitraathydroxide werd er een bi-modale deeltjesgrootteverdeling verkregen. De brede deetjesgrootteverdeling en de lage kristalliniteit van het koperoxide zorgde voor een slechte correlatie tussen de CuO kristallietgrootte, bepaald met XRD, en de koperdeeltjesgrootte, berekend uit N_2O chemisorptie. In een NO/N_2 gasstroom werd kopernitraat snel gehydrolyseerd naar hoog dispers kopernitraathydroxide gevolgd door ontleding naar CuO, zonder de formatie van het anhydrisch kopernitraat intermediair. In dit geval vond er geen gasfase redispersie plaats en vormde zich een smallere deetjesgrootteverdeling waardoor een veel betere correlatie tussen de CuO kristallietgrootte en Cu deeltjesgrootte gevonden werd. Gepostuleerd wordt dat de

lagere dispersies verkregen voor NiO en Co_3O_4 na metaalnitraatontleding in N_2 of lucht toegeschreven kan worden aan de afwezigheid van redispersie.

Samengevat laten de resultaten in deze dissertatie zien dat fundamentele studies nieuwe inzichten kunnen geven in de fysisch-chemische processen die plaatsvinden tijdens de bereiding van katalysatoren. Gebruikmakend van de beschreven methodologie zijn we er in geslaagd om de mobiele en immobiele metaalnitraatfasen te indentificeren en de ontleding zo te sturen dat alleen de fasen die hoogdisperse metaaloxiden geven, gevormd worden. Voor silica-gedragen nikkel- en kobaltnitraathydraat werd de mobiliteit gereduceerd door hydrolyse naar anhydridisch nitraathydroxide. Nagenoeg volledige hydrolyse kon worden bewerkstelligd door middel van een lage temperatuur (≤150 °C) thermische behandeling in een gasstroom met daarin NO. Volledige ontleding (25-350 °C) in een verdunde NO gasstroom beperkte de mobiliteit verder. Hoewel deze methode ook voor kopernitraat goede resultaten gaf, werden dezelfde en soms hogere dispersies verkregen door dehydratatie tot anhydridisch kopernitraat, wat kan redispergeren via de gasfase. Dehydratie vond plaats door een thermische behandeling in een geringe gasstroom in afwezigheid van NO. Hoewel metaalnitraten in bepaalde opzichten vergelijkbaar gedrag vertonen, zijn dus toch voor elk metaal specifieke eigenschappen van belang die ontleding en agglomeratie mede bepalen.

List of Publications and Presentations

Patent application

Wolters, M., P. Munnik, J.H. Bitter, P.E. de Jongh and K.P. de Jong: 'Method for producing a supported metal nitrate' GB0905222.6 2009.

Publications

M. Wolters, H. Daly, A. Goguet, F.C. Meunier, C. Hardace, J.H. Bitter, P.E. de Jongh and K.P. de Jong: *'DRIFTS/MS/Isotopic Labeling Study on the NO Moderated Decomposition of a Silica Supported Nickel Nitrate Catalyst Precursor' J. Phys. Chem. C* **2010**, *114*, 7839.

M. Wolters, L.J.W. van Grotel, T.M Eggenhuisen, J.R.A. Sietsma, K.P. de Jong and P.E. de Jongh: 'Combining confinement and NO calcination to arrive at highly dispersed supported nickel and cobalt oxide catalysts with a tunable particle size' *Catal. Today* **2010**, *doi:10.1016/j.cattod.2010.02.052*.

M. Wolters, I.C.A. Contreras Andrade, P. Munnik, J.H. Bitter, P.E. de Jongh, K.P. de Jong: 'Impact of NO on the decomposition of supported metal nitrate catalyst precursors and the final metal oxide dispersion'
Stud. Surf. Sci. Catal. **2010**, *175,* 69.

C.J. Gommes, H. Friedrich, M. Wolters, P.E. de Jongh and K.P. de Jong: 'Quantitative Characterization of Pore Corrugation in Ordered Mesoporous Materials Using Image Analysis of Electron Tomograms'
Chem. Mater. **2009**, *21*, 1311.

Wolters, M., P. Munnik, J.H. Bitter, P.E. de Jongh and K.P. de Jong: 'How NO immobilizes nickel and cobalt nitrates to arrive at highly dispersed silica supported nickel and cobalt oxide' (submitted).

Wolters, M., P. Munnik, J.H. Bitter, P.E. de Jongh and K.P. de Jong: 'Copper nitrate mobility during thermal treatment and the effect on the dispersion and catalytic activity of silica supported copper catalysts' (in preparation)

Oral Presentations

M. Wolters, P. Munnik, I. C. A. Contreras Andrade, J. H. Bitter, P. E. de Jongh, K. P. de Jong: 'Impact of NO on the decomposition of supported metal nitrate catalyst precursors and the final metal oxide dispersion'
TOCAT6/APCAT5, Sapporo, Japan, July 18-23, 2010

M. Wolters, P. Munnik, I. C. A. Contreras Andrade, J. H. Bitter, P. E. de Jongh, K. P. de Jong: 'Impact of NO on the decomposition of supported metal nitrate catalyst precursors and the final metal oxide dispersion'
10th International Symposium on the Scientific Bases for the Preparation of Heterogeneous Catalysts, Louvain-la-Neuve, Belgium, July 11-15, 2010

M. Wolters, P. Munnik, J. H. Bitter, P. E. de Jongh, K. P. de Jong: 'Thermal activation of supported catalysts prepared by impregnation and drying - How NO yields highly dispersed metal catalysts'
Johnson Matthey Academic Conference, Loughborough, UK, April 14-15, 2010

M. Wolters, P. Munnik, J. H. Bitter, P. E. de Jongh, K. P. de Jong: 'How NO affects the decomposition of metal nitrates to arrive at highly dispersed metal catalysts'
10th Netherlands Chemistry and Catalysis Conference, Noordwijkerhout, Netherlands, March 1-3, 2010

M. Wolters, P. Munnik, J. H. Bitter, P. E. de Jongh, K. P. de Jong: 'How NO affects the decomposition of metal nitrates to arrive at highly dispersed metal catalysts'
Johnson Matthey Academic Conference, Loughborough, UK, April 6-7, 2009

M. Wolters, L. J. W. van Grotel, J. R. A. Sietsma, P. E. de Jongh and K. P. de Jong: 'Preparation of supported NiO and Co_3O_4 with tunable particle size via confinement'
10th Netherlands Chemistry and Catalysis Conference, Noordwijkerhout, Netherlands, March 2-4, 2009

M. Wolters, J. R. A. Sietsma, J. H. Bitter, P. E. de Jongh, K. P. de Jong: 'Nitric oxide moderated metal nitrate decomposition'
10th Netherlands Chemistry and Catalysis Conference, Noordwijkerhout, Netherlands, March -53, 2008

Poster Presentations

M. Wolters, L. J. W. van Grotel, T. M. Eggenhuisen, P. E. de Jongh and K.P. de Jong: 'Preparation of supported NiO and Co_3O_4 with tuneable particle size: impact of confinement and gas atmosphere'
10th International Symposium on the Scientific Bases for the Preparation of Heterogeneous Catalysts, Louvain-la-Neuve, Belgium, July 2010

M. Wolters, L. J. W. van Grotel, T. M. Eggenhuisen, P. E. de Jongh and K.P. de Jong: 'Preparation of supported NiO and Co_3O_4 with tuneable particle size: impact of confinement and gas atmosphere'
International Zeolite Conference - International Mesoporous Materials Conference, Sorrento, Italy, July 2010

M. Wolters, L. J. W. van Grotel, T. M. Eggenhuisen, P. E. de Jongh and K.P. de Jong: 'Preparation of supported NiO and Co_3O_4 with tuneable particle size: impact of confinement and gas atmosphere'
9th EuropaCat, Salamanca, Spain, August 2009

M. Wolters, L. J. W. van Grotel, T. M. Eggenhuisen, P. E. de Jongh and K.P. de Jong: 'Preparation of supported NiO and Co_3O_4 with tuneable particle size: impact of confinement and gas atmosphere'
21th North American Meeting, San Fransisco, USA, June 2009

M. Wolters, H. Daly, F. Meunier, P.E. de Jongh, J.H. Bitter, A. Goguet and K.P. de Jong: 'Nitric oxide moderated nickel nitrate decomposition: unravelling the mechanism'
Johnson Matthey Academic Conference, Nottingham, UK, June 2008

M. Wolters, H. Daly, F. Meunier, P.E. de Jongh, J.H. Bitter, A. Goguet and K.P. de Jong: 'Preparation of supported metal (oxide) catalysts: understanding the agglomeration behaviour of metal nitrate precursors'
Johnson Matthey Academic Conference, Nottingham, UK, June 2007

Dankwoord/Acknowledgements

After 120 pages I'm now left with only a few more pages to write. The past four years would not have been as successful and enjoyable without the support and contributions of many colleagues, family members and friends. It would take many more pages to include everyone, so on forehand I appologize to those I do not name personally.

Krijn, ik wil jou bedanken voor de mogelijkheid die je mij hebt gegeven om een promotieonderzoek in jouw groep te doen. Ik heb in de afgelopen vier jaar heel veel van je kritische blik en inzichten geleerd en genoten van jouw passie voor de wetenschap. Petra, heel erg bedankt voor je snelle en kritische correctie van mijn artikelen en je enthousiasme voor mijn werk. Tevens bedankt voor het promoten van mijn werk op verscheidene conferenties, mijn "confinement" poster is zo de halve wereld over geweest. Harry, hoewel je niet als co-promotor voorin mijn proefschrift staat, voelt het door jouw grote bijdrage aan mijn artikelen wel zo. Ik heb erg genoten van onze wetenschappelijke en wat minder wetenschappelijke discussies en bijeenkomsten.

Tijdens mijn promotie heb ik hulp gekregen van een heel aantal studenten. Ingmar en Tjalling, bedankt voor de nieuwe inzichten die ik mede dankzij jullie literatuur scripties heb verkregen. Lotte, jouw werk staat voor het grootste gedeelte beschreven in hoofdstuk 5, bedankt hiervoor. Irene and Mustafa, thank you for your explorative work. Van de vele DRIFTS metingen die in deze thesis te vinden zijn is het grootste gedeelte door jou uitgevoerd Peter. Heel erg bedankt en ik wens je nog veel succes met je promotieonderzoek en verdere carrière.

I would like to thank all the people from Johnson Matthey Catalysts that made my various visits to Chilton a pleasure, both during and after work hours. A few people I would like to name specifically. Steve Pollington and John Casci, the numerous fruitful meetings and discussions at various JM sites have been an absolute pleasure. Thank you for all your time and contributions to my work. John Ridland, thank you for the fast writing of the patent application and (sometimes last minute) reviewing of numerous publications, abstracts and presentations. Anders Gabrielsson and Gareth Headdock, thank you for hosting me at Chilton and for the scientific discussions on the work described in chapter 6. Leon van de Water, you

made travelling to and from the Chilton site more efficient, but above all much more enjoyable.

Helen Daly, Alexandre Goguet, Frederic Meunier and Chris Hardacre, thank you for hosting me at the Queens University Belfast and the fruitful collaboration that led to the work described in Chapter 4. Ignacio Contreras Andrade, thank you for your explorative work.

Of course a word for all my colleagues from the Inorganic Chemistry and Catalysis group, who have made working in the group a pleasure. I also enjoyed all the coffee/lunch breaks, drinks, labuitjes, conferences and other outings in the past four years. A special thanks for my (former) office mates Arjan, Ingmar, Matti, Sankara and Jinbao who made working in office N209 enjoyable. Tamara, Heiner and Jelle, thank you for the nice collaborations. Niels, ik vond het leuk om een keer carnaval op z'n Brabants mee te maken. Succes met je verdere carrière. Adri en Anne-Mette, door jullie was het ook in de vroege uurtjes gezellig op de vakgroep. Dank ook aan Inge en Fouad voor alle gezelligheid. Fouad, tevens bedankt voor je hulp met de DRIFTS metingen. Natuurlijk wil ik ook de verdere vaste staf; Ad M., Ad E., Tom, Vincent, Fred, Cor, Hans, Monique en Dymph, bedanken hun bijdragen de afgelopen vier jaar.

De laatste paragraaf is voor mijn familie en vrienden, zonder wie ik dit proefschrift niet tot stand had kunnen brengen. Joyce, je bent een vrolijke noot geweest wanneer ik dat het meest nodig had, bedankt daarvoor. Anne, ik vind het echt super dat je mijn paranimf wilt zijn. Mijn dierbare vrienden en huisgenoten Dominik en Renata, dat jullie achter mij staan is mij enorm veel waard. Johan, wie had ooit kunnen denken dat een carpoolafspraak en wat klassieke muziek tot zoiets moois zou leiden. Bedankt voor alles. Papa, mama, broer en oma, jullie onvoorwaardelijke liefde, steun en vertrouwen in mij zijn de afgelopen jaren een bron van inspiratie en kracht geweest. Ik hou van jullie.

Mariska

About the Author

Mariska Wolters was born on the 30th of August 1983 in Lelystad. She attended the SGL (secondary school) in Lelystad from 1995-2001. In September 2001 she started with a bachelor study Chemistry at the VU in Amsterdam and received her bachelor's degree in September 2004. Afterwards she started with the master Chemistry and Physics at Utrecht University from which she obtained her master's degree with specialization in Inorganic Chemistry and Catalysis (Dr. F. Winter and Prof.dr.ir. K.P. de Jong) in September 2006. From October 2006 till October 2010 she worked as a PhD-student in the Inorganic Chemistry and Catalysis group at Utrecht University under the supervision of Prof.dr.ir. K.P. de Jong and Dr. P.E. de Jongh. The results obtained during this period are described in this thesis and were presented at several (inter)national conferences. During the Johnson Matthey Academic Conference in Loughborough in 2010 she received the award for best oral presentation. Starting 1st of November 2010, she will work as a research scientist at Shell Global Solutions in Amsterdam.